ANODIC CATALYST DESIGN FOR HIGHLY EFFICIENT FRESHWATER AND SEAWATER ELECTROLYSIS

LI LU

PhD

The Hong Kong Polytechnic University

2025

The Hong Kong Polytechnic University

Department of Applied Physics

Anodic catalyst design for highly efficient freshwater and seawater electrolysis

LI Lu

A thesis submitted in partial fulfilment of the requirements for the degree of Doctor of Philosophy

August 2024

CERTIFICATE OF ORIGINALITY

I hereby declare that this thesis is my own work and that, to the best of my knowledge and belief, it reproduces no material previously published or written, nor material that has been accepted for the award of any other degree or diploma, except where due acknowledgement has been made in the text.

(Signed)

LI Lu (Name of student)

ABSTRACT

The excessive consumption of traditional fossil fuels, driven by rapid industrialization worldwide, has resulted in severe energy crises and environmental pollution. Mitigating carbon emissions and addressing environmental degradation have emerged as critical challenges for contemporary society. In this context, the pursuit of affordable, clean, and environmentally sustainable alternative energy sources has gained considerable attention. Hydrogen energy is increasingly recognized as a viable alternative to fossil fuels and plays a pivotal role in achieving carbon neutrality. Among various hydrogen production methods, water electrolysis is particularly attractive owing to its high efficiency and zero carbon emissions. Recently, the utilization of seawater as a feedstock in place of highly purified freshwater in electrolysis has attracted considerable interest due to the widespread distribution and abundant reserves of seawater. However, the sluggish kinetics of the anodic oxygen evolution reaction (OER) significantly hinders the overall efficiency of water electrolysis. Furthermore, for seawater electrolysis, the high concentration of Cl^- would compete with anodic OER, leading to the chlorine oxidation reaction (ClOR) and generating corrosive Cl_2 and ClO^-, which poses additional challenges. To enhance the efficiency and selectivity of OER for water/seawater electrolysis, it is crucial to develop highly efficient electrocatalysts that can facilitate the anodic OER while suppressing the ClOR.

This thesis presents a comprehensive investigation into the development and optimization of efficient transition metal (TM)-based electrocatalysts for OER in practical freshwater and seawater electrolysis applications. The research aims to address the critical challenges of activity, stability, and selectivity in OER catalysis, particularly in the presence of high-concentration chloride ions in seawater. The key research findings are as follows:

1. CeO_2/NiFe-based layered double hydroxides (LDH) composite with high oxygen ion diffusion rates and a high concentration of oxygen vacancies are designed to optimize OER activity under alkaline and seawater electrolytes. The partial coverage of CeO_2 on LDH surfaces inhibits direct Cl^- adsorption on active sites, while high proton conductivity mitigates proton accumulation within LDH interlayers, thereby preventing structural collapse and ensuring superior stability. Notably, the enhanced mixed ionic conductivities at elevated temperature contribute to significant improvements in OER performance. The chapter underscores the effectiveness of employing mixed ionic conductors for enhancing OER performance and highlights the importance of characterizing electrocatalysts and cells under service conditions for practical applications.
2. A novel nickel substituted double perovskite material, $NdBa_{0.75}Ca_{0.25}Co_{1.5}Fe_{0.4}Ni_{0.1}O_{5+\delta}$ (NBCCFN), has been synthesized via the electrospinning method. It has been found that the incorporation of Ni increases the concentration of oxygen vacancies in perovskite and facilitates the formation of oxyhydroxide species on the perovskite surface during OER. Density functional theory (DFT) calculations reveal that the OER process for NBCCFN proceeds via a lattice oxygen mechanism, while Ni incorporation effectively reduces the reaction energy barrier of the potential determining step. This chapter indicates that NBCCFN perovskite has remarkable activity, selectivity, and durability for water and seawater electrolysis, holding significant potential for practical applications.
3. Cobalt metaphosphate ($K_2Co(PO_3)_4$) is explored as an OER catalyst in freshwater and seawater electrolysis. As indicated by various characterizations, the metaphosphate experienced a complete and irreversible structural reconstruction process during OER, in-situ forming CoOOH that acts as the real active sites. The reconstruction process is accompanied by the leaching of metaphosphate ions. Moreover, the advantageous

adsorption of OH^- rather than Cl^- helps to achieve high selectivity of the prepared catalyst, which also prevents the negative effect of chlorine adsorption. This chapter underscores the potential of cobalt metaphosphate as a highly efficient, selective, and robust OER pre-catalyst capable of maintaining performance in challenging environments.

The collective findings from these chapters advance the field of OER catalysis, particularly for seawater electrolysis applications. The developed and optimized electrocatalysts that can effectively prevent Cl^- adsorption and oxidation while maintaining high OER activity and stability are crucial for the practical implementation of seawater electrolysis technologies. The strategies employed in material design pave the way for the development of high-performance OER catalysts. Furthermore, the integration of in-situ and ex-situ characterization techniques provides valuable insights into understanding OER mechanisms, which can guide the design and optimization of new materials for practical applications in freshwater and seawater electrolysis.

AUTHOR'S PUBLICATIONS

[1]. Lu Li, Gao Chen*, Zongping Shao, and Haitao Huang*, Progress on Smart Integrated System of Seawater Purification and Electrolysis. *Energy & Environmental Science*, **2023**, *16*, 4994.

[2]. Lu Li, Liqi Bai, Sixuan She, Gao Chen*, and Haitao Huang*, Mixed Ionic Conductor Brings Extra Gain in Oxygen-Evolving Activity of NiFe Hydroxide Electrocatalyst at Practical Working Temperature, *Applied Catalysis B: Environment and Energy*, **2025,** *371***,** 125271.

[3]. Lu Li, Liqi Bai, Hao Li, Gao Chen, and Haitao Huang*, Facilitated Generation of Oxyhydroxides Induced by Nickel Substitution for Highly Efficient and Selective Seawater Electrolysis, **Finished**.

[4]. Lu Li, Liqi Bai, Hao Li, Gao Chen, and Haitao Huang*, Complete and Fast Reconstruction of Cobalt Metaphosphate for Highly Efficient and Selective OER in Seawater Electrolysis, **Finished**.

ACKNOWLEDGEMENTS

I would like to take this opportunity to express my sincerest gratitude to several individuals who have played a significant role in the completion of my PhD thesis.

First and foremost, I would like to express my sincerest gratitude to my supervisor, Prof. Haitao Huang, for his unwavering support and guidance throughout this research journey. His profound expertise, constructive feedback, and continuous encouragement have been instrumental in shaping this thesis and enhancing my academic development.

Special gratitude is extended to Dr. Gao Chen, Dr. Liqi Bai, and Dr. Hao Li for their generous assistance and valuable recommendations throughout my research.

I am also grateful to my groupmates and colleagues, as well as all participants in this study, for their collaboration, insightful suggestions, and continuing support.

I am also indebted to my family for their unwavering support, understanding, and patience during this demanding period. Their love and encouragement have been a constant source of strength for me.

Lastly, I would like to acknowledge the financial support provided by the PolyU Presidential PhD Fellowship Scheme 2021/22, which made this research possible.

I am truly grateful to all those who have contributed to this thesis in any way. Thank you.

TABLE OF CONTENTS

LIST OF FIGURES

LIST OF TABLES

LIST OF ABBREVIATIONS

AEL	Anion-exchange layer
AEM	Adsorbate evolution mechanism
AEMWE	Anion exchange membrane water electrolyser
AWE	Alkaline water electrolysis
BET	Brunauer-Emmett-Teller
BPMWE	Bipolar membrane water electrolyser
BSCF	$Ba_{0.5}Sr_{0.5}Co_{0.8}Fe_{0.2}O_{3-\delta}$
CA	Chronoamperometry
CEL	Cation-exchange layer
CL	Catalyst layer
CP	Chronopotentiometry
CV	Cyclic voltammetry
ClOR	Chlorine oxidation reaction
C_{dl}	Double layer capacitance
DFT	Density functional theory
DMF	Dimethylformamide
DMSM	Dual-metal-site mechanism
D_O	Oxygen diffusion coefficients
D_P	Proton diffusion coefficients
ECSA	Electrochemical surface area
EDS	Energy dispersive spectroscopy
EDX	Energy-dispersive X-ray

EIS	Electrochemical impedance spectra
EXAFS	Extended X-ray absorption fine structure
FE	Faraday efficiency
FESEM	Field emission scanning electron microscope
FETEM	Field emission transmission electron microscope
FT-IR	Fourier-transform infrared spectroscopy
fcc	Face-centered cubic
GDL	Gas diffusion layer
GSAS	General Structure Analysis System
HER	Hydrogen evolution reaction
HF	Hydrogen fluoride
HR-TEM	High-resolution transmission electron microscopy
H^+	Proton
H_2	Hydrogen
ICP-MS	Inductively coupled plasma-mass spectrometry
ICP-OES	ICP-optical emission spectrometry
LDH	Layered double hydroxide
LOM	Lattice oxygen mechanism
LSV	Linear sweep voltammetry
MA	Mass activity
MEA	Membrane electrode assembly
MOR	Methanol electrooxidation reaction
MW	Megawatts
NRR	Nitrogen reduction reaction
OCP	Open circuit potential

OER	Oxygen evolution reaction
ORR	Oxygen reduction reaction
OVSM	Oxygen-vacancy-site mechanism
PAN	Polyacrylonitrile
PEM	Proton exchange membrane
PEMFC	Proton exchange membrane fuel cell
PEMWE	Proton exchange membrane water electrolysis
PFSA	Perfluoroalkylsulfonic acid
RDE	Rotating disk electrode
RHE	Reversible hydrogen electrode
RRDE	Rotating ring disk electrode
RT	Room temperature
R&D	Research and development
R_{ct}	Charge transfer resistance
SA	Specific activity
SEM	Scanning electron microscope
SMR	Steam methane reforming
SMSM	Single-metal-site mechanism
SOEC	Solid oxide electrolysis cell
TEM	Transmission electron microscopy
TM	Transition metal
TMA^+	Tetraalkylammonium cation
TMO	Transition metal oxide
TMP	Transition-metal phosphate
TOF	Turnover frequency

UV-vis	Ultraviolet-visible spectroscopy
XANES	X-ray absorption near-edge structure
XAS	X-ray absorption spectroscopy
XPS	X-ray photoelectron spectroscopy
XRD	X-ray diffraction
1D	One-dimensional
2D	Two-dimensional
3D	Three-dimensional
η	Overpotential

Chapter 1 Introduction

1.1 Background

1.1.1 Global Energy Trends

At present, fossil fuels continue to serve as the predominant energy source for most nations and regions in the world. As the global economy and society continue to expand, challenges such as energy security, environmental pollution, and climate change have increasingly come to the forefront. The transition to sustainable energy represents a pivotal challenge confronting global society in the 21st century. Carbon-free and low-pollution renewable energy has become an integral component of the future energy framework. Hydrogen, with its high energy density and zero carbon emissions when burned, has become a key element in the envisioned renewable energy landscape [1]. It offers a versatile solution for energy storage, transportation, and as a feedstock for various industrial processes. However, achieving a hydrogen economy depends on the development of efficient and sustainable production methods.

1.1.2 Production of Green Hydrogen

Currently, the vast majority of hydrogen is produced from fossil fuels, predominantly through coal gasification and steam methane reforming (SMR) of natural gas [2]. Coal gasification is a thermo-chemical process in which the gasifier's heat and pressure break down coal into its chemical constituents including H_2, CO, and CO_2, which is referred to as “brown hydrogen”. For SMR, the methane in natural gas is transformed into H_2 and CO_2 under high heat and pressure, of which the hydrogen is called “blue hydrogen”. Water electrolysis (or water splitting) is another important way to produce H_2. If the water electrolysis process is driven

by environmentally friendly renewable energies such as wind, solar, and tide, the hydrogen produced is called "green hydrogen". The production of green hydrogen by electrolysis of water has the potential to yield high-purity H_2, mitigate carbon emissions, and alleviate environmental pollution [3]. As compared in **Table 1.1**, water electrolysis represents an appealing renewable hydrogen production method capable of directly converting electrical energy into chemical energy stored in hydrogen, holding great promise for meeting the "Net Zero Emissions" targets by 2050.

Table 1.1 The comparison between different hydrogen color shades [4].

Hydrogen Color	Technology	Source	Products	Cost ($ kg/H_2)	CO_2 Emission
Brown hydrogen	Gasification	Coal	$H_2 + CO_2$	1.2-2.1	High
Blue hydrogen	SMR	Natural gas	$H_2 + CO_2$	1.5-2.9	Low
Green hydrogen	Electrolysis	Water	$H_2 + O_2$	3.6-5.8	Minimum

Water electrolysis refers to splitting water molecules into hydrogen and oxygen under the driven force of electricity. The efficiency of water electrolysis is dependent on the kinetics of its two half-reactions: the hydrogen evolution reaction (HER) at the cathode and the oxygen evolution reaction (OER) at the anode. While HER has been significantly optimized, OER remains a challenging and energy-intensive reaction [5, 6]. OER entails the oxidation of water molecules to produce molecular oxygen, protons, and electrons, constituting a four-electron transfer process involving formation and evolution of various intermediate species, inherently rendering it slower in kinetics than the two-electron transfer HER. The sluggish kinetics of the OER require higher overpotentials, consequently resulting in increased energy

consumption and reduced electrolysis efficiency. In light of this, researchers have exerted significant efforts to enhance the reaction kinetics and elevate the overall energy efficiency, achieving considerable progress.

1.1.3 Progress on Water Electrolysis

Since the first discovery of water electrolysis by Troostwijk and Deiman in 1789, it has been developed for over 200 years (**Figure 1.1**) [7]. Subsequently, in 1833, the establishment of Faraday's Law quantified the electrical energy consumption and gas production, providing formal validation for hydrogen production through water electrolysis [8]. In fact, the actual industrialization of hydrogen production through water electrolysis can be attributed to the invention of the Gram machine in 1869 and the establishment of industrial production for hydrogen in alkaline solutions by Lachinov in 1888 [9]. Since then, the water electrolysis technologies have experienced rapid development. The second stage was a fast development age of industrial water electrolysis technology, during which various membranes, electrocatalysts, and innovative devices were used for commercialization. For example, the asbestos separator, a bipolar configuration electrolyser with a press filter effect, and the Raney nickel were developed and implemented in water electrolysis, significantly advancing the progress of this technology [10, 11]. Nonetheless, the burgeoning petrochemical industry facilitated the production of hydrogen through steam methane reforming and coal gasification, resulting in significantly more cost-effective hydrogen production post-1970s, leading to a period of stagnation for hydrogen production via water electrolysis. Nowadays, the escalating energy crisis and growing environmental concerns have reignited interest in the generation of clean hydrogen through water electrolysis.

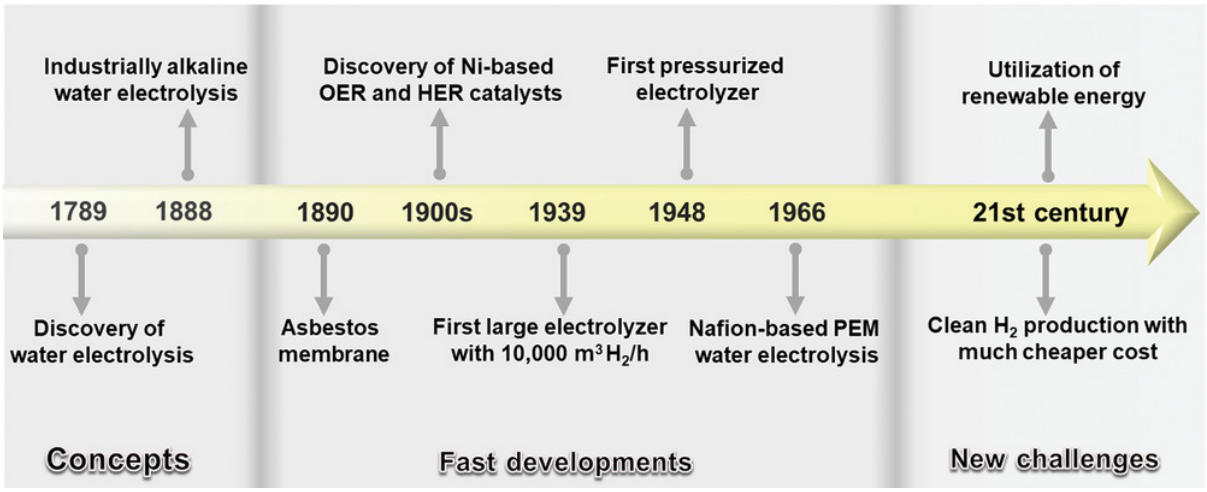

Figure 1.1 Timeline of water electrolysis [12].

At present, the overall efficiency, capital costs, and long-term stability of prevailing water electrolysis technologies are inadequate to meet the requirements for energy structure transition. With the continuous advancement of technology, various new technologies and new materials continue to emerge, bringing opportunities and challenges to water electrolysis technology, especially in combination with renewable energies. For instance, to mitigate energy consumption resulting from the sluggish half-reaction kinetics, significant endeavors have been undertaken to develop high-performance electrocatalysts. Typically, an ideal OER electrocatalyst should exhibit high activity, long-term stability, and corrosion resistance in an anodic oxidation environment [13]. Although noble metal oxides such as iridium oxide IrO_2 and ruthenium oxide RuO_2 are known for their excellent OER activity, their scarcity, high cost, and sustainability issues limit their practical applications. This has prompted a strong investigation of alternative materials, including transition metal (TM) oxides, hydroxides, sulfides, phosphides, and layered double hydroxides, as well as carbon-based materials [14]. The employment of these cost-effective electrocatalysts would significantly reduce the operational expenses of water electrolysis systems. Meanwhile, a variety of advanced water electrolysis technologies have emerged in recent years to improve system efficiency and

facilitate large-scale production of hydrogen, which will be introduced in the following section. However, various challenges still persist. For example, although different TM-based catalysts have been employed to reduce the costs of water electrolysis systems, improving the electrolytic efficiency of hydrogen production using existing electrodes is a huge challenge and requires further substantial progress. Besides, although employing fluctuating power sources holds promise as a cost-effective approach for hydrogen production, but the frequent initiation and cessation of water electrolysers can result in significant degradation of their components, requiring further advancements in durable and responsive electrolyser components [15]. Therefore, there is still a long way to go.

Currently, the well-established water electrolysis technologies require highly purified freshwater as feedstock [16]. The necessity for ultra-pure water increases the expense of hydrogen production by water electrolysis and constrains the establishment of water electrolysis facilities in particular regions (such as arid lands and remote areas) where freshwater is deemed a precious resource, posing a sustainability challenge given the increasing global water scarcity. Seawater, which covers over 70% of the Earth's surface, presents an abundant and infinite resource for hydrogen production through electrolysis [17]. As an alternative to freshwater electrolysis, electro-splitting seawater into hydrogen energy could not only alleviate the pressure on freshwater resources and save system costs, but also open new avenues for large-scale hydrogen production in coastal and offshore settings, closely integrated with marine renewable energy sources such as offshore wind and tidal power, thus attracting a wide range of interest from researchers all over the world. However, the composition of seawater is rather complex, posing significant challenges toward the selectivity and long-term stability of direct seawater electrolysis. One of the most significant concerns is the chlorine ions with the highest concentration in seawater (~0.5658 M). The

chemistry of chlorine in seawater is intricate and greatly dependent on pH levels. The chlorine electrooxidation reaction (ClOR), a two-electron transfer process, will compete with anodic OER due to its more favorable kinetics, while in turn its products (such as Cl_2 and ClO^-) are corrosive to the electrolyser components, thus reducing electrocatalytic activity and long-term robustness of the system [18]. However, ClOR is thermodynamically unfavorable compared to OER under alkaline conditions (pH > 7.5), leaving an equilibrium potential difference window of 0.480 V for selective OER over ClOR [19]. Therefore, developing anode materials and catalysts that selectively favor the OER over the ClOR in an alkaline environment is a significant research endeavor. These materials should exhibit high electrocatalytic activity for the OER, while also possessing intrinsic resistance to chloride oxidation, corrosion, and biofouling. Additionally, understanding the reaction mechanisms and the interplay between the OER and ClOR at the anode surface is crucial for the rational design of such materials.

1.2 Fundamentals of Water Electrolysis

1.2.1 Working Principles

A standard electrolytic cell mainly comprises an external power supply, an electrolyte solution, and two electrodes (anode and cathode). In low-temperature water electrolysis, anodes and cathodes are immersed in the aqueous electrolyte and connected to an external circuit. The OER and HER occur at the anode and cathode, respectively, which are both pH dependent. When an appropriate voltage is provided, the half reactions can be described below:

In acid condition:

Anode: $H_2O \rightarrow 1/2O_2 + 2H^+ + 2e^-$ (1.1)

Cathode: $2H^+ + 2e^- \rightarrow H_2$ (1.2)

In neutral condition:

Anode: $2H_2O \rightarrow O_2 + 4H^+ + 4e^-$ (1.3)

Cathode: $4H_2O + 4e^- \rightarrow 2H_2 + 4OH^-$ (1.4)

In alkaline condition:

Anode: $4OH^- \rightarrow O_2 + 2H_2O + 4e^-$ (1.5)

Cathode: $4H_2O + 4e^- \rightarrow 2H_2 + 4OH^-$ (1.6)

For different electrolytes, the overall reaction is:

$2H_2O + \text{Electricity} \rightarrow 2H_2 + O_2$ (1.7)

The total reversible cell voltage (E_{rev}) of water electrolysis is calculated using the cell potentials of the two half-reactions, which can be described below:

$E_{rev} = E_{anode} - E_{cathode}$ (1.8)

Under standard conditions, E_{rev} equals 1.23 V. The equilibrium voltage values E^0 at the anode and cathode are influenced by the electrolyte's pH, while the E_{rev} value of 1.23 V remains constant. To enable water electrolysis, the applied voltage needs to be large enough to overcome the Ohmic drop caused by ion conduction in aqueous electrolytes, the overpotential for OER and HER, and cell resistance. Therefore, the actual cell voltage (E_{cell}) can be described as:

$$E_{cell} = E_{rev} + \eta_{anode} + \eta_{cathode} + I \times R_{cell} \quad (1.9)$$

where the anode overpotential, cathode overpotential, current, and overall cell resistance are represented by the variables η_{anode}, $\eta_{cathode}$, I, and R_{cell}, respectively.

Thermodynamically, water electrolysis is an endothermic reaction, which is described below:

$$\Delta H^0 = \Delta G^0 + T\Delta S^0 \quad (1.10)$$

The ΔH^0 is the change of enthalpy change, ΔG^0 is the change of Gibbs free energy, and ΔS^0 is the difference of thermal energy, which are 285.8, 237.1, and 48.7 kJ mol^{-1}, respectively, under standard conditions (298.15 K, 1 atm). Since the ΔH^0 typically consists of both thermal and electrical energy, the water electrolysis based on the thermodynamic views can be defined as:

$$H_2O + 237.1 \text{ kJ mol}^{-1} \text{ (electricity)} + 48.7 \text{ kJ mol}^{-1} \text{ (heat)} \rightarrow H_2 + 1/2O_2 \quad (1.11)$$

Hence, heat and electrical energy are necessary for the water electrolysis to occur under standard conditions. For a given temperature, the reaction will not start until sufficient work and heat are supplied. The environment can serve as a source of heat. Therefore, the reaction's necessary enthalpy is equal to 285.8 kJ mol^{-1}. The water electrolysis process can become spontaneous when the free energy becomes negative at high temperatures (approximately 3000 K), however, this impractical energy demand can lead to severe deterioration of the electrolyser's component parts due to the exceedingly high temperature. Therefore, a much more practical solution to overcome the free energy would be engineering the electrochemical cell consisting of two electrodes inside the electrolyte.

1.2.2 Electrolyser Classifications

According to the types of electrolytes, operating conditions, and ionic agents, water electrolysis technologies can be mainly divided into four types, which are alkaline water electrolysis (AWE), solid oxide electrolysis cell (SOEC), proton exchange membrane water electrolysis (PEMWE), and anion exchange membrane water electrolysis (AEMWE), as shown in **Figure 1.2**.

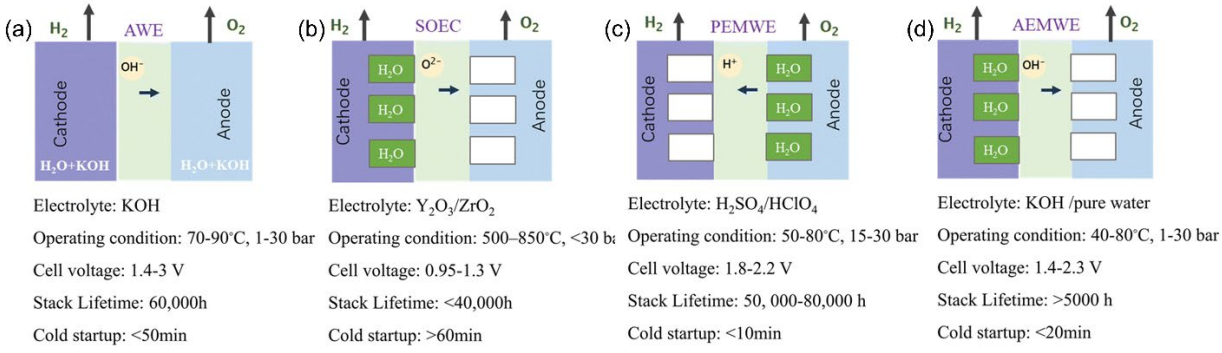

Figure 1.2 Schematic compositions of different water electrolysis cells, including (a) AWE, (b) SOEC, (c) PEMWE, and (d) AEMWE [20].

Alkaline Water Electrolysis

AWE has been under development for more than two centuries. Up to now, hydrogen production by AWE has become a mature technology that has commercially produced megawatts (MW) of high-rank hydrogen. The common configuration of AWE consists of two electrodes immersed in an alkaline KOH or NaOH electrolytic solutions with a concentration of 30% to 40% (**Figure 1.2a**). In a traditional industrial setup, electrodes loaded with electrocatalysts such as Raney nickel, nickel (or iron)-plated steel, or nickel/stainless-steel mesh are submerged in a highly concentrated KOH solution. A porous diaphragm is used to separate the two electrodes and the product gases of the electrodes, which enables the

permeation of hydroxide ions and water molecules. The diaphragm is a critical component for the overall performance of the cell, as it enables ionic contact between the electrodes and prevents the mixing of the produced gases. The operating temperature of AWE typically range from 70 to 90 °C with an efficiency range between 70 and 80%. The capability to utilize non-precious metal catalysts coupled with the low capital price (€170-1000 kW^{-1}), constitutes the most significant advantage of AWE, contributing to cost reduction for large-scale hydrogen production. Besides, its stable operation and extended service life are conducive to reducing the maintenance cost of devices. At present, a major challenge for AWE is the low energy efficiency due to the significant ohmic resistance across the liquid electrolyte and diaphragm, resulting in substantial power consumption [21]. Furthermore, the porous diaphragm can result in incomplete prevention of cross-diffusion of product gases, thereby reducing the purity of the produced hydrogen [22]. In addition, the challenges of integration with renewables due to the slow response to load changes and the significant leakage issues are also considered noteworthy. In recent years, AWE has garnered renewed attention due to its unique properties for seawater electrolysis. When supplied with seawater, the highly concentrated OH^- environment of AWE is more conducive to facilitating OER than ClOR and it helps prevent the pre-precipitation of Ca^{2+}/Mg^{2+} to avoid electrode blockage. Nevertheless, the presence of complex ions and impurities inevitably leads to diagram blockage and gaseous crossover, giving rise to safety concerns that require additional efforts.

Solid Oxide Electrolysis Cell

Operating within the temperature range of 500 to 850 °C, SOEC is a type of high-temperature water electrolysis technology. Based on the type of electrolyte employed, SOEC can be categorized as either oxygen-conducting (O-SOEC) or proton-conducting (H-SOEC) [23]. O-SOEC typically employs steam as feedstock. Steam is oxidized on the cathode to generate

hydrogen and oxygen ions. The produced oxygen ions then transport across the electrolyte to the anode side to release electrons and produce oxygen. For H-SOEC, protons are generated by water oxidization on the anode along with oxygen, which then migrate to the cathode through the pure proton-conducting electrolyte and form hydrogen on the cathode. In accordance with thermodynamics, the high operating temperatures endow SOEC with a diminished requirement for electrical energy in the process of water splitting and improved productivity and energy conversion efficiency, offset by the utilization of heat, thereby leading to a substantial reduction in hydrogen production costs. Another advantage is that non-noble-metal catalysts can be utilized to achieve the desired electrochemical performance in SOEC, eliminating the need for expensive and scarce noble metal materials [24]. Compared to O-SOEC, H-SOEC could offer some extra advantages. For example, unlike O-SOEC, H-SOEC could obtain dry and pure H_2 at the cathode side without additional treatment, as stream is fed with anode side [25]. Besides, the operation temperature of H-SOEC is typically lower than that of O-SOEC due to the high ion conductivity and lower activation energy of proton conductors at relatively moderate temperatures (500 to 700 °C). Lower temperatures allow for the use of cost-effective materials for balance-of-plant and interconnects and contribute to an extended system lifespan. For seawater electrolysis, the high operating temperature (compared to room temperature water electrolysis technologies) confers upon the SOEC the capacity to overcome the challenges posed by the intricate composition of seawater. Since the working temperature of SOEC typically exceeds 500 °C, the seawater feedstock can be converted into salt- and impurities-free water vapor, thereby mitigating the bad effects of the sea salt on the electrolyser and achieving enhanced energy conversion efficiency [26]. While these advantages bode well for the technological future of SOEC, its application is impeded by the high manufacturing and maintenance costs, as well as elevated energy consumption. The longevity of parts and components in the SOEC is vulnerable to

oxidation and corrosion, especially the deterioration of the electrolyser components due to impurities when fed with seawater, during prolonged high-temperature operation. Moreover, the high operating temperatures present challenges for the sealing of the stack, as the sealing material must withstand oxidation reactions in the anode region and reduction reactions in the cathode region. Additionally, it is crucial to consider the thermal stress and heat distribution within the cell over extended periods of operation. Furthermore, the SOEC is not as mature as other electrolysis technologies, and there are limited reports on its direct utilization for seawater electrolysis, necessitating extensive development.

Proton Exchange Membrane Water Electrolysis

The research on the proton exchange membrane (PEM) electrolysis can date back to the 1950s, when the proton-conducting polymer membranes were used as sold electrolyte to replace liquid electrolyte [20]. The proton exchange membrane is a type of perfluoroalkylsulfonic acid (PFSA) type polymer membrane (such as Nafion, Flemion, and Aquivion) with a thickness of 50-250 μm, acting to conduct protons and separate the gaseous products. In a typical PEMWE single cell, the PEM is sandwiched by anodic and cathodic catalyst layers (CLs), with gas diffusion layers (GDLs) and bipolar plates positioned in close proximity on both sides. The operating principle of PEMWE can be described as that pure water is input and reaches the anodic CL. Water molecules are then oxidized to generate protons (H^+), oxygen molecules, and electrons. The produced protons pass through the polymer electrolyte membrane along with the electrons to the cathodic CL, which are then reduced to generate molecular hydrogen [27]. Although the feedstock is pH-neutral pure water, when saturated with water, the PEM undergoes swelling and assumes a protonic form, which is equivalent to a 0.5-1.0 M H_2SO_4 solution. Therefore, the circulated water transitions into an acidic solution with a pH ranging from 3.4-5.6 during operation, which requires high level

of acid resistance capability for each component over the long-term operation. PEMWEs could deliver a current density higher than 2.0 A cm^{-2} with a rapid response. The in-situ-formed acidic environment endows PEMWE with high HER kinetics. Besides, the purity of the produced hydrogen by PEMWEs is as high as 99.999 vol%. In addition, the high ionic conductivity and current density also serve to prolong the cycle life of PEMWEs by inhibiting the formation of contaminants such as carbonates. Furthermore, PEMWE cells exhibit a comparable configuration to that of PEM fuel cells (PEMFCs), which could potentially facilitate a more compact design for energy storage and conversion systems. All these merits contribute to positioning PEMWEs as a promising technology in the pursuit of sustainable energy objectives. However, due to its operation in an acidic environment, PEMWE necessitates the use of noble metals such as Ir, Ru, and Ti as catalysts, GDLs, and bipolar plates, resulting in elevated costs. The substantial investment and operating costs have hindered PEMWE from achieving significant market penetration in the past few years. To meet the energy efficiency and stability requirements, PEMWE necessitates highly purified freshwater as feedstock. When PEMWE is employed for seawater electrolysis, only the anode is supplied with seawater to prevent precipitation at the cathode, but the impurities will also contaminate the costly membranes. Additionally, the formation of chlorine gas and other oxychlorides resulting from active chlorine electrochemistry in acidic conditions could lead to corrosion of the membranes, catalysts, bipolar plates, and other components, thereby diminishing the efficiency and lifespan of the electrolysers. Moreover, the presence of Na^+ may compete with protons across the membrane, potentially leading to instability as protons are unable to be efficiently transferred to the cathode, reducing the local pH of the anode and increasing Nernst overpotential.

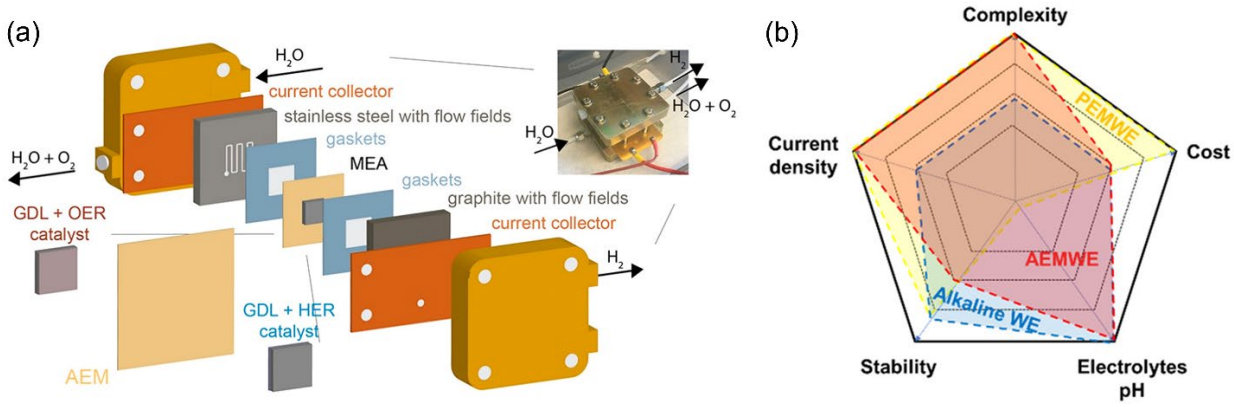

Figure 1.3 (a) The electrolyser components of AEMWE. (b) Radar map comparing the key parameters of the water electrolysis technologies [28, 29].

Anion Exchange Membrane Water Electrolysis

AEMWE is an emerging technology that has the potential to efficiently and cost-effectively produce hydrogen by leveraging the benefits of PEMWE and AWE [30]. The main constituents of the AEMWE cell are similar to that of PEMWE, with electrolyte membrane changes from proton exchange membrane to the anion exchange membrane, as can be shown in **Figure 1.3a**. The working principle of AEMWE can be described as that water or alkaline electrolyte solution is fed to the cathode, where water molecule is reduced to hydrogen and OH^- ions. The OH^- ions migrate through the anion exchange membrane to the anode, generating oxygen and releasing four electrons. AEMWEs possess some of the advantages of PEMWEs, including low resistance cell configuration and high gas purity. Besides, AEMWEs could also offer certain advantages that are not applicable to PEMWEs. For example, operating under alkaline conditions, AEMWEs accommodate the utilization of inexpensive non-precious metal catalysts and cell materials, leading to significant cost reductions. The alkaline condition of AEMWE is also conducive to facilitating the kinetically sluggish OER while suppressing ClER. Like AWE, the cations (Ca^{2+}/Mg^{2+}) can be pre-

precepted to avoid the blockage and fouling of the electrode and membranes for sweater electrolysis. Furthermore, membranes and ionomers in AEMWEs are typically fabricated with hydrocarbon backbones and cationic groups to facilitate hydroxide ion conduction, offering a more economically and environmentally advantageous alternative to the perfluorinated membranes used in PEMWEs, such as Nafion™, which emit hydrogen fluoride (HF) upon chemical decomposition In comparison to AWE, AEMWE still presents several advantages,, including the utilization of a more moderate condition (1 M KOH solution), a more compact design, higher energy density, and increased hydrogen purity. **Figure 1.3b** illustrates a comparison of the key parameters of water electrolysis between AEMWE and two other room-temperature technologies, namely AWE and PEMWE, emphasizing the comprehensive advantages of AEMWE. Therefore, AEMWE represents a promising and practically viable hydrogen production technology. Typically, the operating temperature of AEMWE typically surpasses ambient temperature in an industrial setting. The elevated temperature can improve ion transport in the solution and electrode reaction kinetics, consequently reducing both the ohmic and activation overpotentials [31]. However, the elevated temperature also accelerates membrane degradation and leads to performance deterioration. Consequently, the operational temperature for AEMWE typically ranges from 40 to 70 °C. The AEMWE process is its current status in the Research and Development (R&D) stage, in contrast to the PEMWE. The primary challenge for AEMWE lies in achieving long-term stability and operation at high current density [32]. In this regard, the advancement of more efficient electrocatalysts and membranes are primary research objectives to expedite the progress of AEMWE technology.

Other Innovative Electrolysers

Except for the above-mentioned technologies, some emerging and innovative electrolysers in recent years have been developed for water or seawater electrolysis. Bipolar membrane water electrolyser (BPMWE) is an early-stage technology for hydrogen production, comprising a polymeric cation-exchange layer (CEL) and an anion-exchange layer (AEL) [33]. BPMWE enable the coupling of distinct pH environments within a single electrolyser, allowing for the independent selection of optimal pH conditions for each half-reaction [34]. In BPMWE, water is spit at the interface between the two membranes, where OH^- migrates through AEL, and protons migrates through CEL. BPMWE is highly promising for sweater electrolysis. For instance, Jaramillo and co-workers have elaborately employed BMP to design an asymmetric BPMWE for seawater electrolysis and achieved long-term high-current hydrogen production [35]. The CEL layer can hinder the membrane crossover transfer of cathodic Cl^-, preventing it from competing with the anodic OER and affecting the overall efficiency of the electrolyser. The cation was transported from the cathode to CEL and catalyst layer, which was then blocked by the Donnan exclusion effect of AEL. Thereout, the exquisite application of BPM realized purification of saline water by mitigating the transmission of undesirable ion crossovers. The reason for the failure of introducing real seawater for both electrodes is that in the anode, the Cl^- within seawater could easily transport across the AEL and competitively oxidize in the catalyst layer to produce corrosive OCl^- species, which significantly affects the efficiency and durability of the system. This highlights the limitation of BPM for full seawater electrolysis. Other soluble and insoluble impurities within seawater can also contribute substantially to the dissatisfactory stability. Besides, as reported previously, one of the prominent problems with BPM is that the utilization of two pieces of membranes will result in a significant increase in internal resistance, which is why BPMWE requires a much

higher operation voltage than monopolar electrolysers. While the BPMWE strategy opens a new avenue for seawater electrolysis, it still has two drawbacks which need further addressing. First, a high cell voltage (>3 V) is needed to sustain a small current density of 250 mA cm^{-2}, far exceeding the cell voltages reported in existing studies for achieving the same current density under similar conditions. In addition, a large mass loading of noble metal catalysts is used.

Given its high energy efficiency, hydrogen purity, and the potential for utilizing non-precious metal catalysts, as well as the alkaline conditions conducive to facilitating OER and suppressing ClER, this thesis adopts AEMWE to assess the practical application of the developed electrocatalysts.

1.3 Overview of Oxygen Evolution Reaction

1.3.1 Reaction Mechanisms of OER

OER involves a series of complex and interconnected multi-step processes, including the formation and evolution of various intermediate species, the transfer of multiple electrons and protons, and the breaking and formation of chemical bonds. A comprehensive understanding of the reaction mechanism is paramount for the development of OER catalysts with high activity, selectivity, and stability. In the past few years, significant progress has been made in revealing and understanding the OER mechanisms, and corresponding theories have been proposed to quantify the activity-structure relationship. Currently, two mechanisms are widely accepted for describing the OER process, which are conventional adsorbate evolution mechanism (AEM) and lattice-oxygen-mediated mechanism (LOM) [36]. Typically, OH^- adsorption, OOH^- production, and O_2 release are the evolutionary pathways for AEM (**Figure**

1.4a), whereas OH^- adsorption, O–O coupling, and O_2 release are involved in LOM (**Figure 1.4b**).

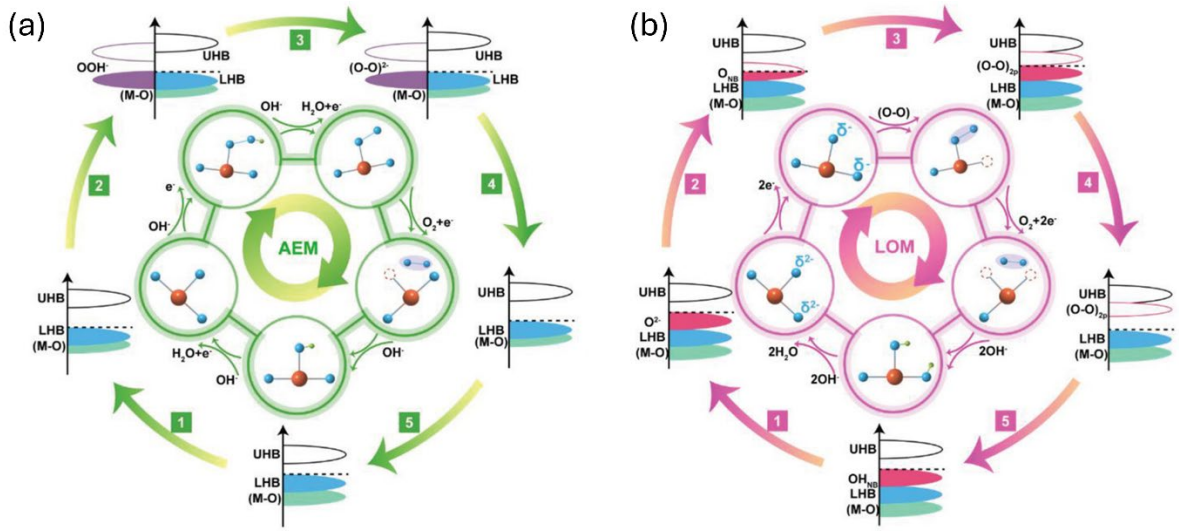

Figure 1.4 The OER mechanism involves (a) the conventional AEM route, where the metal functions as the redox center, and (b) the LOM pathway, where oxygen serves as the redox center [37].

Adsorbate Evolution Mechanism

The AEM consists of four steps in both alkaline and acidic solutions, with some variations in the reactants and products. For the OER process in an alkaline solution, a dissociative OH^- group first migrates to the catalyst surface, and an electron is removed to generate adsorbed OH* species (OH*). Subsequently, the OH* species reacts with the second OH^- to produce adsorbed O* species (O*), which further reacts with the third OH^- to form an adsorbed OOH* intermediate (OOH*). Ultimately, the OOH* species reacts with the fourth OH^- to produce O_2. In an acidic solution, the processes of water adsorption and dissociation are expected to be involved. A water molecule initially adsorbs on the catalyst surface and undergoes cleavage to form OH*, followed by deprotonation to generate O*. The resulting O* species

further reacts with another water molecule to form OOH*, which leads to the generation of O_2 through deprotonation and desorption processes.

OER under alkaline or neutral conditions:

$$OH^- + * \rightarrow OH^* + e^- \quad (1.12)$$

$$OH^- + OH^* \rightarrow H_2O + O^* + e^- \quad (1.13)$$

$$OH^- + O^* \rightarrow OOH^* + e^- \quad (1.14)$$

$$OH^- + OOH^* \rightarrow O_2 + H_2O + e^- \quad (1.15)$$

OER under acidic conditions:

$$H_2O \rightarrow OH^* + H^+ + e^- \quad (1.16)$$

$$OH^* \rightarrow O^* + H^+ + e^- \quad (1.17)$$

$$H_2O + O^* \rightarrow OOH^* + H^+ + e^- \quad (1.18)$$

$$OOH^* \rightarrow O_2^* + H^+ + e^- \quad (1.19)$$

In the above equations, * denotes surface adsorption site.

Lattice Oxygen Mechanism

Later, numerous highly active oxides were found to demonstrate pH-dependent OER activity, suggesting nonconcerted electron-proton transfer steps, in contrast to the concerted charge transfer in AEM [38]. Furthermore, several investigations have demonstrated that the generated oxygen molecules might have come via lattice oxygen evolution in addition to water molecules [39, 40]. Furthermore, certain catalysts showed significantly higher intrinsic

OER performance even if they didn't have the perfect composition according to the AEM. These phenomena therefore posed a serious challenge to the conventional AEM and its associated activity descriptors. This led to a tremendous deal of interest in creating a new OER mechanism. The first experimental proof that lattice oxygen redox chemistry is involved in oxides with high metal–oxygen bond covalency was proved by Shao-Horn et al. This type of oxygen redox chemistry route in OER was referred to as lattice oxygen-mediated mechanism. In **Figure 1.4b**, the electron transfer route of the LOM is depicted. Initially, the first two steps are like the AEM to generate O*. Next, when O* is directly coupled with the lattice oxygen within the catalysts, an O–O bond is formed, and oxygen molecules is released. Lattice oxygen is consumed in this process to generate oxygen vacancies to act as the active sites for OER electrocatalysis, which are then filled by OH^- in solution migrating into the voids. Without the formation of the OOH* in the LOM mechanism, a faster reaction kinetics and a lower overpotential than AEM can be expected due to the direct O–O coupling. The scaling relationship between OH* and OOH* in the conventional adsorbent release mechanism is not applicable. Therefore, LOM can surpass the overpotential limitation (0.37 V) of the scaling relation in AEM.

Based on LOM, recent studies have proposed several popular OER paths via LOM with various active centers [41]. In order to successfully initiate the LOM pathway, lattice oxygen activation is required. The activation of the lattice oxygen allows it to easily serve as an active site, which is referred to as the oxygen-vacancy-site mechanism (OVSM, **Figure 1.5a**). An alternative approach pathway utilizing a single metal site as the catalytic center to adsorb OH^- and proceeds through the deprotonation step, known as the single-metal-site mechanism (SMSM, **Figure 1.5b**). The high-valence metal cations benefit energetically from the direct coupling of the O* intermediate and activated lattice oxygen, which is made possible by the

surface reconstruction process. The produced OO* species can be seen as a freshly created O2 molecule that will experience next oxygen production. In addition, the dual-metal-site mechanism (DMSM, **Figure 1.5c**) involves the adjacent activated lattice oxygen intramolecularly coupling to generate M–OO–M species. There has been reports on metal (oxy)hydroxides with structural flexibility proceeds with DMSM.

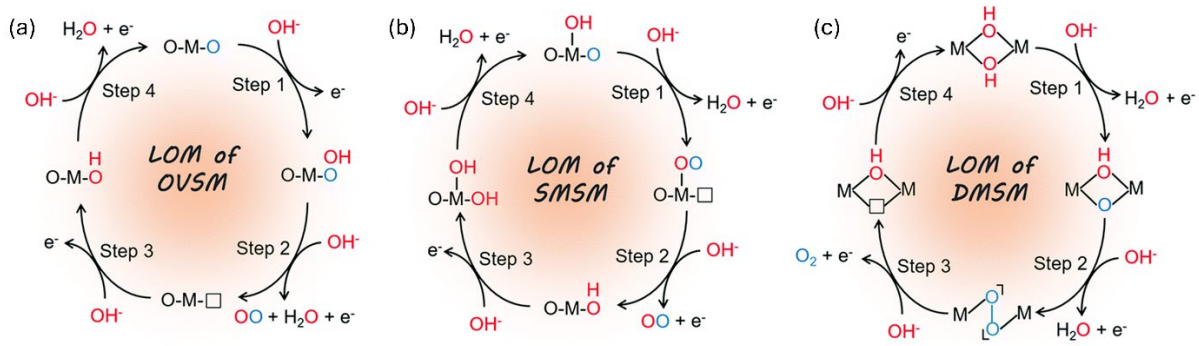

Figure 1.5 Three potential LOM routes in alkaline conditions with distinct catalytic sites, which are (a) oxygen-vacancy-site mechanism (OVSM), (b) single-metal-site mechanism (SMSM), and (c) dual-metal-site mechanism (DMSM) [36].

The electrocatalyst surface becomes metastable due to the oxidation and exchange of lattice oxygen in the LOM process, facilitating structural reconstruction [42]. When the OER proceeds through LOM, abundant oxygen vacancies will be formed on the surface of the electrocatalysts. Since the replenishment of surface vacancies happens much more slowly than their production, the real catalytic species of TM oxyhydroxides will be produced by the leaching of surface cations and dynamic structural rebuilding. As a result, the electrocatalysts based on LOM are regarded as pre-catalysts [43]. There are several direct/indirect methods to identify the LOM mechanism, including measuring pH-dependent OER activity, introducing tetraalkylammonium cation (TMA^+) as an indicator of an active surface lattice oxygen, and isotope oxygen (^{18}O and ^{16}O) detection. Besides, considering that the electronic states of the

surface reconstructed structure are crucial in directing the reaction process, in situ/operando characterization technologies are highly demanded.

1.3.2 Activity Descriptors for OER

To better predict, screen, and design effective catalysts for OER, a series of descriptors which describes the structure–activity relationship of the catalyst have been proposed in the past few years, including M−OH bond dissociation energy, the reaction step energy ($\Delta G_{O*}-\Delta G_{HO*}$), and the electronic structure parameters such as d-orbital occupation, e_g orbital filling, and O p-band center. Here, we select the e_g orbital occupancy, one of the most popular descriptors for TM oxides, to illustrate how relationship of the descriptor and the OER activity.

The electrons filling degree of e_g orbital is typically applicable to TM oxide (TMO) electrocatalysts, such as spinel, perovskite, and mullite. In 1977, Matsumoto et al. first utilized the overlap integral between the e_g filling of the TMs and the σ_{sp} orbital of the oxygen molecule as a descriptor [44]. More recently, Shao-horn's group demonstrated a quantitative relationship between the e_g occupancy of the 3d electrons and the OER activity of perovskite catalysts [45]. Assuming that the oxygen in OER adsorbates is bonded to the B-site TM in perovskites, they found that an e_g orbital occupancy close to unity yields optimal OER activity due to the 3d orbital of B-site metal overlaps with the O 2p orbital, thus changing bonding energy between surface and absorbates [46]. An excessive amount of e_g orbital occupancy slows down O-O bond formation rate in OOH adsorbate, while insufficient eg filling prevents OOH from deprotonating and forms O_2^{2-}ions [47]. Based on this descriptor, $Ba_{0.5}Sr_{0.5}Co_{0.8}Fe_{0.2}O_{3-\delta}$ (BSCF) with an e_g orbital occupancy of approximately 1.2 could potentially exhibit an activity at least an order of magnitude higher than that of the

benchmark material IrO_2. Subsequently, e_g orbital occupancy was also utilized as an OER activity descriptor for spinel and other oxide electrocatalysts.

Typically, e_g filling of the TMO can be adjusted by altering the oxidation state or spin state of the TM cation. The electron numbers in the 3d orbital can be altered through changing the oxidation state of the TMs. For example, Fe^{4+} ($3d^4$) indicates a $t_{2g}^3e_g^1$ configuration with a high spin state, while its less oxidized form, Fe^{3+} ($3d^5$), exhibits a $t_{2g}^3e_g^2$ configuration. Similarly, Ni^{3+} ($3d^7$) has an occupancy of $t_{2g}^6e_g^1$ with a low-spin state, whereas Ni^{2+} ($3d^8$) presents a $t_{2g}^6e_g^2$ configuration. Introducing dopant elements with varying oxidation states and electronegativities, or engineering vacancies, can regulate the 3d electron occupancy and the oxidation state of the TMs, thereby influencing the OER performance. Vacancy engineering can reduce the oxidation state in accordance with the electron-neutral principle and enhance the e_g occupancy. Modifying the spin state can also regulate e_g fillings. For instance, Co^{3+} with an electron configuration of $t_{2g}^6e_g^0$ in a low spin state exhibits moderate activity, while altering its electron configuration to $t_{2g}^5e_g^1$ (intermediate spin state) could intrinsically enhance its OER activity. There are several strategies to adjust the spin state of TM cations, such as substitution, strain engineering, and nanostructuring.

1.3.3 Measurement Criteria for OER

Benchmarking parameters are necessary for the assessment of OER electrocatalytic performance in order to improve comparisons across various systems. Several commonly acknowledged essential evaluation parameters have been summed up as follows.

Overpotential (η)

The overpotential (η), one of the most important parameters for assessing the OER activity of a designated electrocatalyst, is defined as the potential difference between the potential at a specific current density and the equilibrium potential (1.23 V). In practical, η denotes the value that must be applied to attain a specified current density, typically 10 mA cm^{-2}, stemmed from the 12.3% photochemical water decomposition efficiency. To a certain degree, a lower overpotential corresponds to a reduced reaction barrier to overcome and an enhanced catalytic performance of the electrocatalyst. It is noteworthy that some OER electrocatalysts, such as nickel-based and cobalt-based materials, demonstrate pronounced redox peaks in the potential range slightly above 1.23 V. To accurately determine the overpotential value, it is essential to distinguish the redox peak current from the OER current. Overpotential at elevated specific current densities can be chosen for comparison. Furthermore, the values reported in numerous studies represent the overpotential after iR compensation. Nevertheless, the iR-corrected overpotential is insufficient in characterizing an authentic water electrolysis system. Therefore, the utilization of iR uncompensated overpotential is also essential.

Tafel Slope

The Tafel slope serves as a crucial indicator for reflecting the intrinsic activity of a catalyst and holds significant importance in investigating the OER mechanism. The Tafel equation is derived from the renowned Butler-Volmer equation, establishing a logarithmic relationship between overpotential and current density:

$$\eta = a + b \times \log (j) \tag{1.20}$$

where $a = 2.303RT\log(j_0)/\alpha nF$, $b=2.303RT/\alpha nF$. b is the Tafel slope, j refers to the current density, j_0 represents the exchange current density, R stands as the ideal gas constant, T refers

to the absolute temperature, n denotes the number of transferred electrons during the redox reaction, F represents the Faraday constant, and α represents the charge transfer coefficient. Typically, a low Tafel slope (b) signifies that a small overpotential change is necessary to accommodate the swift increase in current density, thereby demonstrating exceptional electrocatalytic kinetics. The Tafel slope can be extracted from the measured anode polarization curves.

Mass and Specific Activities

When assessing the OER catalytic efficiency, particularly when taking the catalyst costs into account, the mass activity (MA), defined as the current normalized by the mass loading of the target catalyst at a particular overpotential, is becoming increasingly significant. The specific activity (SA), which is often based on the geometrical area, electrochemically active surface area (ECSA) or the Brunauer-Emmett-Teller (BET) surface area, is another critical evaluation measure for OER.

Electrochemically Active Surface Area

The ECSA is heavily reliant on several catalytic materials and electrochemical processes. ECSA can be obtained by double-layer capacitance (C_{dl}), hydrogen underpotential deposition, carbon monoxide stripping, and integrating the redox peak area. For example, C_{dl}, proportional to ECSA, can be obtained by testing the cyclic voltammogram (CV) curves under different scanning rates. It is recommended to utilize ECSA solely for comparing similar materials within the same reaction, as the assessment methodology and outcomes of ECSA may vary across different electrochemical reactions and materials [48].

Turnover Frequency

Turnover frequency (TOF) characterizes the inherent catalytic activity of a catalyst, denoting the rate at which the production of products is determined by the number of active sites. For electrocatalytic reactions involving gas release, TOF can be calculated by:

$$TOF = \frac{jN_A}{nFT}$$

where “j” denotes the current density at a specific overpotential, “N_A” represents the Avogadro constant, "n" signifies the quantity of transferred electrons in the reaction (n = 4 in the case of OER), “F” denotes the Faraday constant, and “Γ” is attributed to the concentration of active sites on the catalytic surface or the number of atoms participating in the reaction. Obviously, a higher TOF signifies superior catalytic activity of the electrocatalyst. In practice, obtaining an accurate count of active sites is challenging, especially on solid-state heterogeneous electrocatalysts. One approach involves considering all metal sites as active sites, a method that frequently yields a higher TOF than the actual value, since not all metal sites are catalytically active.

Faraday Efficiency

Faraday efficiency (FE) is another quantitative parameter that signifies the efficiency of electron utilization in the reaction, and reflects the charge transfer efficiency and selectivity of the catalyst to a certain extent, which is typically employed to determine whether unfavorable reactions have occurred. The FE of OER is the ratio between the experimental production value of oxygen and the theoretical value. In general, the theoretical yield of oxygen is assessed by chronoamperometry or chronopotentiometry analysis, while the actual

oxygen obtained can be detected by conventional water-gas displacement, gas chromatography, or fluorescence spectrometry

Stability

The assessment of stability stands as a primary criterion for evaluating catalyst performance, as it dictates the feasibility of industrial application. In many cases, achieving high stability is established on sacrificing activity. There are several approaches to assess the stability of electrocatalysts. CV cycling at high scan rates is the main method to determine the stability of electrocatalyst. When the ultimate curve aligns closely with the initial curve, or the overpotential increases by no more than 10% of the original value, it signifies that the catalyst exhibits commendable stability. Two other commonly employed strategies include chronoamperometry (I-t curve at constant potential) and chronopotentiometry (E-t curve at constant current density). The identification of a consistent current density at a given potential through chronogalvanometry, or a minimal rise in overpotential at a fixed current density through chronopotentiometry, is deemed stable for the OER catalysts or the electrolyser.

1.4 Seawater Electrolysis

Currently, commercial water electrolysis systems typically employ fresh and highly purified water for green hydrogen production. However, the resources of highly purified fresh water are rather scarce and limited, with over 80% of the global population confronted with different levels of water security risks. The highly purified fresh water is typically obtained by purification pretreatment process with additional desalination system or integrating the electrolysis system with a purification system. The extra purification/desalination systems would introduce considerable economic expenses owing to the increased costs of land,

infrastructure, maintenance, and transportation. Compared with purified fresh water, seawater is an infinite resource since seawater accounts for 97% of the global water storage. Hence, substituting freshwater with abundant seawater for hydrogen production via water electrolysis is highly advantageous. Furthermore, seawater electrolysis obviates the necessity for supplementary pretreatment purification systems, thereby simplifying the engineering of electrolysers and strengthening the economic feasibility of green hydrogen production from water. Moreover, it is also flexible to integrate renewable power generation technologies (such as wind, solar, tide, and wave) with seawater electrolysis systems. Furthermore, it has been demonstrated that seawater electrolysis holds significance for arid or coastal hyperarid regions, as this technology can yield safe and exceptionally pure drinking water. Research on seawater electrolysis dates back to 1975 [49]. However, it is only in the past two years that the research on seawater electrolysis has ushered in explosive growth.

1.4.1 Main Challenges in Seawater Electrolysis

The complexity of the chemical and biological components stands as the major challenge in seawater electrolysis research (**Figure 1.6a**). The 3.5 wt% salts containing various metallic elements within seawater would bring about many drastic competitive side reactions, while the biological species tend to form insoluble precipitates and cause block hazards to catalysts and electrolysers. One of the most notable concerns is the high concentration of chloride anions (~0.5 M), which would result in ClOR. The competition between ClOR and OER at the anode surface can have important implications for the efficiency and stability of electrolysis processes. ClOR is a two-electron-transfer process, which is kinetically more favorable than the four-electron-transfer OER.

$$2Cl^- \rightarrow Cl_2 + 2e^- \qquad E^0 = 1.36 \text{ V vs. SHE} \quad (pH = 0) \tag{1.20}$$

$$Cl^- + 2OH^- \rightarrow ClO^- + H_2O + 2e^- \quad E^0 = 0.89\ V\ vs.\ SHE \quad (pH = 14) \qquad (1.21)$$

Besides, the products of ClOR including Cl_2 or ClO^- can have detrimental effects on the performance and durability of the electrolyser components, leading to corrosion and degradation of the anode materials and other components in the system. The specific product formed of ClOR, whether Cl_2 or ClO^-, depends on the pH values of the electrolyte.

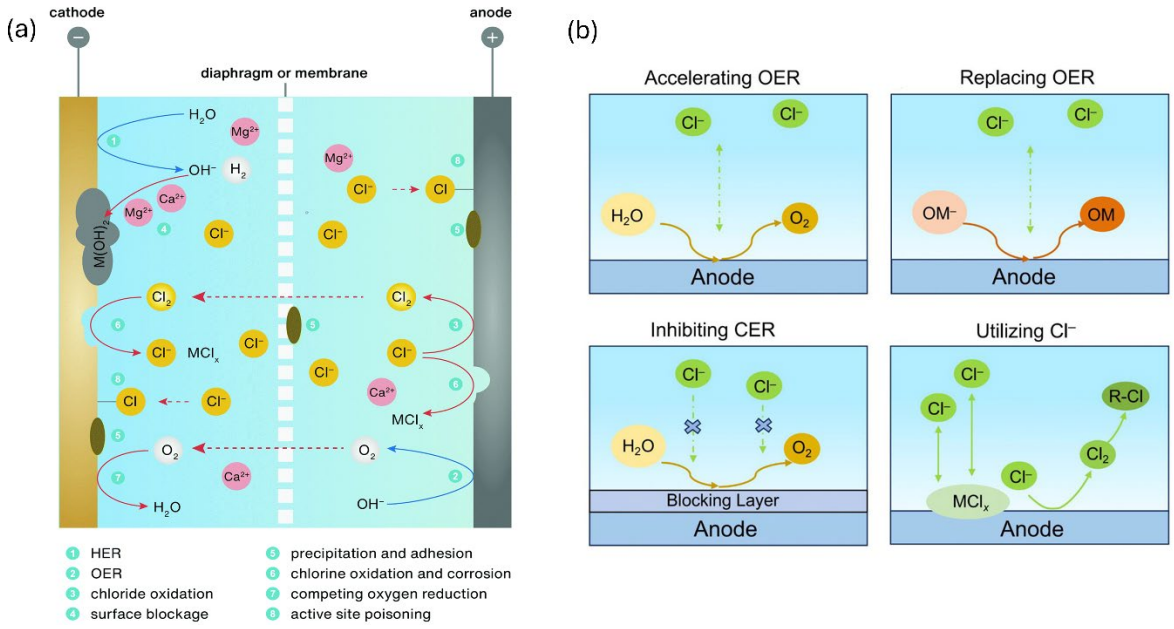

Figure 1.6 (a) Several challenges arise in seawater electrolysis due to the intricate composition of seawater [50]. (b) Different strategies for alleviating chlorine interference at anode in seawater electrolysis [51].

1.4.2 Selective OER over ClOR

Various strategies have been developed to prevent chlorine electrochemistry on the anode side to obtain excellent OER selectivity in seawater electrolysis, including accelerating OER by employing highly efficient catalysts, replacing OER by a more thermodynamically advantageous electrooxidation reaction such as urea oxidation reaction, impeding ClOR by

adding a blocking layer on the anode surface, and using Cl^- within the catalysts to quickly eliminate the distributed Cl^- species close to the surface (**Figure 1.6b**).

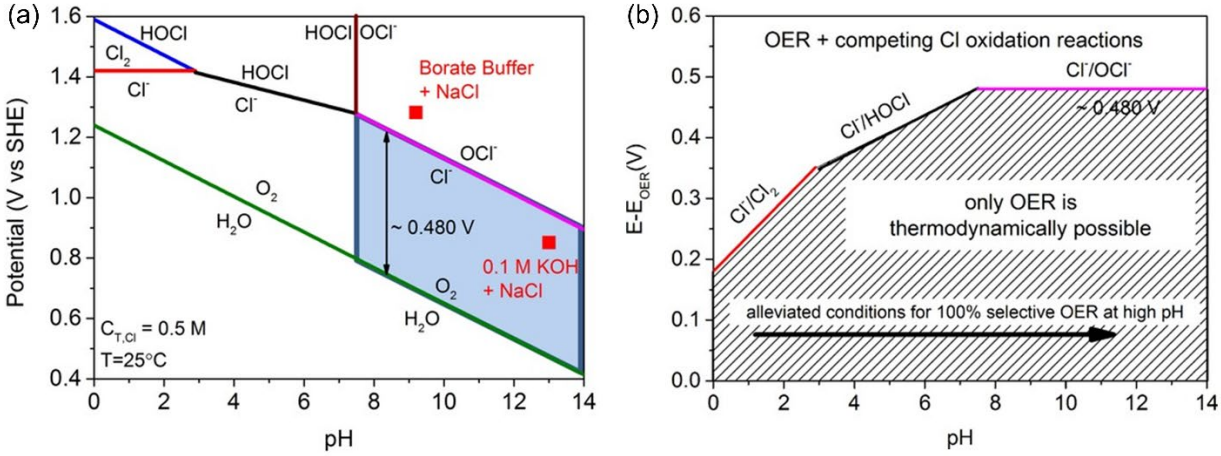

Figure 1.7 (a) The Pourbaix diagram pertaining to OER and the chloride electrochemistry in an aqueous saline electrolyte (0.5 M NaCl). (b) Overpotential ranges of oxygen and chloride electrochemistry at various pH levels.

Among these strategies, employing highly efficient catalysts to facilitate OER is an optimal approach to enhance OER selectivity and mitigate ClOR considering the well-established research foundation of OER. In 2016, Peter and his group members proposed a Pourbaix diagram to describe the chlorine electrochemistry and OER under different pH values in simulated seawater (**Figure 1.7a**) [19]. At lower pH values, ClOR can lead to the formation of chlorine gas (Cl_2), which is highly corrosive and can pose significant challenges for the long-term operation of the electrolysis system. On the other hand, at higher pH values (pH >7.5), ClOR can result in the formation of hypochlorite ions (ClO^-), which also have corrosive properties and can contribute to the degradation of the electrolyser components. However, there is an equilibrium potential difference of 480 mV between OER and ClOR at alkaline electrolyte, which indicates that ClOR can be suppressed by controlling the anodic overpotential lower than 480 mV under alkaline condition, allowing for selective OER

(**Figure 1.7b**). Hence, expanding the operational potential difference between OER and ClOR is essential to prevent the generation of corrosive and hazardous products of chlorine electrochemistry during seawater electrolysis. Developing highly active and electrochemically stable catalysts for OER is thus of paramount importance for improving OER selectivity for seawater electrolysis [52].

1.5 Transition Metal-Based Electrocatalysts for Accelerating OER

Currently, industrial electrocatalysts towards OER are mainly noble based materials, such as Ir- and Ru- based catalysts [53]. However, the scarcity, high costs, and inferior stability significantly impede their widespread commercialization. Therefore, noble-metal-free-based (mainly TM including Mn, Fe, Co, and Ni) electrocatalysts, which can be classified as alloys, oxides, hydroxides/layered double hydroxides, phosphates/borates, and chalcogenides, have been widely explored as high-performance, cost-effective, and robust OER catalysts [48]. The advancement of highly efficient catalysts capable of achieving OER selectivity at reduced overpotential, irrespective of the existence of chlorine ions in seawater, represents an optimal approach to circumvent ClOR. Various TM-based electrocatalysts have been extensively investigated for enhancing OER selectivity owing to their heightened activity in alkaline environments.

1.5.1 Layered Double Hydroxides

Structure and Properties

As typical layered-type catalysts, hydroxides/layered double hydroxides (LDHs), primarily composed of first-row TMs (Fe, Co, Ni, Mn, etc.), exhibit exceptional activity for OER and have attracted enormous attention in recent years [54]. The typical crystal structure of the

layered catalysts consists of layers of interconnected MO_6 (through edge sharing) with H^+ stacked on top of each other, forming the 2-D layered structure. In comparison, LDHs suggest bigger interlayer distance due to the intercalation of various anions and water molecules in the layers. Composed of brucite-like positively charged layers and anion ligands within the layers, LDH can be denoted with a formula of $[M_{1-x}^{2+}M_x^{3+}(OH)_2]^{x+}(A_{x/n}^{n-})\cdot mH_2O$, in which M^{2+} represents divalent metal ions such as Ni^{2+}, Fe^{2+}, Cu^{2+}, and Co^{2+}, M^{3+} is trivalent metal ions such as Fe^{3+}, Mn^{3+}, and Al^{3+}, and A is the interlayer anions such as CO_3^{2-}, NO^{3-}, SO_4^{2-}, and Cl^-). Due to the existence of divalent meta ions and trivalent mental ions within the MO_6 octahedral, the brucite layers are positively charged, while the charge neutrality is maintained by interlaminar anions. LDH materials offer several advantages for water/seawater electrolysis. Firstly, the layered structure is susceptible to delamination into ultra-thin nanosheets, thereby exposing more active sites to enhance electrocatalytic activity. Secondly, the compositional flexibility in both cations and anions, as well as the tunable interlayer distance, provides LDHs with the capability to customize designs for desired activity, stability, conductivity, and selectivity. Thirdly, LDHs enable the utilization of earth-abundant and cost-effective elements, offering significant potential for large-scale applications. Lastly, the alkaline conditions in water/seawater electrolysis inherently favor the stable existence of LDH. In recent years, extensive research has been dedicated to the employment of LDH-based materials as efficient electrocatalysts towards water/seawater electrolysis, with the prominent activity of LDH-based materials being widely demonstrated, especially for OER. Since the fundamental research based on NiFe LDH has achieved considerable progress, recent studies have been dedicated to further optimizing its catalytic performance by doping heteroatoms, constructing compounds, and interlayer anion replacement, etc. The design strategies and recent progress of LDH-based materials are reviewed, along with its application in water/seawater electrolysis.

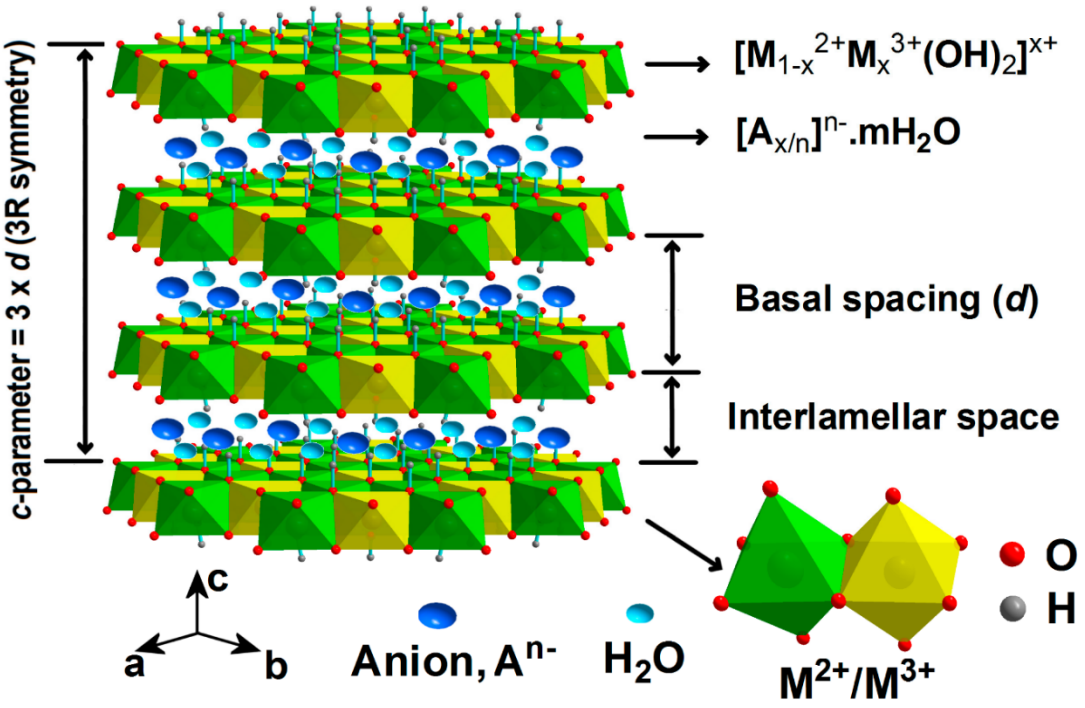

Figure 1.8 Schematic diagram of the classical LDH structure [55].

The versatile composition of LDHs enables the broad selection of cations and anions and imparts them with distinctive catalytic activities when active components are appropriately positioned within the structure. The heteroatom doping could regulate the morphology, the electronic structures, and electrical conductivity of the LDHs, thus enhancing the electrocatalytic activity [56]. Therefore, heteroatom doping is regarded as an effective method to improve the performance of electrocatalysts. In the past few years, various binary and ternary LDH materials have been developed as efficient catalysts for extensive energy conversion and storage applications, including NiFe-LDH, MgAl-LDH, CoFe-LDH, NiCoFe-LDH, and MgAlFe-LDH. Besides, it has been reported that for many catalysts, the LDH generated during OER operation is the actual active species under alkaline OER conditions. Among various LDHs, NiFe-LDH emerges as one of the best-known catalysts for alkaline OER [57]. Ni-Fe LDH consists of a brucite-like host layer comprising nickel oxide octahedra coordinated by hydroxyl groups, with a portion of Fe^{2+}/Fe^{3+} substituting at Ni sites, with the

surplus positive charges are counterbalanced by exchangeable charge-balancing interlayer anions. Given the advantages of the synergistic effect between Ni and Fe elements, NiFe LDH has attracted much attention in recent years for its attractive electrocatalytic performance. Although bimetal LDHs exhibit catalytic activity towards OER, they have not yet reached their optimal state, which could potentially be enhanced through the introduction of a third type of metal doping to form ternary structure. Typically, elements such as Co, V, Mn, and Zn have been found to modulate the band structure by reducing the bandgap to enhance electrical conductivity, while dopants such as Cr, Co, and Mn are utilized to increase the electronic density over Fe and Ni atoms and modify their absorption capacity. Recently, the introduction of Ce into the NiFe LDHs has been demonstrated to induce lattice defects and enhance electron interactions, thereby effectively enhancing the OER catalytic performance.

Combining LDH and other materials to construct hybrid materials is a highly promising strategy to achieve superior catalytic performance towards OER, since the heterostructure between LDH and other catalysts provides increased active sites for the reaction and creates a more favorable interface, and the synergistic interactions between these two materials could enhance the electrochemical performance. In seawater electrolysis, heterogeneous structures can optimize interface properties and fully utilize various components. Zhan's group integrated NiFe-LDH with $FeNi_2S_4$ to form a heterostructure, which were then utilized as an electrocatalyst for seawater electrolysis [58]. It is suggested that the obtained heterostructure exhibits incomplete hexagonal structures with rough surfaces and edges. The heterostructure enhances the interactions between NiFe-LDH and $FeNi_2S_4$, while also offering a greater surface area and additional catalytic sites. The density functional theory (DFT) calculations reveal that the $FeNi_2S_4$ accumulates electrons, whereas the NiFe-LDH absorbs electrons,

signifying a substantial electron interaction between the two phases. Typically, there are abundant defects or vacancies at the boundaries between LDH and another species, which could act as active sites. Defects can also induce synergies, robust electronic interactions, or support effects, thereby improving the charge transfer efficiency between the electrocatalyst, electrolyte, and gas-phase interfaces. Owing to its unique redox properties (Ce^{4+} to Ce^{3+}), CeO_2 possesses abundant oxygen vacancies and exhibits effective performance in catalytic reactions [59]. When combined with the electrocatalyst, the presence of oxygen vacancies at the CeO_2 surface interface enhances the OER performance of the sample. Numerous studies have demonstrated that the stability and activity of electrocatalysts can be substantially enhanced with the support of CeO_2 [60]. It has been reported that the heterostructure between NiFe-LDH and CeO_2 could induce an enhancement of the electronic conductivity [61]. Xia et al. proposed a heterostructure between NiFeCr LDH and CeO_2 and employs DFT calculation to demonstrate that the interaction between NFC and CeO_2 will generate a d-f electron ladder through the subtle gap between the Ce-4f and 3d orbitals of Fe/Cr, thus facilitating the electron transfer rate. Furthermore, the incorporation of CeO_2 notably enhanced the oxygen diffusion coefficient, thereby facilitating kinetics [62].

1.5.2 Oxides

Compared to other catalysts, including sulfides, selenides, and nitrates, oxides are more thermodynamically stable under the oxidizing conditions during OER [63]. According to the crystallographic structure, metal oxide electrocatalysts with outstanding OER activity can be mainly classified as spinel, perovskite, and fluorite type oxides.

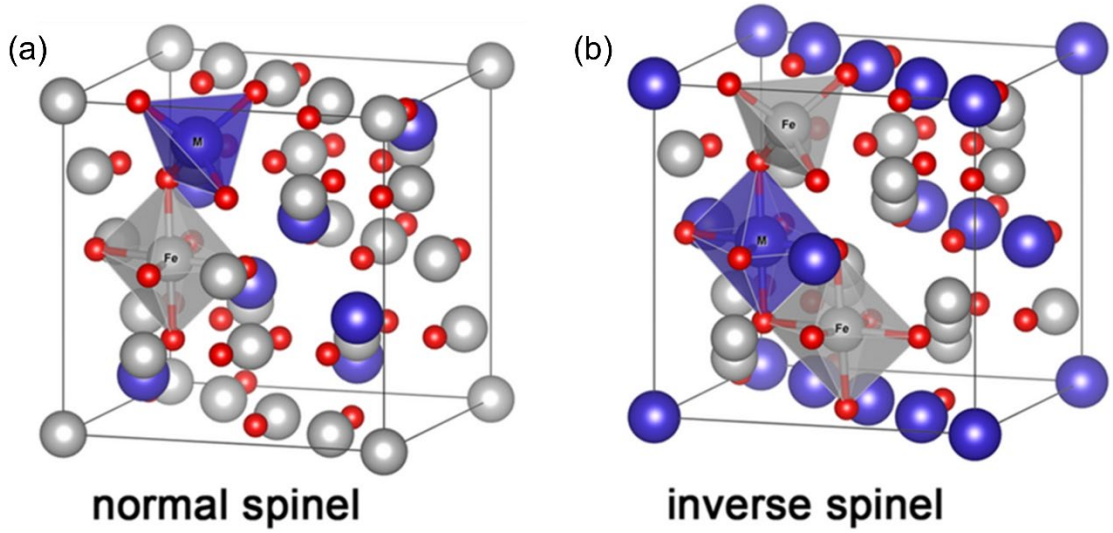

Figure 1.9 The crystal structure of (a) normal spinel ferrite and (b) inverse spinel ferrite [64].

Spinel Oxides

Spinel oxides with the general formula of AB_2O_4 exhibit a structure by a vertex connection of 1/3 A-O tetrahedrons with 2/3 B-O octahedrons [65]. Cation A^{2+} is situated at the tetrahedral position, while cation B^{3+} occupies the octahedral position. The same element can occupy both A and B sites, such as Co_3O_4. Typically, the cations in the octahedral site contribute to the performance of OER, while the cations at the tetrahedral site show moderate roles. In addition, there is an inverse spinel structure that cation A^{2+} occupies the octahedral sites, while half of the cation B^{3+} situates at the tetrahedral sites and the other half exists in the octahedral sites. Spinel oxides typically demonstrate favorable electrical conductivity due to the potential for electron jumps between the different oxidation states of A^{2+} and B^{3+}. The OER performance of spinel materials is greatly influenced by the composition, structure, distribution, and oxidation state of the cations. In the past few years, the 3d TM spinel materials and their derivatives have been extensively investigated as highly active OER electrocatalysts [66]. The electrocatalytic performance of the spinel materials and their derivatives can be optimized by various strategies. For instance, the intrinsic activity can be

improved by regulating electronic structure through changing the surface adsorption free energies. Modifying the electronic structure can be accomplished through the creation of defects/vacancies and heteroatom substitution, which has been extensively employed for electrocatalysts optimization. In addition, size and morphology regulation of the spinel materials can pose a positive effect on the electrochemical performance of OER through mass diffusion and charge transfer optimization. Moreover, integrating spinel with conductive substrates or other active materials is also an attractive way to improve OER performance.

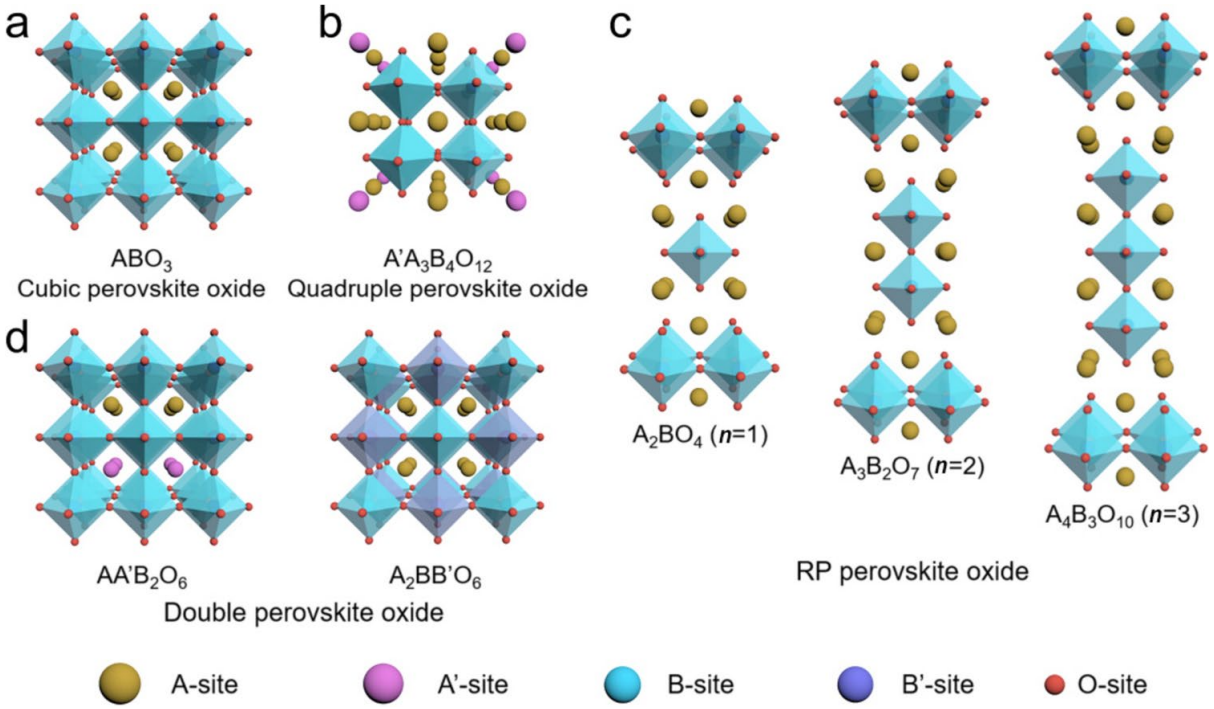

Figure 1.10 The crystal structures of various perovskite oxides: (a) single, (b) quadruple, (c) Ruddlesden–Popper layered, and (d) double perovskite oxides [67].

Perovskite Oxides

The crystal structure of perovskite oxides is more complicated than spinel oxides. In fact, approximately 90% of the metallic elements in the periodic table can be accommodated by the perovskite structure, providing significant flexibility for tailoring their physical and

chemical properties [68]. The general formula of perovskites can be denoted as ABO_3, where A stands as alkaline, alkaline-earth, or rare-earth elements, while B is typically transitioning metal cation. Since substituting heteroatoms in A and/or B site may lead to distortions and oxygen nonstoichiometric for the crystal structure, a more general formula $A_{1-x}A'_xB_{1-y}B'_yO_{3\pm\delta}$ is frequently used. TM B occupies the center of the octahedron that is connected by angles, with A fills the open space. Typically, the oxidation state of the element at B site can be +3, +4, or a combination of +3 and +4, depending on the oxidation state of A. The electronic structure of perovskite oxides can be regulated due to the high flexibility of perovskite composition and crystal structure [69]. Perovskite oxides have various structures owing to the variable composition and flexible crystal structures, which are single perovskite (ABO_3), double perovskite ($A'A''B'B''O_6$), quadruple perovskite $A'A''A'''B'B''B'''O_9$), Ruddlesden–Popper layered perovskite ($A_{n+1}B_nX_{3n+1}$, n is the number of the octahedral layers), as can be seen in **Figure 1.10** [67]. Other structures of perovskites can be considered as derivatives of the single perovskite structure. For example, when A or B, or both are occupied by two or more different cations, these cations exhibit long-range order within each subnetwork, resulting in the formation of a “double perovskite”. The formula for a double perovskite can be expressed as A-site ordered structure $A'A''B_2O_6$, B-site ordered structure $A_2B'B''O_6$, or A- and B- site ordered structure $A'A''B'B''O_6$. Double perovskite oxides have been reported to offer distinct advantages, such as a faster oxygen ion diffusion rate, enhanced surface oxygen exchange, and higher electrical conductivity [70]. Taking a B-site ordered double perovskite as an example, its formation begins with doubling the simple ABO3 unit, followed by the replacement of one of the B sites with another element B', resulting in the A2BB'O6 structure [71]. In general, adjusting BB' site is regarded as an effective way for regulate OER performance since it could BB' site optimize the d-band center to Fermi level. For double perovskite, when the oxidation state of the A-site is +2, the B-site cation may exhibit an

average oxidation state of +4 through a combination of B+4/B′+4, B+3/B′+5, and B+2/B′+6. Conversely, when the A-site cation suggests a valence state of +3, the B-site will have an average valence state of +3, realized by several combinations of B+3/B′+3, B+2/B′+4. Furthermore, numerous phase transitions have been observed as a result of the distortion of the BO_6 octahedron caused by the nonstoichiometry of oxygen and the varying sizes of A and B site cations within the structure. Essentially, the crystal structure and morphology of double perovskite oxides depend on their synthesis methods, which subsequently impacts their catalytic properties [72].

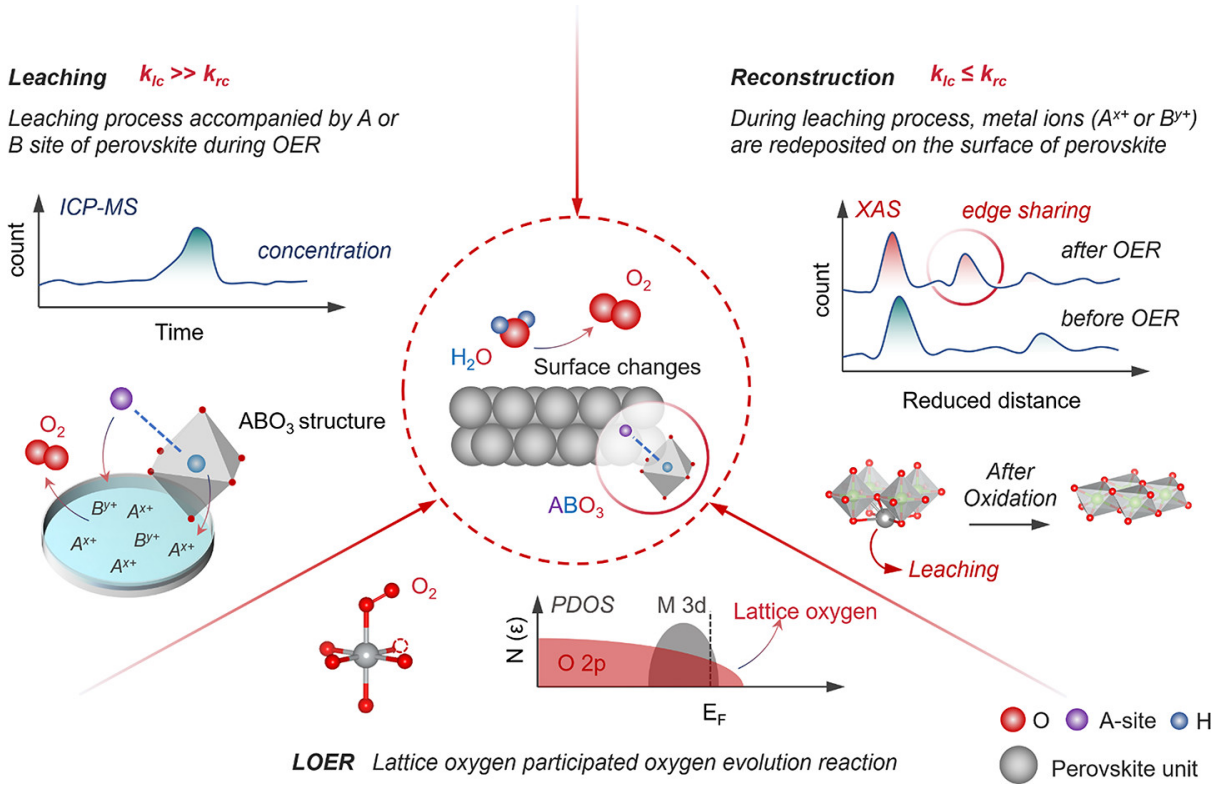

Figure 1.11 Surface changes of perovskite during OER [46].

It is widely recognized that most of the electrochemical reactions take place at the complex solid-liquid interfaces where solvent effects, the coordination environment, and the atomic active site will exert influence. During the OER process, the perovskite surface typically

undergoes changes such as leaching, reconstruction, as well as alterations of the active sites and coordination of adsorbates through the LOM mechanism, which are of considerable importance for electrochemical performance [73]. However, it is challenging to directly characterize the surface behavior of the catalysts in aqueous condition, necessitating advanced operando/in situ techniques.

Cerium Oxide

Recently, cerium oxide CeO_2 has emerged as a highly promising candidate for OER electrocatalysis [60]. CeO_2 is an abundant rare-earth metal oxide with the fluorite crystal structure, featuring a face-centered cubic (fcc) unit cell with the space group of Fm3m. In the unit cell of CeO_2, each cerium ion is coordinated with eight adjacent oxygen ions, forming an octahedral interstitial structure, while each oxygen ion is coordinated with four adjacent cerium ions, resulting in a tetrahedral unit. The unoccupied 4f orbital and abundant electronic energy levels confer CeO_2 with significant potential for OER catalysis. Both the electronic structure of Ce and previous reports have demonstrated the coexistence of Ce(IV) and Ce(III) and their facile interconversion [74]. The flexible transition between Ce^{4+} and Ce^{3+} oxidation states in CeO_2 are conducive to the generation of oxygen vacancy defects and the reversible surface oxygen ion-storage capacity through the loss of electrons or oxygen. The presence of these oxygen vacancies, coupled with the ability of cerium to toggle between the Ce(III) and Ce(IV) oxidation states, endows CeO_2 with dynamic lattice oxygen chemistry. The multivalence property of Ce within CeO_2 can have a beneficial impact on promoting strong interactions with other components in catalysts, thereby enhancing the electrochemical performance of the catalysts. Furthermore, the robust mechanical stability and corrosion resistance of CeO_2 in alkaline environments renders it suitable for harsh electrocatalytic environments. The prominent redox property, high oxygen storage capacity, abundant oxygen

vacancies, and mechanical stability contribute to the wide application of CeO_2-based materials in various catalytic applications, such as OER, HER, oxygen reduction reaction (ORR), nitrogen reduction reaction (NRR), methanol electrooxidation reaction (MOR), oxygen sensors, fuel cells, photoelectrochemical catalysis, etc. [60] Apart from the above-mentioned properties, CeO_2 has also be known as a solid-state mixed ionic conductor due to its high conductivities of oxygen ion and proton, especially for ultra-high-temperature applications (typically 450-800 °C) such as oxygen sensors and protonic ceramic fuel cell [60].

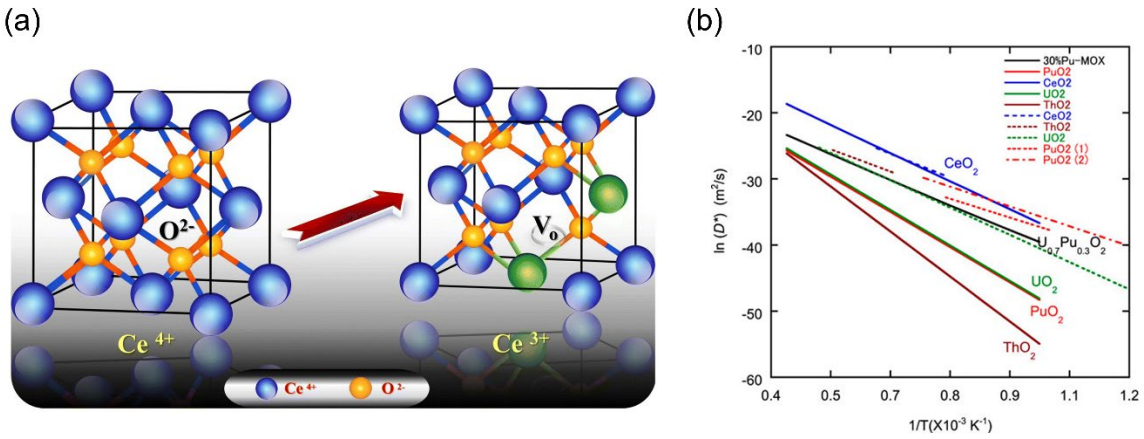

Figure 1.12 The (a) crystal structure and (b) oxygen diffusion coefficient of CeO_2 [75, 76].

These properties make CeO_2 an effective proton carrier, offering new opportunities for the design of advanced functionalities based on these characteristics. Actually, the proton conductivity of hydrated ceria can reach up to 10^{-3} S cm^{-1} at room temperature [77]. Recently, Rupp's group utilized CeO_2 as a proton-conductive electrolyte in glucose fuel cells operating at body temperature to harness energy within the human body, shedding light on the potential application of leveraging its favorable proton conductivity for room temperature applications [78].

1.5.3 Phosphates

Transition-metal phosphates (TMPs) have been extensively employed as efficient OER electrocatalysts due to their structural diversity and catalytic properties [79]. The strong affinity between TM centers and phosphate ligands has prompted the development of various TM phosphate and phosphonate materials. Cobalt-based phosphates, the first phosphate members identified for OER, are regarded as highly active water oxidation catalysts [80]. TMPs comprises the coordination of metal centers with phosphoric acid, which tend to form a 3D layered structure with an open framework, interconnected by MO_x polyhedral and PO_4 tetrahedra via co-prisms or co-vertices. The phosphate groups could serve as proton acceptors to facilitate the oxidation of metal atoms, owing to the capability of protons diffusion through the interlamellar region, while also inducing distorted local metal geometry that promotes water adsorption and oxidation, thus favoring electrolysis [79]. Besides, the electronic structure can be finely adjusted due to the versatile structures and the adaptable compositions of TMPs, offering an ideal approach for developing excellent catalysts for OER. The TMPs system typically exhibits superb chemical stability due to the robust P–O covalent bond. Prior research has demonstrated that both crystallinity and composition significantly influence the OER mechanism and intrinsic activity of TMPs, necessitating adjustments to further enhance catalytic activity [81].

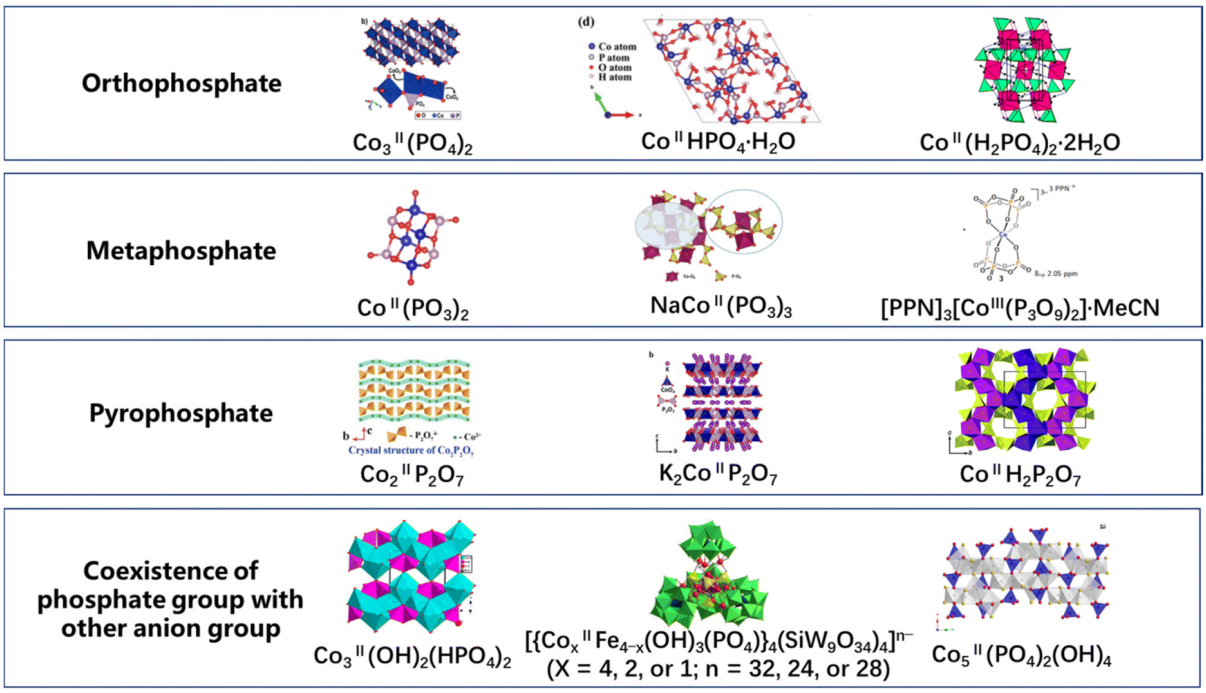

Figure 1.13 Classification of cobalt phosphate-based materials [82].

TMPs can be categorized as orthophosphate, pyrophosphate, and metaphosphate based on the phosphate groups, which are PO_4^{3-}, $(P_2O_7)^{4-}$, and PO_3^-, respectively (**Figure 1.13**) [82]. The transition-metal metaphosphate (TMMP) with the highest P contents, high oxidation state of phosphorus, and strong P-O bonds is an attractive candidate for OER applications [83]. Depending on the cation radius, either cyclic or chain structures are seen in the TMMP family. The propensity of cations like Ca^{2+}, Cd^{2+}, Ba^{2+}, Sr^{2+}, and Mn^{2+} to form chain metaphosphates in the orthorhombic crystal structure increases with their radius. The chain metaphosphate as shown in **Figure 1.14b** consists of linked MO_x octahedra and PO_4 tetrahedra. Each PO_4 tetrahedron shares a corner with two neighboring PO_4 tetrahedra, and each tetrahedron has two terminal oxygen atoms in addition to two shared oxygen atoms. As a result, six additional chains form to encircle the one-dimensional (1D) $(PO_3)^-$ chains that are formed along the a-axis. Cubic structures containing cyclic metaphosphates are preferentially formed for smaller ions (Mg^{2+} and Zn^{2+}), while chain metaphosphates can also be obtained. One way

to conceptualize the atomic arrangement is as a sequence of alternating layers running parallel to the (a, b) plane. The crystal structure of a common cyclotetraphosphate is depicted in **Figures 1.14c, d**. The edge-sharing MO_x octahedra form a 1D zigzag chain, and the layers of MO_x octahedra are nicely separated by PO_4 tetrahedra. In the ac plane, the zigzag chains are connected to one another by PO_4 tetrahedra, forming a two-dimensional (2D) lattice network. Furthermore, dimers are formed by the two distinct metal ions within the unit cell [84].

The first time TMMPs were employed as the electrocatalyst towards OER was in 2012 [85], when Tilley's group synthesized $Co(PO_3)_2$ nanoparticles by annealing the molecular precursor. Although the prepared $Co(PO_3)_2$ nanoparticles loaded on Ni foam showed moderate OER performance in a neutral phosphate-buffer electrolyte, it opens a new way for utilizing TMMPs for electro catalyzing water oxidation. After that, various strategies have been investigated to optimize the OER performance of the TMMPs [86]. Typically, the poor conductivity and local aggregation of single TMMPs significantly impede their large-scale application in water electrolysis. Integrating with conductive substrates to construct a heterostructure could improve overall conductivity of the catalyst, regulate the electronic structures, and modify the active sites, which could enhance the kinetics of OER. Recently, Gong et al. integrated $Fe_{1-x}Ni_x(PO_3)_2$ with Ni_2P, which exhibits good electrical conductivity and electrocatalytic activity, and loaded it onto a Ni foam electrode for freshwater and seawater electrolysis [87]. The heterostructure $Fe_{1-x}Ni_x(PO_3)_2/Ni_2P$/NF exhibiting nanoflower morphology suggested prominent activity and stability in the different electrolyte. It is found that the abundant heterogeneous interfaces within the catalysts could facilitate the electron transfer at the interfaces and the exposure of numerous active sites, thereby improving the OER activity. A harsh electrolysis environment can be accommodated by employing the

synthesis strategy of in situ growth and the creation of heterogeneous interfaces, which can substantially enhance the catalyst's stability and enable highly efficient and stable oxygen evolution in demanding conditions.

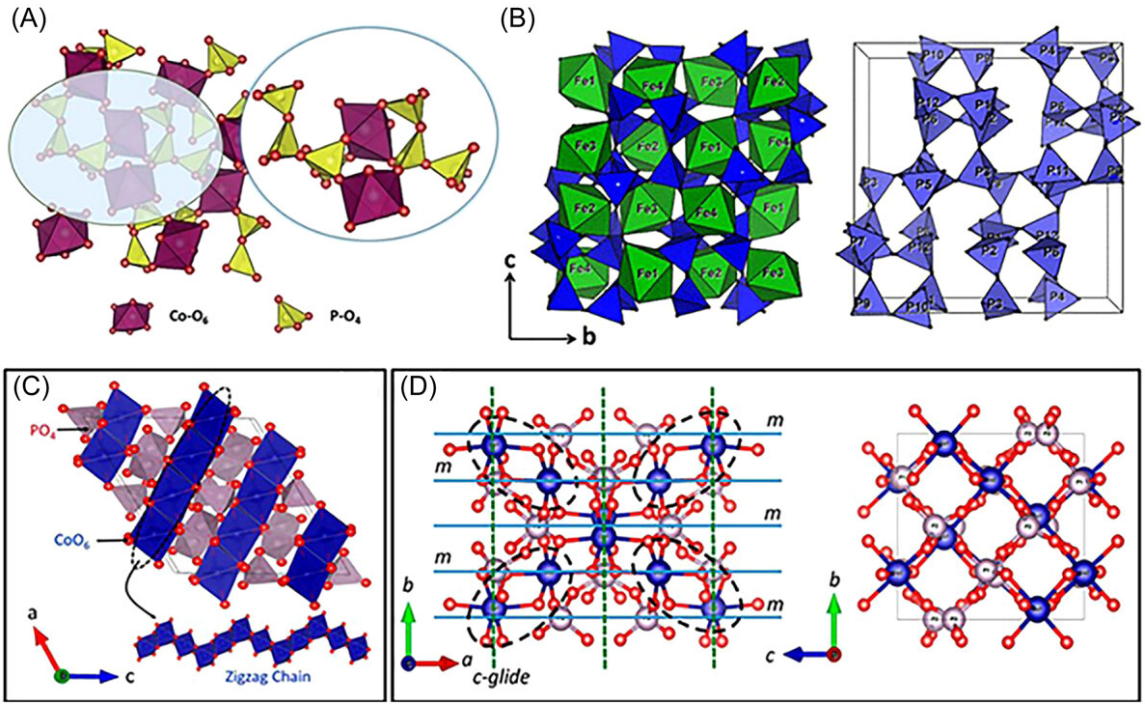

Figure 1.14 (a) The TMPs 3D open-framework structure. The configuration of (c, d) cyclotetraphosphate and (b) chain metaphosphate [84].

Even though a number of TMMPs have been employed as electrocatalysts and exhibit good electrochemical activity, figuring out the structure–activity relationship is still difficult. For instance, electrocatalytic activity and stability are influenced by the bond length of M–O in various configurations, the local environment, geometry, and degree of distortion of the metal atoms, and the interaction between the TM and PO_3. Therefore, the development of new, effective electrocatalysts would benefit from the controlled synthesis, characterization, and investigation of TMMPs with various microstructures and how their structure affects OER performance. Furthermore, the insufficient electrical conductivity and tendency of metal phosphates to agglomerate prevent further improvement of their catalytic efficiency.

Moreover, in comparison to other types of phosphates, there are relatively few studies on the application of TMMPs in the OER, which necessitates further investigations.

1.6 Objectives and Outline of Thesis

1.6.1 Objectives

Hydrogen energy is considered one of the most promising clean alternatives for next-generation fuel consumption. In line with this prospect, the scalable production of hydrogen through the electrocatalysis of water and/or seawater has been the subject of extensive research. The development of efficient OER electrocatalysts, while simultaneously suppressing ClOR process, and gaining a fundamental understanding of the reaction mechanisms are crucial for practical water/seawater electrolysis. Despite considerable efforts invested in the advancement of TM-based OER electrocatalysts for water and seawater electrolysis, their performances have yet to meet industrial standards, and there remain numerous deficiencies in replacing noble metal-based catalysts. Several unanswered questions necessitate investigation, including:

(1) Given that the industrial operation of water electrolysis for hydrogen production typically occurs at temperatures higher than ambient, is there a discernible difference in the physicochemical properties of electrocatalysts under these elevated temperatures? If so, is it necessary to characterize the catalysts at elevated temperatures and the practical working conditions?

(2) Surface reconstruction is a prevalent occurrence in TM-based OER electrocatalysts. In the presence of multiple active TM elements in the OER catalyst, is there any correlation between the different surface-reconstructed species?

(3) What is the underlying mechanism by which electrocatalysts facilitate OER while simultaneously suppressing ClOR formation in the presence of high concentrations of Cl^- in seawater electrolytes for specific catalysts?

1.6.2 Outline

This thesis presents the development of efficient TM-based catalysts towards OER for practical water and seawater electrolysis. The thesis is organized as bellow:

Chapter 1 initially provides a succinct overview of the research background, followed by an introduction of the fundamental principles of water/seawater electrolysis and OER. Subsequently, various efficient, cost-effective, and stable TM-based catalysts for OER are also reviewed.

Chapter 2 outlines the primary experimental methodologies utilized in this thesis, encompassing the chemical compounds and reagents, material preparation techniques, and various ex-situ and in-situ characterization methods. Additionally, it also includes the assembly and testing of the AEMWE single cells.

Chapter 3 describes a series of CeO_2/NiFe-based LDH materials with high oxygen ion diffusion rate and high concentration of oxygen vacancies to optimize the OER activity and effectively prevent the adsorption and oxidation of Cl^- under alkaline and seawater electrolytes. The emerged CeO_2 partially covering the surfaces of LDH also inhibits the direct adsorption of Cl^-, while the high proton conductivity could help prevent the accumulation of protons within the LDH interlayers, thereby averting structural collapse and achieving superior stability. Notably, the enhanced mixed ionic conductivities at elevated temperature contribute to significant improvements in OER performance, which highlights the importance

of characterizing the OER process under high temperature conditions for serving practical applications.

Chapter 4 introduces a double perovskite $NdBa_{0.75}Ca_{0.25}Co_{1.5}Fe_{0.4}Ni_{0.1}O_{5+\delta}$ (donated as NBCCFN) synthesized by electrospinning method. A series of ex-situ and in-situ characterizations indicate that the in-situ formation of NiOOH species through a surface reconstruction process serves as the actual active sites for OER. Additionally, NiOOH can trigger the formation of FeOOH species, which synergistically facilitates the OER formation, as evidenced by the inconspicuous signal of FeOOH in the sample without Ni incorporation. The NBCCFN specimen shows remarkable activity, selectivity, and durability towards water and seawater electrolysis. Even when fed with natural seawater, the NBFFCN-based electrolyser could maintain stable operation, underscoring its significant potential for practical application in water/seawater electrolysis.

Chapter 5 presents a relatively underexplored cobalt metaphosphate ($K_2Co(PO_3)_4$) material, of which the in-situ formed CoOOH through complete self-reconstruction process acting as the real active sites for OER. The completely reconstructed catalyst demonstrates superior activity. In addition, the advantageous adsorption of OH^- over Cl^- for the prepared catalyst ensures the high selectivity of the catalyst in seawater electrolysis, as indicated by the theoretical and experimental results. The durability of the catalyst has been proved for both three-electrode system and membrane-based water electrolyser in both alkaline condition and seawater electrolysis.

Chapter 6 is the last chapter of the thesis, offering a comprehensive summary of the investigations on TM-based catalysts for water/seawater splitting, thereby enhancing the understanding of the improved activity, selectivity, and stability towards OER. Additionally,

it provides insights into the future research directions for OER and water/seawater electrolysis.

1.7 References

1. T. da Silva Veras, T. S. Mozer and A. da Silva César, *International journal of hydrogen energy*, 2017, **42**, 2018-2033.
2. M. Younas, S. Shafique, A. Hafeez, F. Javed and F. Rehman, *Fuel*, 2022, **316**, 123317.
3. N. Hassan, A. Jalil, S. Rajendran, N. Khusnun, M. Bahari, A. Johari, M. Kamaruddin and M. Ismail, *International Journal of Hydrogen Energy*, 2023.
4. S. S. Kumar and H. Lim, *Energy reports*, 2022, **8**, 13793-13813.
5. Y. Zhu, Q. Lin, Y. Zhong, H. A. Tahini, Z. Shao and H. Wang, *Energy & Environmental Science*, 2020, **13**, 3361-3392.
6. J. Corbin, M. Jones, C. Lyu, A. Loh, Z. Zhang, Y. Zhu and X. Li, *RSC advances*, 2024, **14**, 6416-6442.
7. M. Chatenet, B. G. Pollet, D. R. Dekel, F. Dionigi, J. Deseure, P. Millet, R. D. Braatz, M. Z. Bazant, M. Eikerling and I. Staffell, *Chemical society reviews*, 2022, **51**, 4583-4762.
8. M. Faraday, *Experimental researches in electricity*, Richard and John Eward Taylor, London, 2nd edn., 1849.
9. D. M. Santos, C. A. Sequeira and J. L. Figueiredo, *Química Nova*, 2013, **36**, 1176-1193.
10. M. Paidar, V. Fateev and K. Bouzek, *Electrochimica acta*, 2016, **209**, 737-756.
11. S. De, J. Zhang, R. Luque and N. Yan, *Energy & Environmental Science*, 2016, **9**, 3314-3347.

12. Z. Y. Yu, Y. Duan, X. Y. Feng, X. Yu, M. R. Gao and S. H. Yu, *Advanced Materials*, 2021, **33**, 2007100.

13. F.-Y. Chen, Z.-Y. Wu, Z. Adler and H. Wang, *Joule*, 2021, **5**, 1704-1731.

14. Y. Sun, T. Zhang, C. Li, K. Xu and Y. Li, *Journal of materials chemistry A*, 2020, **8**, 13415-13436.

15. H. Kojima, K. Nagasawa, N. Todoroki, Y. Ito, T. Matsui and R. Nakajima, *International Journal of Hydrogen Energy*, 2023, **48**, 4572-4593.

16. G. A. Lindquist, Q. Xu, S. Z. Oener and S. W. Boettcher, *Joule*, 2020, **4**, 2549-2561.

17. S. r. Dresp, F. Dionigi, M. Klingenhof and P. Strasser, *ACS Energy Letters*, 2019, **4**, 933-942.

18. R. K. Karlsson and A. Cornell, *Chemical reviews*, 2016, **116**, 2982-3028.

19. F. Dionigi, T. Reier, Z. Pawolek, M. Gliech and P. Strasser, *ChemSusChem*, 2016, **9**, 962-972.

20. R.-T. Liu, Z.-L. Xu, F.-M. Li, F.-Y. Chen, J.-Y. Yu, Y. Yan, Y. Chen and B. Y. Xia, *Chemical Society Reviews*, 2023.

21. D. Jang, H.-S. Cho and S. Kang, *Applied energy*, 2021, **287**, 116554.

22. C. Daoudi and T. Bounahmidi, *International Journal of Hydrogen Energy*, 2023.

23. I. Jang, J. SA Carneiro, J. O. Crawford, Y. J. Cho, S. Parvin, D. A. Gonzalez-Casamachin, J. Baltrusaitis, R. P. Lively and E. Nikolla, *Chemical Reviews*, 2024.

24. M. A. Khan, H. Zhao, W. Zou, Z. Chen, W. Cao, J. Fang, J. Xu, L. Zhang and J. Zhang, *Electrochemical Energy Reviews*, 2018, **1**, 483-530.

25. L. Lei, J. Zhang, Z. Yuan, J. Liu, M. Ni and F. Chen, *Advanced Functional Materials*, 2019, **29**, 1903805.

26. Z. Liu, B. Han, Z. Lu, W. Guan, Y. Li, C. Song, L. Chen and S. C. Singhal, *Applied Energy*, 2021, **300**, 117439.

27. M. A. Hickner, H. Ghassemi, Y. S. Kim, B. R. Einsla and J. E. McGrath, *Chemical reviews*, 2004, **104**, 4587-4612.

28. S. A. Lee, J. Kim, K. C. Kwon, S. H. Park and H. W. Jang, *Carbon Neutralization*, 2022, **1**, 26-48.

29. D. Xu, M. B. Stevens, M. R. Cosby, S. Z. Oener, A. M. Smith, L. J. Enman, K. E. Ayers, C. B. Capuano, J. N. Renner and N. Danilovic, *ACS catalysis*, 2018, **9**, 7-15.

30. N. Du, C. Roy, R. Peach, M. Turnbull, S. Thiele and C. Bock, *Chemical reviews*, 2022, **122**, 11830-11895.

31. D. Hua, J. Huang, E. Fabbri, M. Rafique and B. Song, *ChemElectroChem*, 2023, **10**, e202200999.

32. D. Li, A. R. Motz, C. Bae, C. Fujimoto, G. Yang, F.-Y. Zhang, K. E. Ayers and Y. S. Kim, *Energy & Environmental Science*, 2021, **14**, 3393-3419.

33. E. J. Park, C. G. Arges, H. Xu and Y. S. Kim, *ACS Energy Letters*, 2022, **7**, 3447-3457.

34. S. Z. Oener, M. J. Foster and S. W. Boettcher, *Science*, 2020, **369**, 1099-1103.

35. D. H. Marin, J. T. Perryman, M. A. Hubert, G. A. Lindquist, L. Chen, A. M. Aleman, G. A. Kamat, V. A. Niemann, M. B. Stevens and Y. N. Regmi, *Joule*, 2023, **7**, 765-781.

36. N. Zhang and Y. Chai, *Energy & Environmental Science*, 2021, **14**, 4647-4671.

37. X. Wang, H. Zhong, S. Xi, W. S. V. Lee and J. Xue, *Advanced Materials*, 2022, **34**, 2107956.

38. L. Giordano, B. Han, M. Risch, W. T. Hong, R. R. Rao, K. A. Stoerzinger and Y. Shao-Horn, *Catalysis Today*, 2016, **262**, 2-10.

39. A. Grimaud, O. Diaz-Morales, B. Han, W. T. Hong, Y.-L. Lee, L. Giordano, K. A. Stoerzinger, M. T. Koper and Y. Shao-Horn, *Nature chemistry*, 2017, **9**, 457-465.

40. J. S. Yoo, X. Rong, Y. Liu and A. M. Kolpak, *ACS Catalysis*, 2018, **8**, 4628-4636.

41. H. Du, H. Luo, M. Jiang, X. Yan, F. Jiang and H. Chen, *Applied Catalysis A: General*, 2023, 119348.

42. M. Lu, Y. Zheng, Y. Hu, B. Huang, D. Ji, M. Sun, J. Li, Y. Peng, R. Si and P. Xi, *Science advances*, 2022, **8**, eabq3563.

43. A. Zou, Y. Tang, C. Wu, J. Li, H. Meng, Z. Wang, Y. Ma, H. An, H. Zhong and Q. Zhang, *ChemSusChem*, 2024, **17**, e202301195.

44. B. Wang and F. Zhang, *Angewandte Chemie International Edition*, 2022, **61**, e202111026.

45. J. Suntivich, K. J. May, H. A. Gasteiger, J. B. Goodenough and Y. Shao-Horn, *Science*, 2011, **334**, 1383-1385.

46. J.-W. Zhao, Z.-X. Shi, C.-F. Li, Q. Ren and G.-R. Li, *ACS materials letters*, 2021, **3**, 721-737.

47. K. Zhang and R. Zou, *Small*, 2021, **17**, 2100129.

48. Z. P. Wu, X. F. Lu, S. Q. Zang and X. W. Lou, *Advanced Functional Materials*, 2020, **30**, 1910274.

49. S. Trasatti, *Journal of electroanalytical chemistry (1992)*, 1999, **476**, 90-91.

50. W. Zheng, L. Y. S. Lee and K.-Y. Wong, *Nanoscale*, 2021, **13**, 15177-15187.

51. W. He, X. Li, C. Tang, S. Zhou, X. Lu, W. Li, X. Li, X. Zeng, P. Dong and Y. Zhang, *Acs Nano*, 2023, **17**, 22227-22239.

52. S. Bolar, S. Shit, N. C. Murmu and T. Kuila, *Sustainable Energy & Fuels*, 2021, **5**, 5915-5945.

53. Y. Li, Y. Sun, Y. Qin, W. Zhang, L. Wang, M. Luo, H. Yang and S. Guo, *Advanced Energy Materials*, 2020, **10**, 1903120.

54. J. Wang, F. Xu, H. Jin, Y. Chen and Y. Wang, *Advanced materials*, 2017, **29**, 1605838.

55. T. Li, H. N. Miras and Y.-F. Song, *Catalysts*, 2017, **7**, 260.

56. J. Yu, F. Yu, M.-F. Yuen and C. Wang, *Journal of Materials Chemistry A*, 2021, **9**, 9389-9430.

57. H. You, D. Wu, D. Si, M. Cao, F. Sun, H. Zhang, H. Wang, T.-F. Liu and R. Cao, *Journal of the American Chemical Society*, 2022, **144**, 9254-9263.

58. L. Tan, J. Yu, C. Wang, H. Wang, X. Liu, H. Gao, L. Xin, D. Liu, W. Hou and T. Zhan, *Advanced Functional Materials*, 2022, **32**, 2200951.

59. Q. Li, L. Song, Z. Liang, M. Sun, T. Wu, B. Huang, F. Luo, Y. Du and C.-H. Yan, *Advanced Energy and Sustainability Research*, 2021, **2**, 2000063.

60. J. Wang, X. Xiao, Y. Liu, K. Pan, H. Pang and S. Wei, *Journal of Materials Chemistry A*, 2019, **7**, 17675-17702.

61. Q. Dong, C. Shuai, Z. Mo, N. Liu, G. Liu, J. Wang, H. Pei, Q. Jia, W. Liu and X. Guo, *Journal of Solid State Chemistry*, 2021, **296**, 121967.

62. J. Xia, H. Zhao, B. Huang, L. Xu, M. Luo, J. Wang, F. Luo, Y. Du and C. H. Yan, *Advanced Functional Materials*, 2020, **30**, 1908367.

63. X. Rong, J. Parolin and A. M. Kolpak, *ACS catalysis*, 2016, **6**, 1153-1158.

64. Sonia, H. Kumari, Suman, S. Chahal, S. Devi, S. Kumar, S. Kumar, P. Kumar and A. Kumar, *Applied Physics A*, 2023, **129**, 91.

65. V. Zhandun, *Journal of Magnetism and Magnetic Materials*, 2021, **533**, 168015.

66. L. Han, S. Dong and E. Wang, *Advanced materials*, 2016, **28**, 9266-9291.

67. L.-B. Liu, C. Yi, H.-C. Mi, S. L. Zhang, X.-Z. Fu, J.-L. Luo and S. Liu, *Electrochemical Energy Reviews*, 2024, **7**, 14.

68. L. Zhu, R. Ran, M. Tade, W. Wang and Z. Shao, *Asia-Pacific Journal of Chemical Engineering*, 2016, **11**, 338-369.

69. Y. Li, W. Zhang, Y. Zheng, J. Chen, B. Yu, Y. Chen and M. Liu, *Chemical Society Reviews*, 2017, **46**, 6345-6378.

70. Y. Liu, Z. Wang, J. P. M. Veder, Z. Xu, Y. Zhong, W. Zhou, M. O. Tade, S. Wang and Z. Shao, *Advanced Energy Materials*, 2018, **8**, 1702604.

71. A. Banerjee, M. K. Awasthi, P. Maji, M. Pal, S. T. Aziz, G. K. Lahiri and A. Dutta, *ChemElectroChem*, 2023, **10**, e202201098.

72. T. Rom, Poojita and A. K. Paul, *ChemCatChem*, 2023, **15**, e202300774.

73. L. Gao, X. Cui, C. D. Sewell, J. Li and Z. Lin, *Chemical Society Reviews*, 2021, **50**, 8428-8469.

74. J. Yu, X. Du, H. Liu, C. Qiu, R. Yu, S. Li, J. Ren and S. Yang, *Energy & Fuels*, 2021, **35**, 19000-19011.

75. A. A. Badawy, M. H. A. Rehim and G. M. Turky, *RSC advances*, 2023, **13**, 8955-8966.

76. M. Kato, M. Watanabe, S. Hirooka and R. Vauchy, *Frontiers in Nuclear Engineering*, 2023, **1**, 1081473.

77. P. Simons, K. P. Torres and J. L. Rupp, *Advanced Functional Materials*, 2021, **31**, 2009630.

78. P. Simons, S. A. Schenk, M. A. Gysel, L. F. Olbrich and J. L. Rupp, *Advanced Materials*, 2022, **34**, 2109075.

79. H. Zhao and Z.-Y. Yuan, *ChemCatChem*, 2020, **12**, 3797-3810.

80. H. Wan, R. Ma, X. Liu, J. Pan, H. Wang, S. Liang, G. Qiu and T. Sasaki, *ACS Energy Letters*, 2018, **3**, 1254-1260.

81. Y. Li, Z. Dong and L. Jiao, *Advanced Energy Materials*, 2020, **10**, 1902104.

82. X. Zhang, Q. Hou, S. Cao, X. Lin, X. Chen, Z. Wang, S. Wei, S. Liu, F. Dai and X. Lu, *Green Chemistry*, 2023, **25**, 7883-7903.

83. R. Guo, X. Lai, J. Huang, X. Du, Y. Yan, Y. Sun, G. Zou and J. Xiong, *ChemElectroChem*, 2018, **5**, 3822-3834.

84. Y. Zhang, J. Wu, B. Guo, H. Huo, S. Niu, S. Li and P. Xu, *Carbon Energy*, 2023, **5**, e375.

85. H. S. Ahn and T. D. Tilley, *Advanced Functional Materials*, 2013, **23**, 227-233.

86. J. Huang, Y. Sun, Y. Zhang, G. Zou, C. Yan, S. Cong, T. Lei, X. Dai, J. Guo, R. Lu, Y. Li and J. Xiong, *Advanced Materials*, 2018, **30**, 1705045.

87. Z.-J. Gong, Z.-C. Hu, Z.-J. Bai, X.-A. Yu, Z. Liu and Y.-Q. Wang, *Inorganic Chemistry*, 2023, **62**, 13338-13347.

Chapter 2 Materials and Characterization Methods

2.1 Chemicals and Reagents

Table 2.1 List of chemicals and reagents.

Reagent	Specification	Manufacturer
$Ni(NO_3)_2 \cdot 6H_2O$	Analytical reagent	Aladdin Chemical Reagent Co., Ltd
$Fe(NO_3)_3 \cdot 9H_2O$	Analytical reagent	Aladdin Chemical Reagent Co., Ltd
$Ce(NO_3)_3 \cdot 6H_2O$	Analytical reagent	Aladdin Chemical Reagent Co., Ltd
$Nd(NO_3)_3 \cdot 6H_2O$	Analytical reagent	Aladdin Chemical Reagent Co., Ltd
$Co(NO_3)_3 \cdot 6H_2O$	Analytical reagent	Sinopharm Chemical Reagent Co., Ltd
$Ba(NO_3)_2$	Analytical reagent	Aladdin Chemical Reagent Co., Ltd
$Ca(NO_3)_2$	Analytical reagent	Aladdin Chemical Reagent Co., Ltd
KNO_3	Analytical reagent	Aladdin Chemical Reagent Co., Ltd
$NH_4H_2PO_4$	Analytical reagent	Aladdin Chemical Reagent Co., Ltd
NaCl	Analytical reagent	Aladdin Chemical Reagent Co., Ltd
KOH	Analytical/Guarantee reagent	Aladdin Chemical Reagent Co., Ltd
KCl	Analytical reagent	Aladdin Chemical Reagent Co., Ltd

$NH_4H_2PO_4$	Analytical reagent	Aladdin Chemical Reagent Co., Ltd
Ascorbic acid	Analytical reagent	Aladdin Chemical Reagent Co., Ltd
Urea	Analytical reagent	Aladdin Chemical Reagent Co., Ltd
Dimethylformamide	Analytical reagent	Sinopharm Chemical Reagent Co., Ltd
Polyacrylonitrile	Analytical reagent Mw = 250,000	Aladdin Chemical Reagent Co., Ltd
Ethanol	Analytical reagent	Sinopharm Chemical Reagent Co., Ltd
Nafion	5 wt.%	DuPont Co.
Deionized water	18 MΩ·cm	Self-manufactured

2.2 Synthesis Methods of Electrocatalysts

2.2.1 Electrodeposition Method

The LDH based materials were synthesized by electrodeposition method at room temperature. The deposition solutions were prepared by dissolving 2 mol of $Ni(NO_3)_2 \cdot 6H_2O$, (1-x) mol of $Fe(NO_3)_3 \cdot 9H_2O$, and x (x = 0, 0.1, 0.3, 0.5, 0.7, and 0.9, corresponding to the samples named NiFe LDH, NFCe0.1, NFCe0.3, NFCe0.5, NFCe0.7, and NFCe0.9) mol of $Ce(NO_3)_3 \cdot 6H_2O$ into 50 mL ultra-pure water via continuous magnetic stirring, maintaining a molar ratio of Ni^{2+} to (Fe^{3+} + Ce^{3+}) at 2:1. $Ce(NO_3)_3 \cdot 6H_2O$ would not be added for synthesizing NiFe LDH sample. Electrodeposition process was carried out by a three-electrode configuration cell, using Cu plate (for collecting powder samples) or nickel foam (for self-supporting electrode preparation) as working electrode, Ag/AgCl (saturated KCl) electrode as reference electrode,

and platinum plate as counter electrode. A constant potential of -1 V vs. Ag/AgCl (saturated KCl) was exerted for 10 minutes to form the catalyst materials. After deposition, the specimens were carefully exfoliated from the Cu plate and thoroughly washed with ultra-pure water multiple times, followed by centrifugation. Subsequently, the catalysts were subjected to vacuum drying at 60 °C overnight.

2.2.2 Electrospinning Method

The perovskite nanofibers were synthesized through the electrospinning method. The typical preparation process was that, $Nd(NO_3)_3 \cdot 6H_2O$ (3.125 mmol), $Ba(NO_3)_2$ (2.344 mmol), $Ca(NO_3)_2$ (0.781 mmol), $Co(NO_3)_3 \cdot 6H_2O$ (4.688 mmol), $Fe(NO_3)_3 \cdot 9H_2O$ (1.25 mmol), and $Ni(NO_3)_2 \cdot 6H_2O$ (0.156 mmol) were added in 41.25 mL of N, N-Dimethylformamide (DMF, anhydrous ≥99%) and vigorously stirred at 60 ℃ until dissolved. Then, 4.41 g of high purity polyacrylonitrile (PAN) (Mw = 250,000, 12 wt.% based on the mass of dimethyl formamide (DMF)) was added to the solution and constantly stirred for at least 10 h to form a uniform precursor solution. A plastic syringe with a 21-hauge needle was used to load the electrospinning solution, followed by installation on a syringe pump. The collector was a rotating drum with aluminum foil covered, keeping 20 cm from the needle tip. The voltages applied in needle tip and the collector were 18 kV and -2 kV, respectively. The collected samples were then subjected to oven and dried at 60 ℃ overnight. After drying, the as-spun samples were calcined at 950 ℃ for 5 h with an air furnace, which were then collected for catalysis after grinding.

2.2.3 Solution Combustion Method

The transition metal metaphosphate $K_2Co(PO_3)_4$ was synthesized through solution combustion method, as per a previous report [1]. In summary, 2 mmol of KNO_3, 1 mmol of

$Co(NO_3)_3 \cdot 6H_2O$, 4 mmol of $NH_4H_2PO_4$, and 1 mmol of urea (serving as fuel) were dissolved into 15 mL of ultrapure water and vigorously stirred for at least 1 h. Subsequently, the homogeneous solution was freeze-dried to remove excess water. The precursor was then heated at 350 ℃ for 3 h to initiate the exothermic combustion reaction. The resulting powder was ground and subjected to calcination at 700 ℃ for 12 h in a tube furnace under the N_2 gas, yielding the required catalysts. The reaction process can be described as the following equation:

$$2KNO_3 + Co(NO_3)_3 \cdot 6H_2O + 4NH_4H_2PO_4 + CH_4N_2O \rightarrow K_2Co(PO_3)_4/C + 16H_2O + 5NO_x + 4NH_3 + 6CO_x \quad (2.1)$$

2.3 Characterization Methods

2.3.1 Material Characterizations

The crystallinity and phase structure of the samples were characterized by powder X-ray diffraction (XRD) on Rigaku Smartlab X-ray diffractometer, employing Cu Kα radiation (λ = 1.5418 Å) at 45 kV and 200 mA. The step size is 0.02°, while a scan rate of 8° min^{-1}. The Rietveld refinements of the XRD patterns were conducted utilizing the General Structure Analysis System (GSAS) software with the EXPGUI interface [2]. The surface morphology and microstructure of the electrocatalyst samples were recorded by field emission scanning electron microscope (FESEM) equipped with energy-dispersive X-ray (EDX) spectroscopy module using Tescan MIRA microscope. The chamber pressure maintained below 1.0×10^{-5} torr during operation. The EDX spectra were obtained to detect the elemental compositions and distributions of the samples. Field emission transmission electron microscope (FETEM), high-resolution transmission electron microscope (HRTEM), and EDX analyses were conducted using a JEOL JEM-2100F operated at 200 kV to detect the detailed phase structure

of the samples. The catalyst samples were dispersed in absolute ethyl alcohol and ultrasonicated for at least 30 min to obtain homogeneous ink, followed by dropping on the carbon-coated copper grid. The surface elemental composition and chemical information of the catalysts were analyzed by X-Ray photoelectron spectroscopy (XPS) using Thermo Fisher Scientific Nexsa and Thermo Scientific K-Alpha with monochromatic and focused 12 kV Al Kα X-ray. The C 1s with a binding energy of 284.8 eV served as the reference value to compensate for the charging of the sample. The XPS data were fitted by Avantage software. Attenuated total reflection Fourier transform infrared spectrometer (FT-IR) spectra were acquired by PerkinElmer Spectrum Two and Bruker Vertex-70 instruments to identify the vibrational frequencies of the as-prepared electrocatalysts. The Brunauer-Emmett-Teller (BET) specific surface areas were detected by nitrogen adsorption-desorption testing using MicromeriticsASAP. The metal element compositions of the synthesized electrocatalysts were determined by inductively coupled plasma-mass spectrometry (ICP-MS) (Agilent Technologies 7900) and inductively coupled plasma-optical emission spectrometer (ICP-OES) (Agilent720ES). Ultraviolet-visible spectra (UV-vis) were conducted on Shimadzu UV-2550 to measure the chlorine species in the electrolytes. The Raman spectra were obtained by WITec Alpha 300R, with a 633 nm laser source. A silicon wafer (520.7 cm^{-1}) was employed for the calibration of Raman spectrometer. Hard X-ray absorption spectroscopy (XAS) include Co K-edge X-ray absorption near edge structure (XANES) and extended X-ray absorption fine structure (EXAFS) spectra were measured on the 1.9T wiggler XAS Beamline at the Australian Synchrotron in Melbourne in fluorescence mode, using liquid nitrogen cooled Si (111) monochromator crystal. The energy was calibrated using Co foil. The electron paramagnetic resonance (EPR) spectra were recorded using Bruker EMXplus-6/1 instrument.

2.3.2 In-Situ Characterizations

In-situ Raman spectroscopy was conducted using a custom-made three-electrode cell, with a 5 mm gold disk working electrode, a Hg/HgO (1 M KOH) reference electrode, and a Pt wire counter electrode. The electrolyte utilized was a 1 M KOH solution. Other conditions were the same as those used for electrochemical measurements, except for the ink preparation. Owing to the excessive strength of the carbon signals and the comparatively weak signals of the catalysts in the electrolyte, the catalyst ink was prepared without the inclusion of Super P Li carbon powder. The Raman spectra were collected under open circuit potential (OCP) and each applied potential.

The online differential electrochemical mass spectrometry (DEMS) tests were performed using a HIDEN HPR-20 OEMS device. The catalysts were first loaded on carbon clothes as the working electrode, while a Hg/HgO (1 M KOH) electrode and a Pt wire were employed as the reference and counter electrodes, respectively. A 1 M KOH solution containing $H_2{}^{18}O$ was employed as the electrolyte. The CV process was conducted to label the oxygen isotopes, and then the electrocatalyst was rinsed with plentiful deionized $H_2{}^{16}O$ to remove any unbound species. Whereafter, electrochemical tests were carried out in the $H_2{}^{16}O$-based KOH electrolyte. The gas products of different molecular weights were monitored in real-time using online mass spectrometry.

2.4 Electrochemical Measurements

2.4.1 Oxygen Evolution Performance Measurements

The electrochemical OER measurements at room temperature were conducted by a typical three-electrode system using a CHI 660e electrochemical workstation. The glassy carbon

electrode with a diameter of 5 mm, Hg/HgO (1 M KOH), and platinum mesh as working electrode, reference electrode, and counter electrode, respectively. For Hg/HgO (1 M KOH) reference electrode, the potentials were referenced to the RHE by $E_{RHE} = E_{Hg/HgO} + 0.098 + 0.059 \times pH$. It is worth noting that Ag/AgCl (saturated KCl) was selected as the reference electrode for OER measurement at 60 °C, as Hg/HgO cannot work at such a high temperature. The potentials measured with Ag/AgCl (saturated KCl) at 60 °C were referenced to the RHE by $E_{RHE} = E_{Ag/AgCl} + 0.1598 + 0.059 \times pH$. 1 M KOH solution (pH = 14) and simulated seawater (1 M KOH + 0.5 M NaCl) were adopted as aqueous electrolyte medium. The catalysts ink loading on working electrode surface was prepared by adding 10.0 mg of the prepared catalyst, 10.0 mg of the Super P Li carbon powder (conductive agent), and 100 μL of Nafion solution (5 wt%, binder solution) into 1 mL of absolute ethyl alcohol. The mixed solution was then sonicated for at least 1 hour to form a homogeneous catalyst ink. Then, 10 μL of the homogeneous ink was dropped on the surface of the working electrode, followed by naturally drying at room temperature. The mass loading on the working electrode is 0.242 $mg_{(catalyst)}$ cm^{-2}. The electrolyte solutions were saturated with ultra-pure oxygen gas for at least 30 min before electrochemical test and maintained with sufficient input of oxygen during the test. The cyclic voltammogram (CV) curves were performed within the range of OER anodic voltages at different scan rates. Linear sweep voltammetry (LSV) curves were collected at the scan rate of 5 mV s^{-1} from 1.2 to 2.0 V vs. RHE without additional iR compensation. After calibrating to RHE potential, the overpotential (η) can be calculated based on the formula of $\eta\ (V) = E_{RHE} - 1.23$. The electrochemical double layer capacitance (C_{dl}) was obtained by CV test at different scanning rates (which were 20, 40, 60, 80, and 100 mV s^{-1}) in a narrow potential range from 1.17 to 1.27 V vs. RHE. The C_{dl} values can be obtained from the slope of the current density against scan rate. A series of KOH electrolyte solutions with a pH of 12.5, 13, 13.5, and 14 saturated with O_2 were prepared for pH-

dependent activity tests. Rotating-ring-disk-electrode (RRDE) voltammograms conducted in simulated seawater were utilized to separately estimate OER and ClOR currents. Electrochemical impedance spectroscopy (EIS) was conducted at a specified potential within a frequency range of 100 kHz to 0.01 Hz, utilizing an amplitude of 10 mV.

2.4.2 Diffusion Coefficients Measurements of Oxygen Ions and Protons

The oxygen ion diffusion coefficient (D_O) measurements were conducted in N_2-saturated 6 M KOH electrolyte solution using the same three-electrode system as OER tests. CV measurements were first applied with a scan rate of 20 mV s^{-1} under the stationary state of the system. Chronoamperometry (CA) was then performed at a potential that was 50 mV more positive than $E_{1/2}$ (defined as potential halfway between the redox peak currents obtained from CV tests). Proper rotating speed was imposed to eliminate the effect of any electrolyte-based mass transfer. The oxygen ion diffusion coefficient (D_O) was calculated based on the equation $\lambda = a(D_O t)^{-1/2}$, in which λ is a dimensionless shape factor, a is the catalyst particle radius, D_O is the oxygen diffusion coefficient, and t is the time. In our work, λ was identified to be 2. The value a was calculated according to $S=3/(a\rho)$ equation, where S represents specific surface area measured from the BET method, and ρ is the theoretical density determined by Rietveld analysis.

The proton diffusion coefficients (D_P) were determined by the CV test at different scanning rates (2, 5, 10, 20, 50, 100, and 200 mV s^{-1}) based on Randles-Sevcik equation: $I_P = 0.4463n^{3/2}F^{3/2}S(RT)^{-1/2}D_P^{1/2}c^0v^{1/2}$, where I_P is the peak current, n is the electron number involved in the reaction, F is Faraday's constant, S is the working electrode area, R is the ideal gas constant, T is the temperature, D_P is the proton diffusion coefficient, v is the scanning rate, and c^0 is the initial reactant concentration [3].

2.4.3 AEMWE Assembly and Measurement

For assembling AEMWE, the anode was prepared by growing the developed catalysts on washed nickel foam for 10 min, while the cathode was prepared by spraying commercial 20 wt.% Pt/C onto the carbon paper. The cathode ink was prepared by adding 5 mg Pt/C and 100 μL Nafion solution into 1 ml absolute ethyl alcohol, which was then sonicated until a uniform ink was formed. The catalyst mass loading of both anode and cathode was 3 mg cm^{-2}. For comparison, an AEMWE with the RuO_2 anode and Pt/C cathode was also assembled. A commercial anion exchange membrane was sandwiched between the anode and cathode. 1 M KOH solution served as the electrolyte, with a flow rate of 30 mL min^{-1}. Electrochemical analyses of the assembled AEMWE single cells were conducted using a CHI760e electrochemical workstation equipped with a current amplifier. The polarization curves of the AEMWE single cells were obtained by measuring the cell voltage from 1 V_{cell} to 2 V_{cell} at a scan rate of 5 mV s^{-1}, conducted at both room temperature and 60 °C. The stability tests were conducted at a constant current density of 0.5 A cm^{-2}.

2.5 DFT Calculation

DFT calculations were conducted through the Vienna Ab-initio Simulation Package (VASP) under the projector augmented wave (PAW) framework, based on the Perdew–Burke–Ernzerhof (PBE) exchange and correlation functional [4, 5]. The plane-wave basis set had an energy cutoff of 500 eV, in consideration of magnetism and dipole correction. For the sake of electrical structure calculation and geometry optimization, a 4 × 4 × 4 mesh grid size was used.

2.6 References

1. C. Murugesan, S. P. Panjalingam, S. Lochab, R. K. Rai, X. Zhao, D. Singh, R. Ahuja and P. Barpanda, *Nano Energy*, 2021, **89**, 106485.
2. B. H. Toby, *Journal of applied crystallography*, 2001, **34**, 210-213.
3. R. Wang, J. Lang, Y. Liu, Z. Lin and X. Yan, *NPG Asia Materials*, 2015, **7**, e183-e183.
4. G. Kresse and J. Furthmüller, *Computational materials science*, 1996, **6**, 15-50.
5. G. Kresse and J. Furthmuller, *PHYSICAL REVIEW B*, 1996, **54**, 11169-11186.

Chapter 3 NiFe based LDH/CeO_2 Composite with Improved Mixed Ionic Conductivities at Practical Working Temperature for OER

3.1 Introduction

The electrolysis of water and seawater utilizing renewable energy sources to produce green hydrogen holds great promise for attaining future carbon neutrality [1, 2]. However, the sluggish kinetics of the anodic oxygen evolution reaction (OER) pose a significant impediment to achieving desirable energy efficiency [3, 4]. OER is an energy-uphill four-electron-transfer process with a high thermodynamic potential, which necessitates substantial overpotential to drive the reaction, thus exerting a dominant influence on the overall efficiency of the system [5-7]. For seawater electrolysis, specifically, the intricate composition of seawater, encompassing heteroions, microorganisms, and insoluble precipitates, would introduce additional challenges [8]. One notable concern is the electro-oxidation reaction of chlorine (ClOR) and its competition with anodic OER [9, 10]. ClOR is a two-electron-transfer process, which renders it kinetically more favorable than the four-electron-transfer OER [11]. However, OER is more thermodynamically favorable than ClOR, particularly under high pH conditions, leading to a thermodynamic standard potential difference of approximately 480 mV lower than ClOR [12]. To enhance OER kinetics and suppress ClOR for water/seawater electrolysis, developing highly efficient and selective electrocatalysts suitable for alkaline conditions emerges as one of the most viable solutions [13, 14]. The past decades have witnessed the blooming development of the anodic electrocatalysts for water and seawater electrolysis.

NiFe layered double hydroxides (NiFe LDHs) have been extensively recognized as among the most promising electrocatalysts for OER due to their distinctive two-dimensional layered structure, tunable interlayer anions, superior catalytic performance, and low cost, positioning them as viable alternatives to benchmark noble metal catalyst [15, 16]. Nevertheless, their advancement has been significantly hindered by concerns regarding their inadequate stability. Intriguingly, recent studies have found that the proper engineering of NiFe LDH, such as hetero ion substitution, selected anion intercalation, and composite formations, can effectively improve its stability in water and seawater electrolysis [17-21]. Different from laboratory-scale investigations, the industrial operation of water electrolysis typically operates at temperatures ranging from 50 to 80 ℃ [22]. Elevated temperature typically enhances catalytic activity of the electrocatalysts through facilitating ion exchange and electron transfer processes [23]. However, it is often overlooked that the properties of the catalysts at elevated temperatures may differ significantly. Understanding these temperature-dependent properties is crucial for optimizing electrocatalyst performance and promoting their utilization and expansion in industrial settings. For instance, the ionic conductivities of CeO_2 exhibits a strong correlation with temperature, with both oxygen ion and proton conductivities improving as the temperature increases [24]. The increased oxygen ion conductivity at elevated temperature can facilitate oxygen ion transportation, thereby further accelerating reaction kinetics of OER. Previous studies mainly employ CeO_2 as functional support/compound of the electrocatalysts for water electrolysis as itself is electrocatalytically inert. For instance, a prior study has demonstrated that the combination of NiFe LDH with CeO_x could lead to an augmentation of oxygen vacancies at the interfaces, which could facilitate electron/ion migration and charge transfer, and provide additional active sites for catalysis, thus leading to improved OER activities and stability [25]. However, the effect of increased oxygen ionic conductivity of CeO_2 at elevated temperatures (50-80 ℃) has rarely

been investigated and exploited in water electrolysis. In addition, a recent study has revealed that CeO_2 can function as a proton conducting electrolyte for ambient-temperature glucose fuel cells [26]. This discovery has prompted investigations into the proton conductivity of CeO_2 and CeO_2-based materials on OER performance in water electrolysis. Given these considerations, the mixed ionic conductivities of CeO_2 at elevated temperature (i.e., the practical working temperature) and their impact on OER performance warrant further comprehensive investigation.

This study employs NiFe based LDH in conjunction with CeO_2 to function as OER electrocatalyst for elevated-temperature water electrolysers fed with alkaline solution and simulated seawater. The optimal catalyst exhibited the lowest overpotential due to its high oxygen ion diffusion rate and high concentration of oxygen vacancies, as well as superior stability attributed to its high proton conductivity at room temperature. Our experimental findings revealed marked enhancement in both oxygen-ion and proton conductivities of the optimal catalyst under elevated temperature conditions, contributing synergistically to the improvement of its OER activity and stability. Furthermore, enhanced OER activity and suppressed ClOR activity can be achieved through the integration of LDH and CeO_2. Encouraged by the promising outcomes in a typical three-electrode system, an anion exchange membrane water electrolyser (AEMWE) with the optimal catalyst as anode catalyst was assembled, and impressive cell performance was observed at both room temperature and 60 ℃ for water/seawater electrolysis. Our work highlights the importance of performing detailed characterizations of electrocatalysts under operational conditions, as conventional ambient temperature characterizations fail to provide a comprehensive assessment of their catalytic behavior at higher working temperatures.

3.2 Results and Discussion

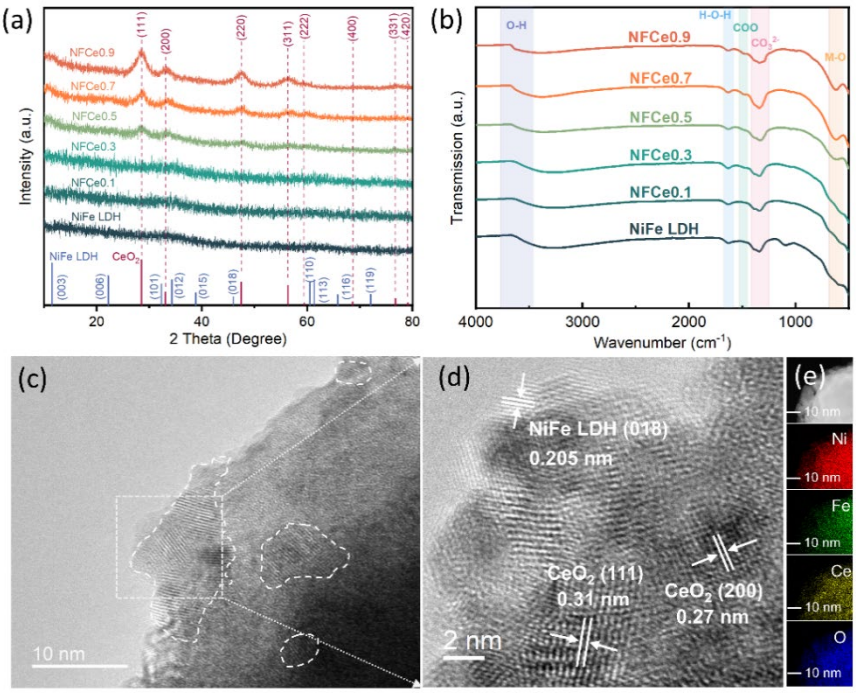

Figure 3.1 (a) XRD patterns and (b) FT-IR spectra of the as-prepared catalysts. (c) HR-TEM image, (d) enlarged HR-TEM image, and (e) the corresponding EDS mapping images of NFCe0.7 sample.

The phase structures of the prepared catalysts were verified by XRD and FT-IR analyses. As depicted in **Figure 3.1a**, the XRD patterns of the deposited pristine NiFe LDH, NFCe0.1, and NFCe0.3 samples exhibit no discernible characteristic diffraction peaks, indicating their possible amorphous nature. In contrast, the NFCe0.5, NFCe0.7, and NFCe0.9 samples exhibit multiple broad peaks that can be indexed to the fluorite structured CeO_2, while the LDH phases continue to exhibit minimal signals. The XRD patterns also show that the emerging CeO_2 improves the crystallinity of LDH, which can be revealed by the gradual increase of (003) peak in LDH phases [27]. FT-IR spectra were adopted to verify the existence of LDH phases within the prepared catalysts. **Figure 3.1b** indicates that all the samples exhibit

characteristic adsorption peaks of LDH materials. The broad and intense absorption bands at 3450 cm^{-1} correspond to the stretching vibration of oxhydryl O–H. The band centered at ~1630 cm^{-1} is attributed to the H–O–H bending vibration of H_2O. The peaks at ~1360 cm^{-1} can be assigned to the stretching vibration mode of CO_3^{2-} within the layers. Below 1000 cm^{-1}, the absorption bands are the stretching vibration of M–O in the LDH structure.

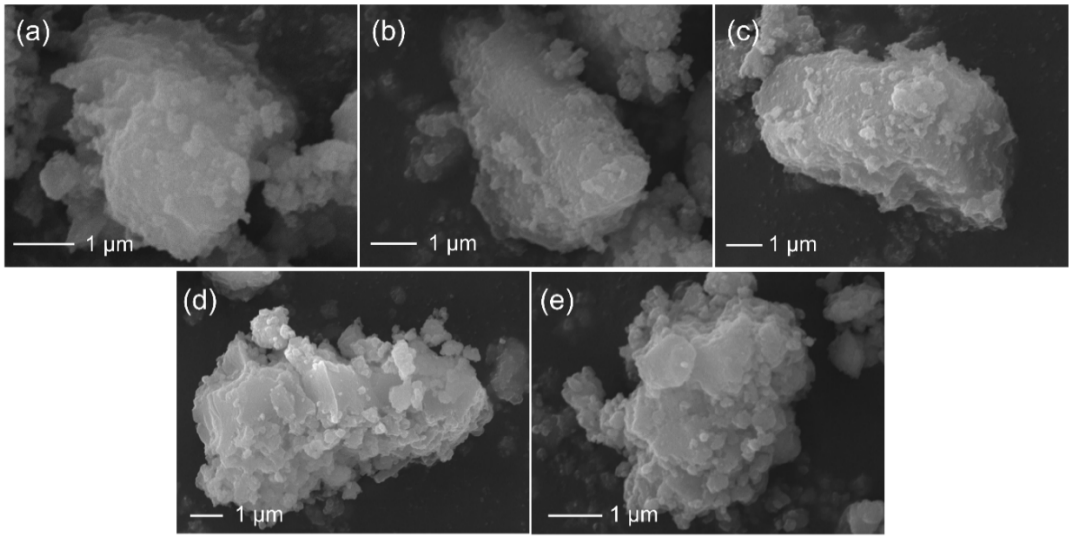

Figure 3.2 SEM images of (a) NiFe LDH, (b) NFCe0.1, (c) NFCe0.3, (d) NFCe0.5, and (e) NFCe0.7 samples.

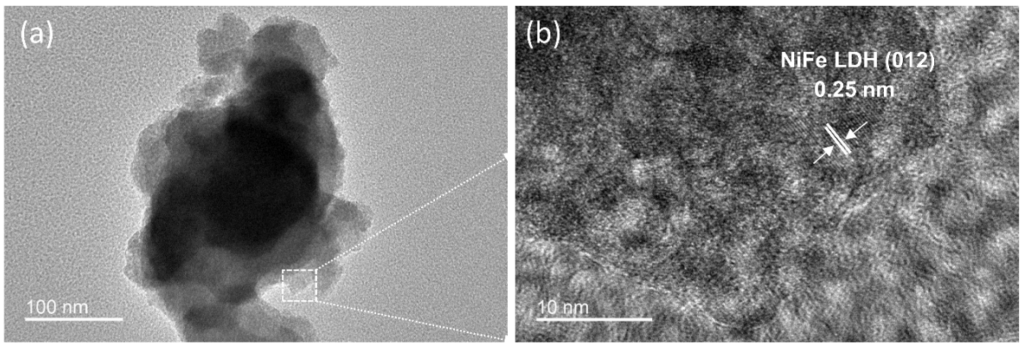

Figure 3.3 (a) TEM image and (b) HR-TEM image of NiFe LDH sample.

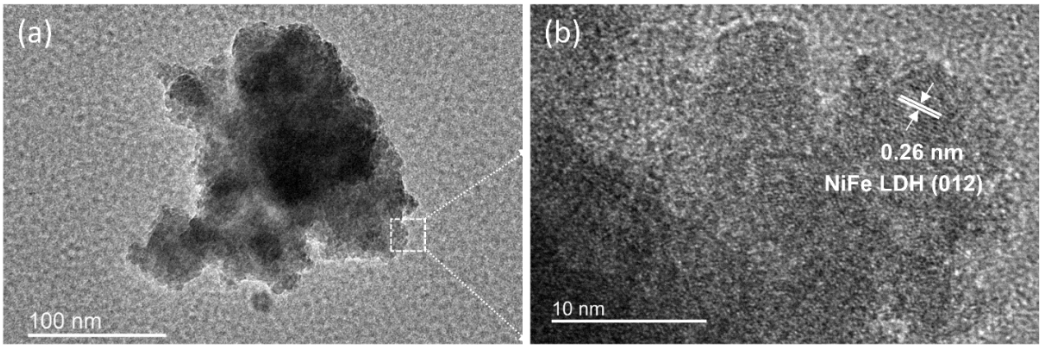

Figure 3.4 (a) TEM image and (b) HR-TEM image of NFCe0.1 sample.

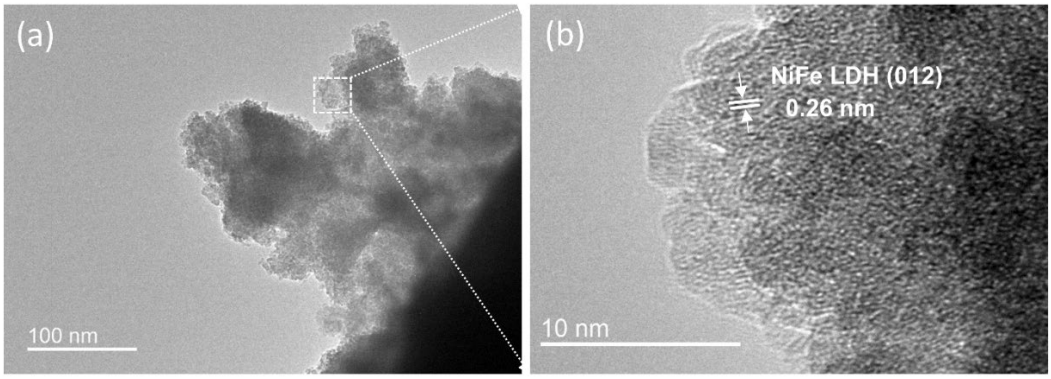

Figure 3.5 (a) TEM image and (b) HR-TEM image of NFCe0.3 sample.

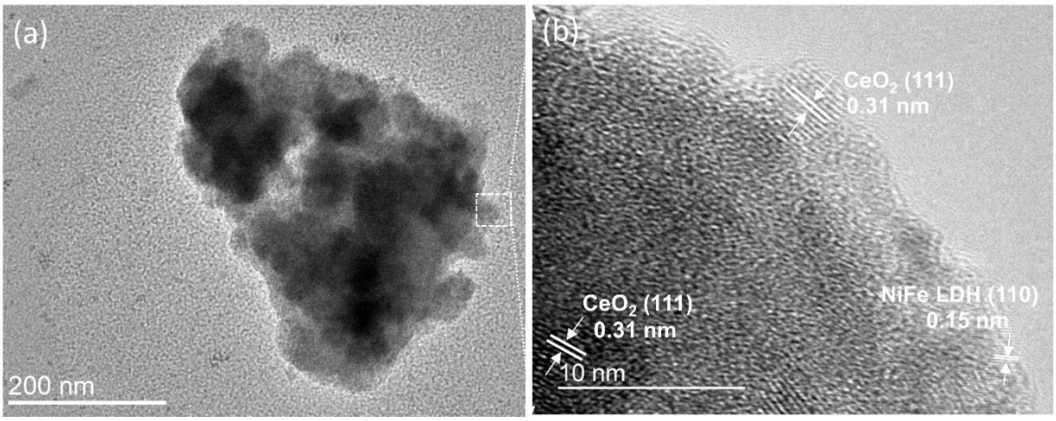

Figure 3.6 (a) TEM image and (b) HR-TEM image of NFCe0.5 sample.

The morphologies and fine structures of the synthesized catalysts were detected by SEM and TEM. SEM images in **Figure 3.2** manifest that the as-prepared catalysts exhibit sheet-stacked

large particle morphologies with inhomogeneous sizes. The high-resolution TEM (HR-TEM) images of the specimens could further reveal the amorphous texture of the LDH phases. As shown in **Figure 3.3-3.5**, the short-range ordered lattice fringes in the HR-TEM images of the NiFe LDH, NFCe0.1, and NFCe0.3 can be well indexed to the (012) plane of the NiFe hydroxide phase. For NFCe0.5 (**Figure 3.6**) and NFCe0.7 (**Figure 3.1c-d**) samples, the *d*-spacings calculated from the distinct lattice fringes are found to be 0.31 and 0.27 nm, corresponding well to the (111) and (200) crystal planes of CeO_2, respectively. Notably, the HR-TEM images of the NFCe0.5 and NFCe0.7 specimens reveal abundant distinct boundaries and intricate interfaces, particularly evident at the edge of the sample particles. The EDS elemental analysis indicates that Ni, Fe, Ce, and O are homogeneously distributed within the structure of NFCe0.7 (**Figure 3.1e**).

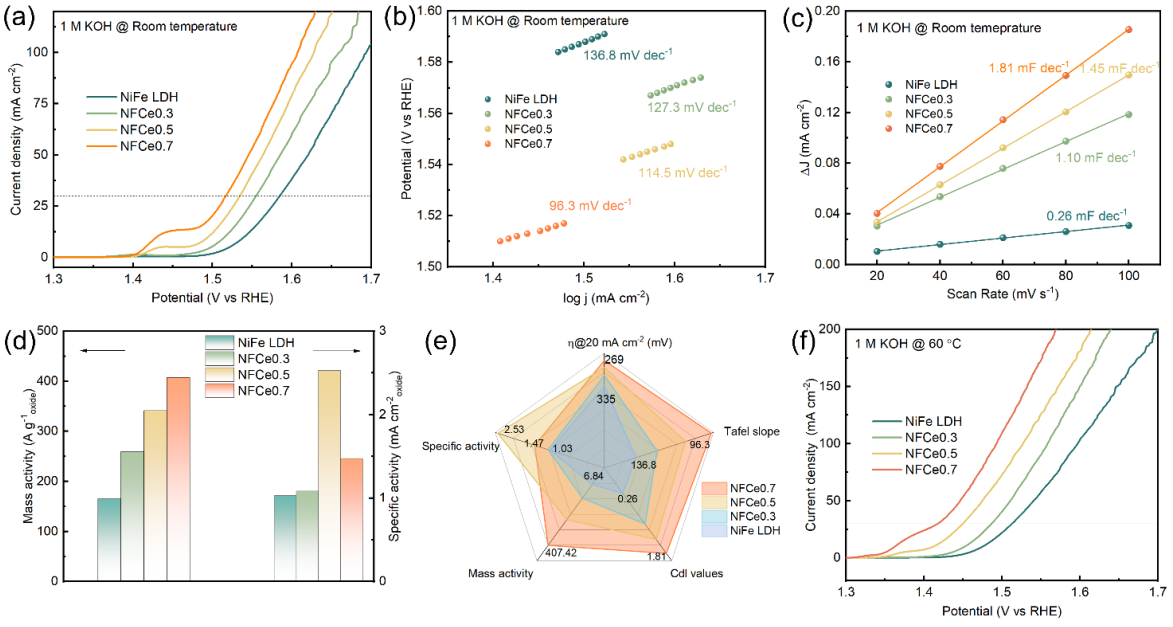

Figure 3.7 (a) LSV curves, (b) Tafel plots, (c) C_{dl} values, (d) mass activity and specific activity at 1.6 V, and (e) Radar map of catalytic activities of different catalysts in 1 M KOH at room temperature. (f) LSV curves of different catalysts in 1 M KOH at 60 ℃.

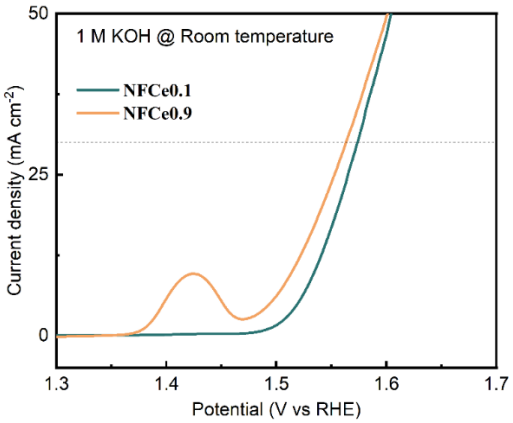

Figure 3.8 LSV curves NFCe0.1 and NFCe0.9 samples.

The electrocatalytic OER activities of the prepared catalysts were initially assessed by a conventional three-electrode system in a 1.0 M KOH solution. The LSV curves obtained at room temperature were presented in **Figure 3.7a** and **Figure 3.8**. It is suggested that compared with the pristine NiFe LDH, NFCe0.1 and NFCe0.3 with the incorporation of Ce suggest enhanced OER activity, which is consistent with the previous reports [28]. A recent study has proved that doping Ce into NiFe-LDH can change the topology of the layers, introduce lattice defects, and promote electronic interactions between LDH and substrate materials, thereby improving electrocatalytic performance [29]. With further increasing the content of Ce, a new phase, i.e., CeO_2, emerged in the samples NFCe0.5 and NFCe0.7, with the further improvement of activity. NFCe0.7 exhibits the highest activity, with the lowest overpotential of 287 mV at 30 mA cm^{-2}, in comparison to NiFe LDH (355 mV), NFCe0.1 (344 mV), NFCe0.3 (325 mV), and NFCe0.5 (304 mV). However, a decrease in activity is observed with further increase in the Ce content, as evidenced by the NFCe0.9 sample (**Figure 3.8**). The Tafel slope (**Figure 3.7b**) of NFCe0.7 also suggests the lowest value of 96.3 mV dec^{-1} for NFCe0.7, surpassing NiFe LDH (136.8 mV dec^{-1}), NFCe0.3 (127.3 mV dec^{-1}), and NFCe0.5 (114.5 mV dec^{-1}), indicating its significantly improved kinetics. The double-layer capacitance (C_{dl}) can be derived from the CV curves at various scan rates

(**Figure 3.9**). As depicted in **Figure 3.7c**, NFCe0.7 demonstrates the highest C_{dl} value, implying its largest electrochemically active surface area. The mass loading-normalized activity (mass activity) and the surface area-normalized activity (specific activity) derived from the nitrogen adsorption-desorption isotherms (**Figure 3.10**) at 1.6 V are presented in **Figure 3.7d**. It is evident that NFCe0.7 delivers the highest mass activity (407.40 A g^{-1}) and superior specific activity (1.47 mA cm^{-2}). The radar map presented in **Figure 3.7e** suggests that NFCe0.7 encompasses the largest area of the map, implying its superiority in aforementioned key parameters.

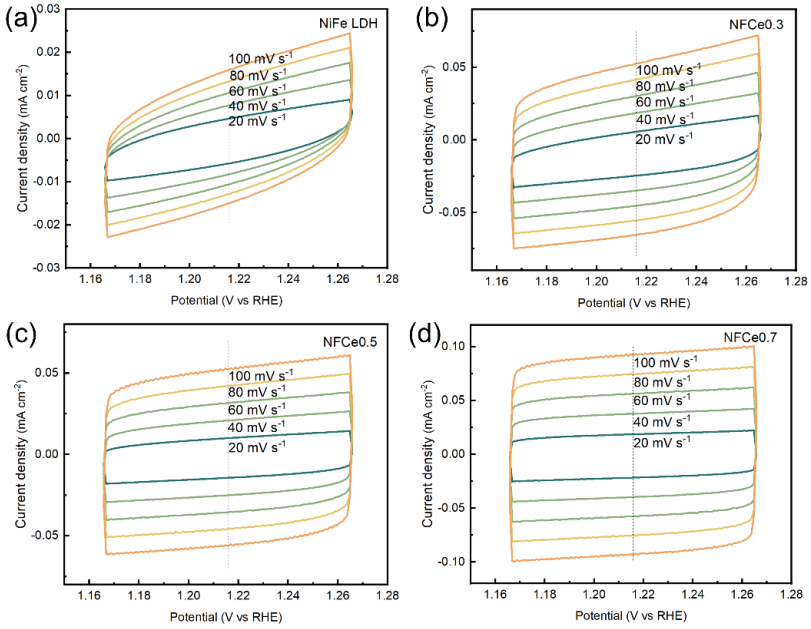

Figure 3.9 CV curves of (a) NiFe LDH, (b) NFCe0.3, (c) NFCe0.5, and (d) NFCe0.7 samples measured at different scan rates.

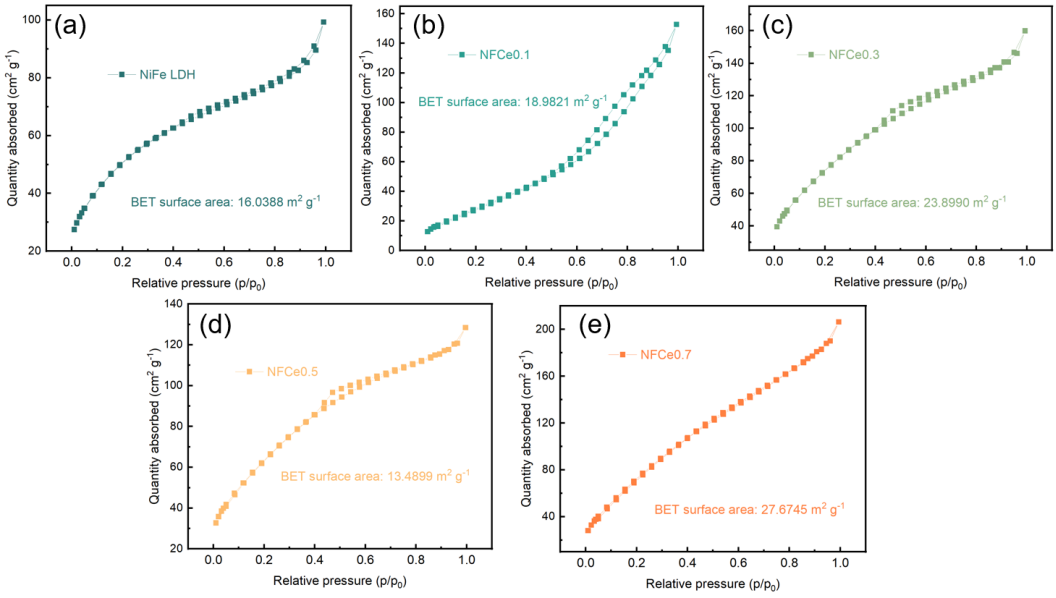

Figure 3.10 The nitrogen adsorption–desorption isotherm profiles of (a) NiFe LDH, (b) NFCe0.1, (c) NFCe0.3, (d) NFCe0.5, and (e) NFCe0.7 samples.

It is widely acknowledged that even a slight modification in the Fe and Ni ratio within NiFe LDH can yield substantial variations in the OER performance. To determine the elemental contents of Ni and Fe in the synthesized samples, ICP-MS analysis was employed. As suggested in **Table 3.1**, upon the gradual incorporation of Ce, the iron content gradually diminishes while the nickel content progressively increases. Notably, in the NFCe0.7 sample, the Fe-to-Ni ratio attains a value of 2:1.

Table 3.1 ICP-MS results of the prepared samples.

Sample	Ni (Con. ppb)	Fe (Con. ppb)	Ce (Con. ppb)
NiFe LDH	0.813	108.27	-
NFCe0.1	1.53	47.03	2.46

NFCe0.3	1.36	20.072	1.33
NFCe0.5	7.62	29.93	7.07
NFCe0.7	7.89	15.68	9.23

To mitigate the influence of varied Fe/Ni ratios on the OER performance, NiFe LDH with a fixed ratio of 2:1 with (NiFe2Ce0.3) and without (NiFe2) Ce, were further synthesized and evaluated as OER catalysts (**Figure 3.11a**, **Table 3.2**). In **Figure 3.11a**, the NiFe2Ce0.3, with the presence of the CeO_2 phase, exhibits a higher degree of crystallinity of LDH phase compared to NiFe2, which is consistent with the observation in **Figure 3.1a**. As illustrated in **Figure 3.11b**, NFCe0.7 continues to exhibit optimal activity, underscoring the need for further investigation to elucidate the origin of its superior performance beyond the influence of the nickel to iron ratio.

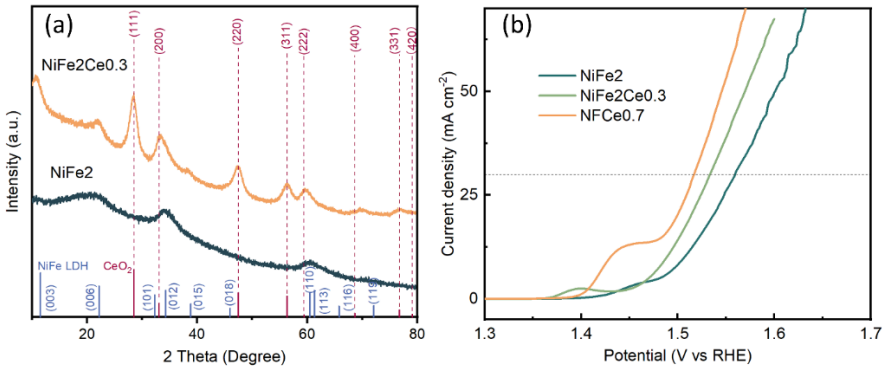

Figure 3.11 (a) XRD patterns and (b) LSV curves of NiFe2 and NiFe2Ce0.3 samples. The LSV of NFCe0.7 is also plotted in (b) for comparison.

Table 3.2 ICP-MS results of the samples with the Fe/Ni ratio.

Sample	Ni (Con. ppb)	Fe (Con. ppb)	Ce (Con. ppb)
NFCe0.7	7.89	15.68	9.23
NiFe2	6.043	11.66	---
NiFe2Ce0.3	13.28	24.547	4.477

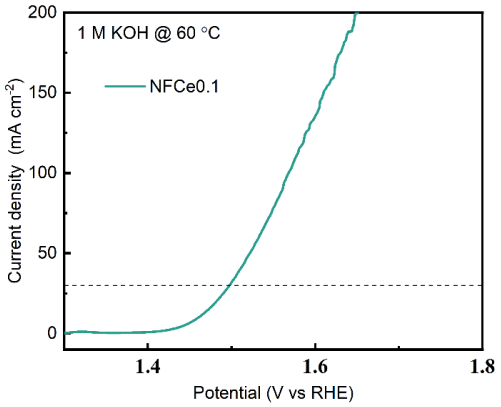

Figure 3.12 LSV curve of NFCe0.1 in 1 M KOH at 60 ℃.

The OER activities of the prepared catalysts at elevated temperatures (60 ℃) were measured. As shown in **Figure 3.7f** and **Figure 3.12**, the catalytic activities for all samples suggest significant improvement with increasing the amount of CeO_2, with the same trend in activity as observed at room temperature (**Figure 3.7a**). NFCe0.7 continues to exhibit the optimal activity, requiring an overpotential of only 186 mV at 30 mA cm^{-2}. **Figure 3.13a** compares the overpotential of all samples at 30 mA cm^{-2} under room temperature and 60 ℃. The overpotentials of all samples at room temperature are notably higher than those at elevated temperature. Theoretically, the chemical rate constant of OER is temperature dependent [30]. With an increase in temperature, both thermodynamics and kinetics could be significantly

enhanced, leading to notably enhanced activities [23, 31]. Hence, it is reasonable to observe improved OER activities in all samples at elevated temperature. However, the decrease in overpotential of NFCe0.7 is notably higher than those of other samples, accounting for 34.6%.

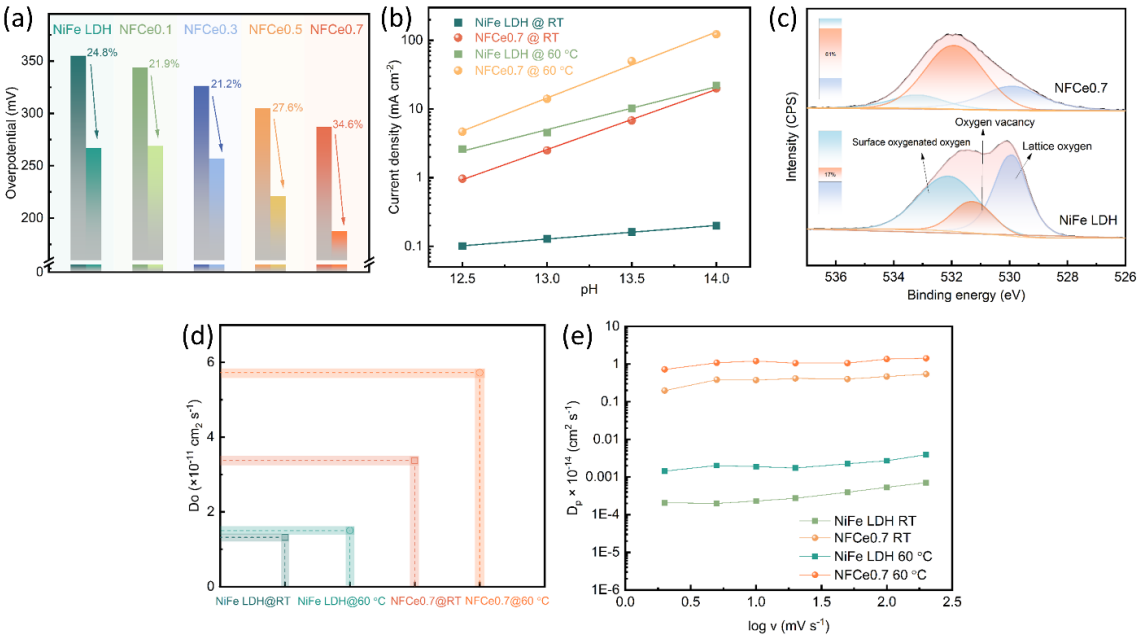

Figure 3.13 Temperature dependent (a) overpotentials at 30 mA cm^{-2} and (b) pH-dependent activities at 1.5 V of NiFe LDH and NFCe0.7 samples. (c) XPS spectra of O 1s for NiFe LDH and NFCe0.7 catalysts. (d) D_O and (e) D_P of NiFe LDH and NFCe0.7 at room temperature (RT) and 60 °C.

In order to elucidate the underlying mechanism behind the superior activity of NFCe0.7 at ambient temperature and the significantly reduced overpotential at elevated temperature, a series of experiments were conducted. Firstly, pH dependent measurements were implemented to understand the OER mechanism for the catalysts. The lattice oxygen mechanism (LOM) is a recently proposed OER mechanism that has been demonstrated to play a pivotal role in enhancing OER activities [32]. As the LOM mechanism entails the redox reaction of lattice oxygen, the produced oxygen molecule involves lattice oxygen and will

create a vacant oxygen site. This process is associated with the decoupled proton-electron transfer step, which resulted in the pH-dependent OER performance. The pH dependent OER performances of NiFe LDH and NFCe0.7 were detected in KOH electrolyte with different pH values at room temperature and 60 °C (**Figure 3.14**). As suggested in **Figure 3.13b**, it is obvious that at room temperature and 60 ℃, both samples show strong pH dependence with the current density improves as pH increases, which identifies the involvement of the LOM pathway of the catalysts during OER. Compared with room temperature, the pH dependence of the catalysts at 60 ℃ becomes more pronounced, as evidenced by the improved slopes of the logarithm of current density versus the electrolyte pH values. Typically, this kind of slope serves as a reliable indicator of lattice oxygen involvement, with a higher value indicating a more favorable lattice-oxygen participation via the LOM pathway [33]. Hence, it can be concluded that increasing temperature is conducive to the participation of lattice oxygen in OER via LOM, thereby achieving improved OER performance.

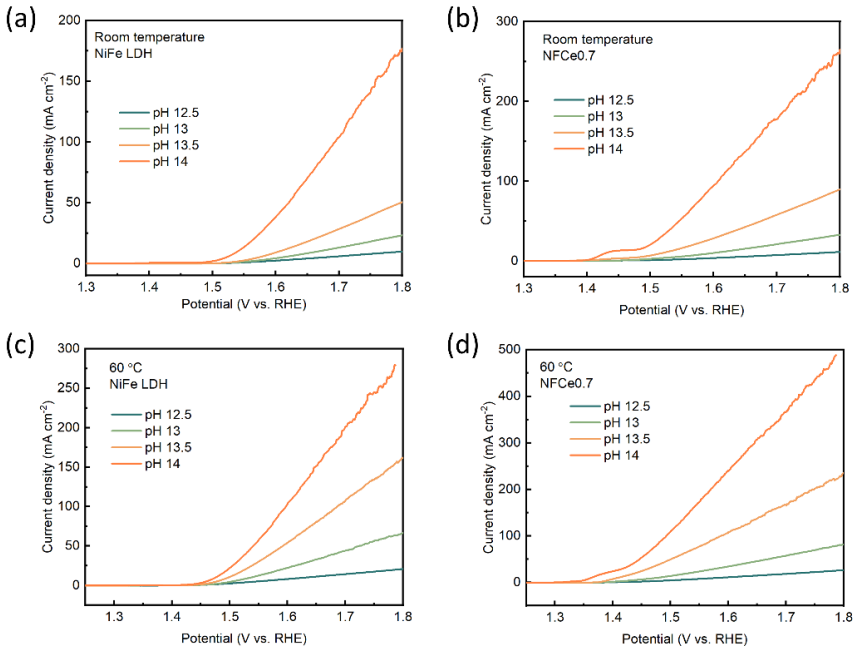

Figure 3.14 The pH-dependent activity of NiFe LDH (a) at room temperature and (c) at 60 ℃ as well as NFCe0.7 (b) at room temperature and (d) at 60 ℃.

For the LOM mechanism, oxygen vacancies have been considered as active sites and its concentration is closely correlated to the oxygen diffusion rates. High concentration of oxygen vacancies could provide abundant oxygen hopping sites, thereby promoting oxygen ion diffusion. To evaluate the oxygen vacancy concentrations of the samples, XPS spectroscopy O 1s analysis was conducted to measure the surface oxygen state (**Figure 3.13c**). The O 1s spectrum of NFCe0.7 exhibit a positive shift in comparison to the pristine NiFe LDH, which may be due to the presence of high-valent Ce in CeO_2. The O 1s spectra can be deconvoluted into three peaks, which are lattice oxygen (~529.6 eV), oxidative oxygen (~531.7 eV), and surface adsorbed water (~532.2 eV). It can be seen that O 1s spectrum of NFCe0.7 suggests a significantly larger proportion of oxidative oxygen (61%) than NiFe LDH (17%), which is an indication of higher concentration of oxygen vacancies and faster oxygen diffusion rates. With the participation of lattice oxygen, quick response to oxygen ion diffusion within the lattice is highly desired for proceeding the whole pathway. The high concentration of oxygen vacancy in NFCe0.7, which exhibits significant intensity that obscures the intensity of the lower concentrations of lattice oxygen and surface-adsorbed water. This also explains why the O 1s spectrum of NiFe LDH is divided into two peaks, whereas NFCe0.7 displays only a single peak. To provide solid evidence of the increased oxygen vacancies of NFCe0.7 compared to the pristine catalyst, EPR spectra were obtained. A pure CeO_2 phase was also synthesized (**Figure 3.15a**) and subjected to EPR measurement for comparison. As depicted in **Figure 3.15b**, the EPR spectrum of NFCe0.7 exhibits a greater intensity than that of NiFe LDH, indicating a higher concentration of oxygen vacancies.

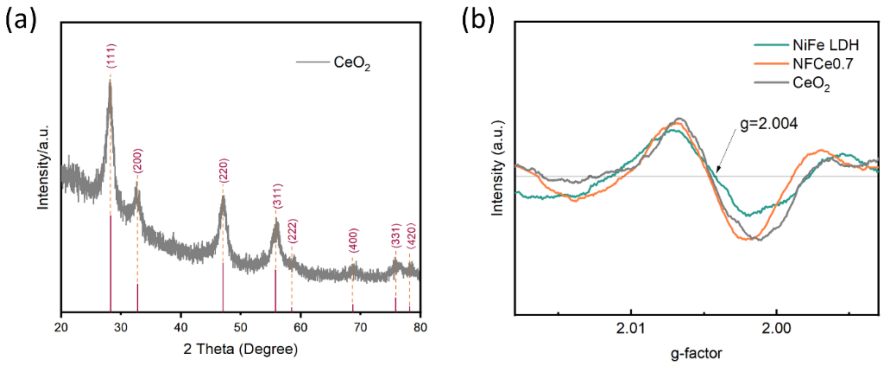

Figure 3.15 (a) XRD pattern of pure CeO_2. (b) EPR spectra of NiFe LDH, NFCe0.7, and pure CeO_2.

The mixed oxygen and proton conductivities of CeO_2 have been well demonstrated under high temperatures (typically higher than 600 °C), yet its ionic conductivities would decrease as temperature reduces [24]. To evaluate the oxygen ion diffusion coefficients of the catalysts at desirable temperatures (room temperature and 60 °C), the CV and chronoamperometry tests were integrated based on a bounded three-dimensional diffusion model. The redox peaks observed in CV curves indicate the insertion and extraction of oxygen ions, with larger redox peak intensities generally indicate a greater tendency for oxygen insertion/extraction [34, 35]. After CV measurements, chronoamperometry tests were performed and plotted as current versus $t^{-1/2}$. By applying an anodic potential of 50 mV more than $E_{1/2}$ that is the potential halfway between the redox peak currents, the current density response to the operation time can be recorded (see **Figure 3.16**). The results indicate a significant increase in the current of NFCe0.7 compared to that of NiFe LDH. Additionally, the current of NFCe0.7 at 60 °C increases notably faster than that at room temperature, suggesting a higher oxygen ion diffusion rate at 60 °C compared to room temperature. The D_O value can be evaluated from the slope of the linear region according to the bounded 3D diffusion model [36]. The oxygen diffusion coefficients (D_O) were calculated and shown in **Figure 3.13d**. The D_O value of

NFCe0.7 is found to be 3.37×10^{-11} cm^2 s^{-1}, which is more than twice that of NiFe LDH (1.32×10^{-11} cm^2 s^{-1}) at room temperatures, and the D_O value of NFCe0.7 at 60 °C (5.73×10^{-11} cm^2 s^{-1}) is 1.7 times higher than that at room temperature, proving enhanced oxygen diffusion rate of the NFCe0.7 sample, especially at elevated temperature. The higher concentration of oxygen vacancies and the superior oxygen ion diffusion rates are expected to notably improve the activity of NFCe0.7 for both ambient and elevated temperatures. CeO_2 also exhibits exceptional proton conductivity at high temperatures, yet its proton conductivity at lower temperatures (below 100 °C) and the consequent influence on OER remains uncertain. Fortunately, a recent study has witnessed its proton conductivity under room temperature, which paves the way for its proton conductive application even at room temperature [26].

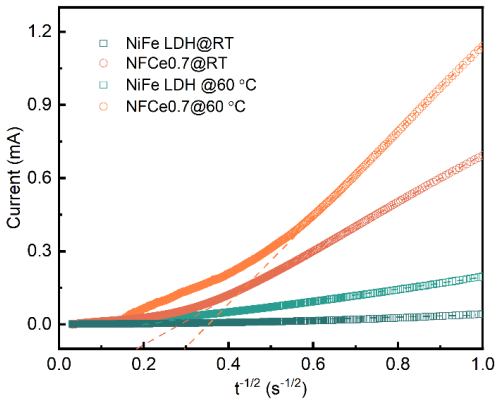

Figure 3.16 Chronoamperometric measurements of the oxygen diffusion coefficients (D_O) of NiFe LDH and NFCe0.7 at room temperature and 60 °C.

The proton diffusion coefficients (D_P) were determined by cyclic voltammetry tests at different scan rates (**Figure 3.17**), where the diffusion of protons to the electrode surface generates a measurable current. The results show that the process is diffusion-controlled and the peak current increases with the increase of the scanning rate. This current is then analyzed using the Randles-Sevcik equation to determine the diffusion coefficient, providing insights

into the transport properties of protons in the system. As shown in **Figure 3.13e**, the proton diffusion coefficients of NFCe0.7 significantly surpass the counterpart NiFe LDH for both temperatures. Larger proton diffusion coefficient endows the NFCe0.7 material with rapid adsorption/desorption capability of protons during OER process in alkaline electrolyte.

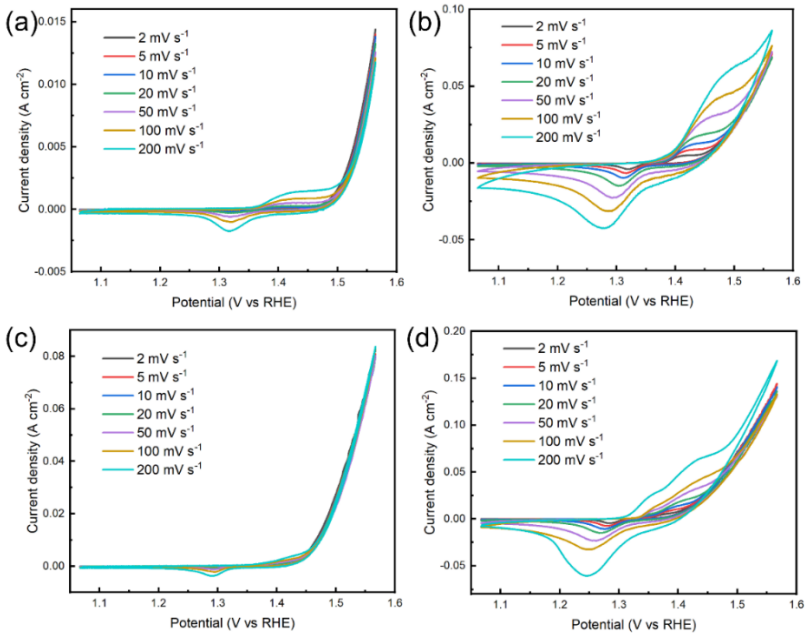

Figure 3.17 CV curves of (a) NiFe LDH and (b) NFCe0.7 samples measured at different scan rates at room temperature. CV curves of (c) NiFe LDH and (d) NFCe0.7 samples measured at different scan rates at 60 °C.

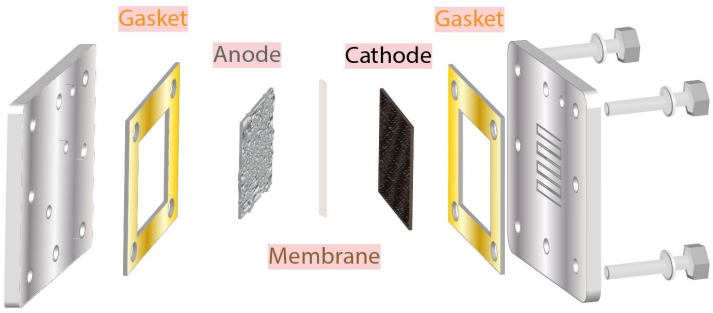

Figure 3.18 Schematic diagram of the AEMWE device.

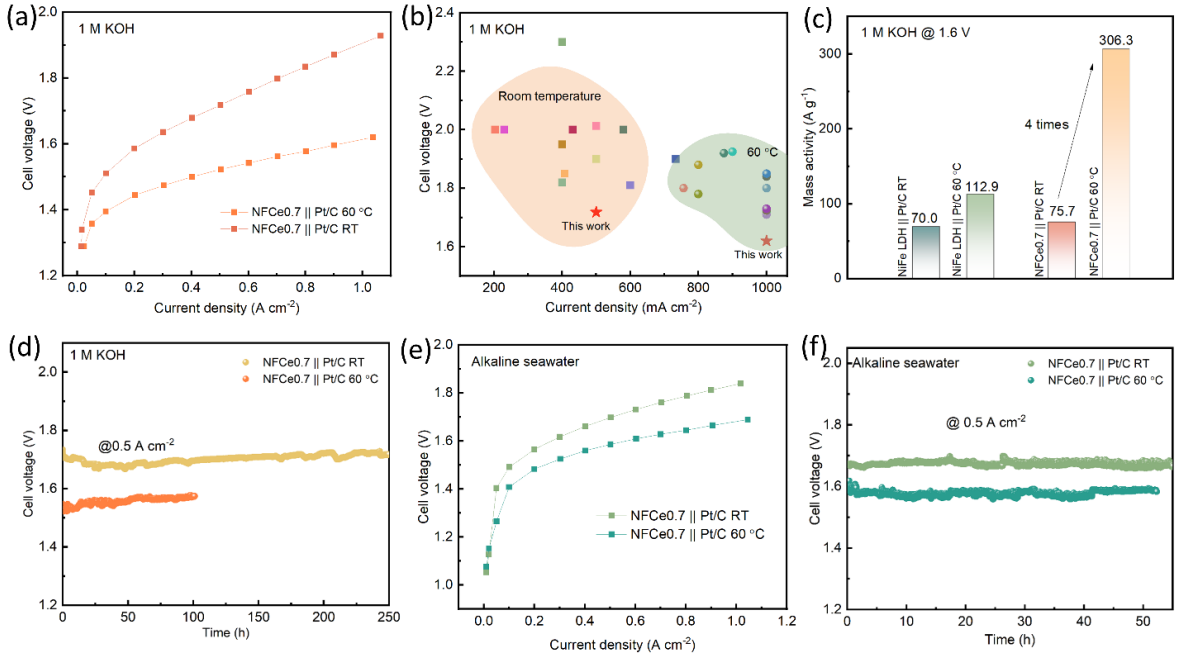

Figure 3.19 (a) NFCe0.7 || Pt/C electrolyser performance in 1 M KOH. (b) Comparison of electrolyser performance [37-60]. (c) Mass activity comparison. (d) Durability tests of the NFCe0.7 || Pt/C single cell in 1 M KOH. (e) Electrolyser performance and (f) durability tests of NFCe0.7 || Pt/C electrolyser in simulated seawater.

Anion exchange membrane water electrolyser (AEMWE) single cells were assembled to evaluate the practical application potential of the developed catalyst. The anion exchange membrane employed was the Sustainion® 37-50 membrane produced by Dioxide Materials. Shown in **Figure 3.18** is the schematic diagram of the assembled AEMWE. Feeding 1 M KOH as electrolyte, an AEMWE with NFCe0.7 as anodic catalyst and Pt/C as cathodic catalyst (denoted as NFCe0.7 || Pt/C) only requires 1.72 and 1.52 V_{cell} to deliver a current density of 0.5 A cm^{-2} at room temperature and 60 °C, respectively, superior to that of the AEMWE with NiFe LDH as anodic catalyst (denoted as NiFe LDH || Pt/C) (**Figure 3.19a** and **Figure 3.20a**). The polarization curves of the NFCe0.7 || Pt/C electrolyser at 40 and 50 °C have also been plotted in **Figure 3.21**. A comparison of the cell performance at room temperature and 60 °C achieved by the NFCe0.7 || Pt/C system and the state-of-the-art

AEMWEs has been plotted in **Figure 3.19b**, which highlights the superior activity of the assembled NFCe0.7 || Pt/C system. **Figure 3.19c** displays the mass activity of the two electrolyser systems at 1.6 V under room temperature and 60 °C. It suggests that although the two cells show comparable mass activity at room temperature, the mass activity of the NFCe0.7 || Pt/C electrolyser at 60 °C is almost three times that of the NiFe LDH || Pt/C cell. The results highlight the importance of high temperature characterizations of the OER process for practical applications under service conditions.

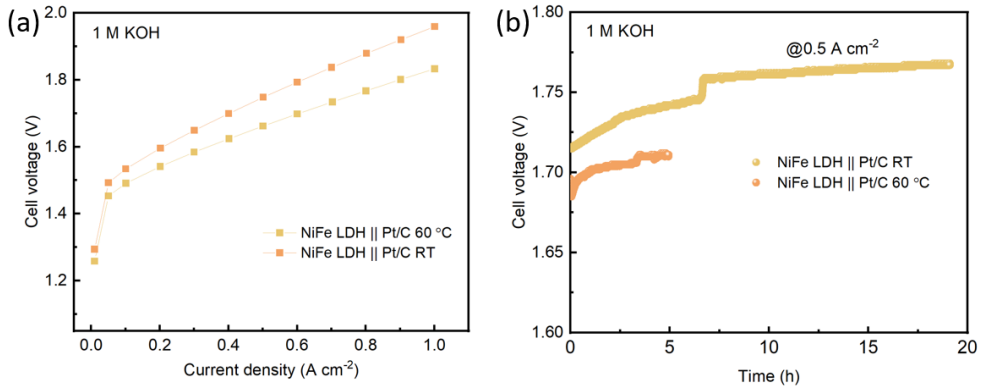

Figure 3.20 (a) Single cell performance and (b) stability tests of the NiFe LDH || Pt/C electrolysers in 1 M KOH solution at room temperature and 60 °C.

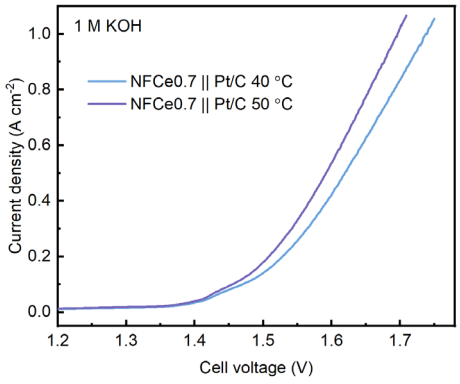

Figure 3.21 Single cell performance of the NFCe0.7 || Pt/C electrolyser in 1 M KOH solution at 40 and 50 °C.

Long-term stability tests were carried out at a current density of 0.5 A cm^{-2} to evaluate the practical viability of hydrogen production using the assembled AEMWEs. As shown in **Figure 3.20b**, the NiFe LDH || Pt/C single cell suggests significant performance degradation at 0.5 A cm^{-2} within a short time for both room temperature and 60 °C. This observation is consistent with many previous reports [61, 62]. By contrast, the NFCe0.7 || Pt/C system suggests significantly improved stability, where the device can operate stably over 250 and 100 h at a current density of 0.5 A cm^{-2} at room temperature and 60 °C, respectively (**Figure 3.19d**). In addition, elevated temperature typically represents more severe operating conditions, which may promote the dissolution of NiFe LDHs. Nevertheless, the NFCe0.7-based electrolyser still demonstrates favorable durability for over 100 hours, owing to the high proton transfer capability of NFCe0.7 at 60 °C.

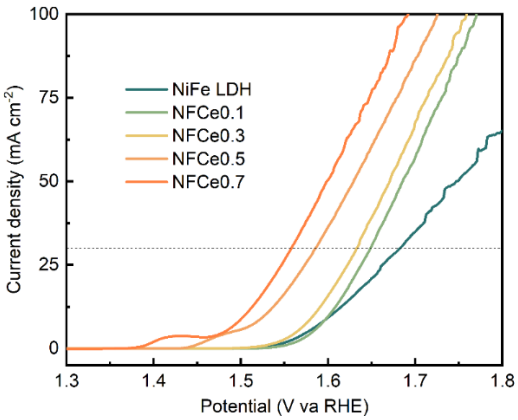

Figure 3.22 OER performance of the prepared samples in alkaline seawater.

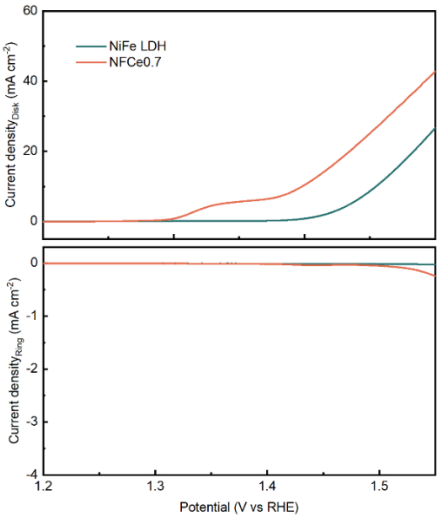

Figure 3.23 RRDE voltammograms of the NiFe LDH and NFCe0.7 samples in simulated seawater.

To evaluate the OER selectivity and application potential of the developed catalyst for seawater electrolysis, electrochemical tests in alkaline-simulated seawater (1.0 M KOH + 0.5 M NaCl) with both conventional three-electrode system and AEMWE single cell were conducted. For the three-electrode system (**Figure 3.22**), NiFe LDH and NFCe0.7 demonstrate overpotentials of 453 and 328 mV, respectively, at 30 mA cm^{-2} in simulated alkaline seawater. A rotating ring-disk electrode (RRDE) was used to assess the selectivity of the electrocatalysts in simulated seawater, as the ring current signifies the reduction signal of ClO^- produced by the electrode, thereby confirming the occurrence of ClOR. As shown in **Figure 3.23**, no significant currents were observed on the Pt ring during the scan ranges for both samples, indicating favorable selectivity of OER for the electrocatalysts. The consequent AEMWE single cell performances were also tested and shown in **Figure 3.19e**. To achieve a current density of 0.5 A cm^{-2}, the NFCe0.7 || Pt/C system in simulated seawater necessitates a cell voltage of 1.70 and 1.59 V_{cell} at room temperature and 60 °C, respectively, much lower than that of NiFe LDH || Pt/C system at room temperature (1.71 V_{cell}) and 60 °C (1.66 V_{cell})

(**Figure 3.24**).

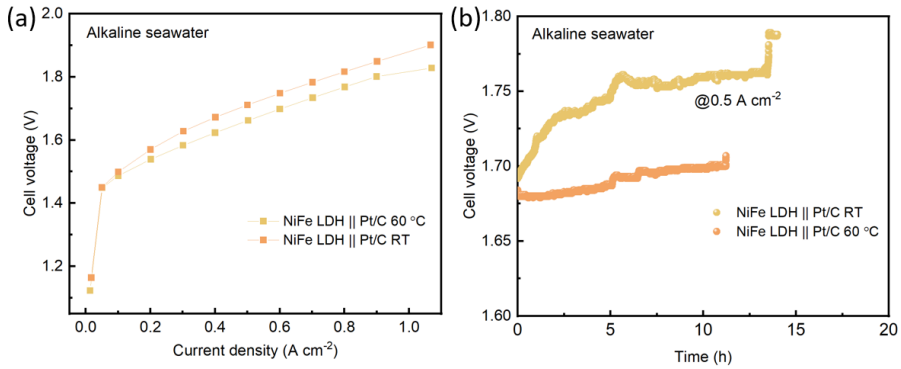

Figure 3.24 (a) Single cell performance and (b) stability tests of the NiFe LDH || Pt/C electrolysers in simulated seawater at room temperature and 60 °C.

Comparing the AEMWE activity of NFCe0.7 in 1 M KOH and seawater reveals that the AEMWE activity in 1 M KOH is inferior to that in seawater under room temperature, whereas the activity in 1 M KOH surpasses that in seawater at 60 °C. This is because at room temperature, the presence of additional Na^+ and Cl^- in simulated seawater can enhance the ionic conductivity of the electrolyte [63, 64]. Thus, the NFC0.7 exhibits enhanced OER activity in seawater compared to that in 1 M KOH. With increasing temperature, the absorption of Cl^- plays an increasing role in deactivating catalytically active sites, thereby reducing the activity of NFCe0.7 in seawater at 60 °C. It is notable that the overall water splitting voltages of both cells fall within the safe voltage range of selective OER, for which highly selective OER can be expected. The produced amounts of ClO^- of the two electrolysers at different times were measured by UV-vis during chronopotentiometry test at 0.8 A cm^{-2}. According to a previous report, there exists a characteristic absorption peak for ClO^- at 292 nm in the UV-Vis spectrum [65]. The absorbance of different concentrations of sodium hypochlorite standard solutions were measured by UV-vis spectroscopy and fitted linearly (**Figure 3.25a**). The produced amounts of ClO^- of the two electrolysers can then be determined based on the

equation obtained in **Figure 3.25a**. As depicted in **Figure 3.25b**, the amount of ClO^- generated by the NFCe0.7 || Pt/C cell is evidently lower than that of the NiFe LDH || Pt/C system at 10 min, 30 min, and 1 h, indicating that NFCe0.7 exhibits greater selectivity towards OER rather than ClOR. The superior OER selectivity of NFCe0.7 mainly stems from its remarkable oxygen ion diffusion rate. Augmenting the oxygen ion diffusion rate has been demonstrated to facilitate efficient oxygen transport and the fast replenishment of consumed surface lattice oxygen, thereby promoting the OER process and mitigating the occurrence of competing reactions, ultimately achieving high selectivity towards OER. **Figure 3.19f** illustrates the stability tests of the NFCe0.7-based electrolyser. It is demonstrated that the NFCe0.7-based electrolyser could operate consistently for over 50 hours at both temperatures, suggesting its significant potential of NFCe0.7 in the practical application of saline water electrolysis.

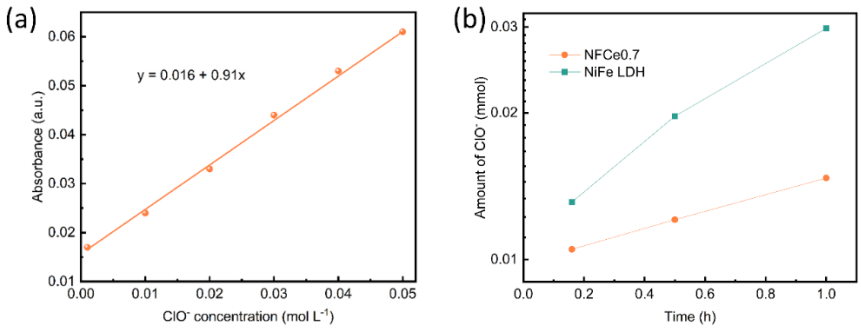

Figure 3.25 (a) Fitting curve of ClO^- concentration versus UV-vis absorbance intensity. (b)The amounts of ClO^- generated in simulated seawater from the NiFe LDH || Pt/C and NFCe0.7 || Pt/C electrolysers at the current density of 0.8 A cm^{-2}.

Based on the acquired findings, a potential catalytic mechanism for the superior performance and durability of the NFCe0.7 electrocatalyst-based cell was hypothesized and schematically illustrated. For the samples without CeO_2 phase (**Figure 3.26a**), the LDH phases are fully

exposed to the alkaline solution containing a high concentration of OH^- (and Cl^-). Since the interlayer basal plane in LDH is also capable of catalyzing OER, the protons will be released during the decoupled proton-electron transfer step. According to previous report, the small interlayer distance of NiFe LDH would impede the diffusion of the proton acceptors, i.e., OH^-, towards the interlayers during alkaline OER process, resulting in a local concentrated acidic environment within the interlayers and the subsequent structural collapse, thus leading to the rapid deactivation of the material [66]. This is consistent with the observed poor stability of NiFe LDH. Recently, significant advancements have been made in understanding the local microenvironment of active sites during the OER process, demonstrating a strong correlation between the local microenvironment and the electrochemical performance [67, 68]. The high concentration of Cl^- in the simulated alkaline seawater would potentially accumulate and absorb on the surface of the LDH phase, impeding the transport of OH^- and undergoing oxidation to ClO^-. The generated ClO^-, in turn, is corrosive to the LDH structure and can lead to electrochemical instability during the electrocatalytic process. The high concentration of ClO^- and the rapidly increased potential during the stability test of NiFe LDH in simulated alkaline seawater may serve to confirm this.

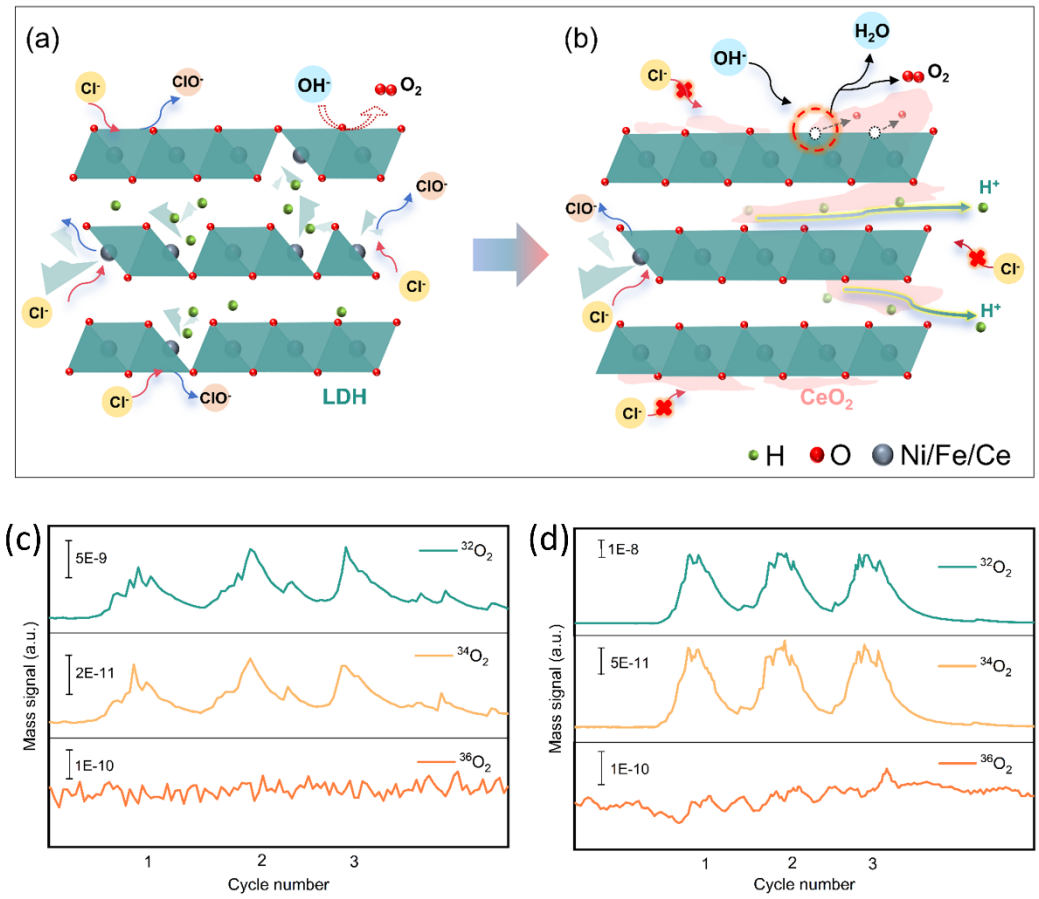

Figure 3.26 Mechanistic illustration of the enhanced activity, stability, and selectivity of OER (a) without and (b) with the mixed ionic conductor CeO_2. DEMS signals of O_2 products for ^{18}O-labeled (c) NiFe LDH and (d) NFCe0.7 electrocatalysts in 1 M KOH with $H_2{}^{16}O$ solvent.

Conversely, the existence of the CeO_2 phase with high mixed ionic conductivity significantly improves the activity, stability, and selectivity of NFCe0.7 electrocatalyst for OER, as suggested in **Figure 3.26b**. It can be observed from the HR-TEM image that there are abundant distinct boundaries and intricate interfaces between the emerged CeO_2 phase and the LDH phase, particularly noticeable at the edge of the sample particles. Physically, the CeO_2 particles may partially cover the surface of the LDH phase, thus inhibiting the direct adsorption of Cl^- to some extent. However, the direct adsorption of OH^- on LDH may also be

impeded due to the partial coverage of the CeO_2 particles. Fortunately, large amount of oxygen vacancies at the interfaces between LDH phase and CeO_2 phase originated from the local electron potential difference between the two phases can provide additional active sites for OER activity [25]. This can be verified by the XPS spectra, which demonstrate a higher concentration of lower valence states of Ni^{2+} and Fe^{2+} in NFCe0.7 compared to the pristine NiFe LDH (**Figure 3.27**).

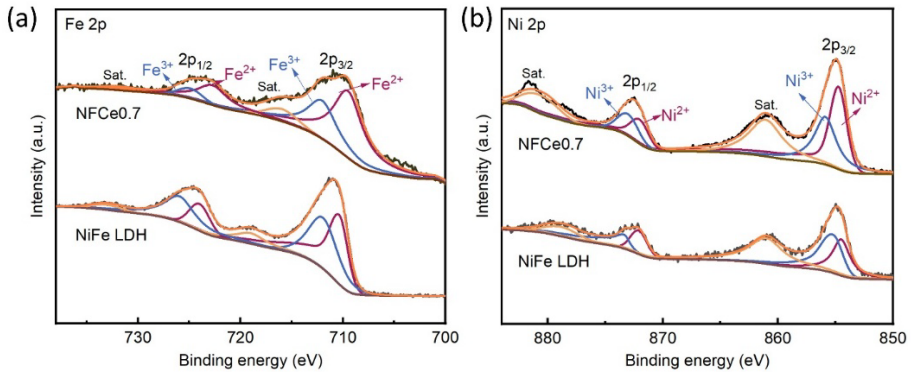

Figure 3.27 XPS spectra of (a) Fe 2p and (b) Ni 2p for NiFe LDH and NFCe0.7 samples.

The reduction in valence state is accompanied by the generation of oxygen vacancies to maintain charge neutrality of the material. The formation of these abundant oxygen vacancies is expected to facilitate the LOM pathway. To provide direct experimental evidence supporting the involvement of the LOM during OER, online DEMS measurements with isotope labeling were conducted. For pathway dominated by LOM mechanism, the oxygen exchange and release processes between the surface-adsorbed ^{18}O species and lattice oxygen would yield products with both $^{36}O_2$ and $^{34}O_2$. While for AEM mechanism, the absence of $^{36}O_2$ signal would be expected, as this pathway does not involve lattice oxygen in the whole reaction process. The results indicate that the oxygen evolution products from NiFe LDH predominantly exhibit significant signals for $^{32}O_2$ and $^{34}O_2$, with no detectable $^{36}O_2$ signal (**Figure 3.26c**), suggesting that the adsorption evolution mechanism (AEM) is the dominant

pathway for OER in NiFe LDH. In contrast, the NFCe0.7 catalyst displays an obvious signal for $^{36}O_2$ in addition to $^{32}O_2$ and $^{34}O_2$ (**Figure 3.26d**), which provides direct experimental evidence for the involvement of the LOM in the OER process for NFCe0.7 catalyst, consistent well with the preceding analyses. Besides, NFCe0.7 exhibit higher levels of $^{34}O_2$ signals than NiFe LDH, further proving the participation of lattice oxygen during electrocatalysis. Consequently, despite the partial physical coverage of the LDH surface by CeO_2, the activity of LDH is not diminished, but instead, it prevents the adsorption and oxidation of Cl^-, thereby improving the selectivity of the catalyst towards OER and the stability of seawater electrolysis. The introduced oxygen vacancies can facilitate electron/ion migration rates, promote charge transfer, and provide additional active sites, thereby enhancing catalytic activities. Hence, the NFCe0.7 electrocatalyst shows enhanced OER activity at room temperature, which is confirmed by the small overpotential of NFCe0.7. Additionally, the significantly improved oxygen ion diffusion rate of NFCe0.7 at elevated temperature could bring extra activity to OER under industrial operation condition, which can be verified by the mass activity comparison. The mass activity of the NFCe0.7-based electrolyser at 60 °C is almost three times that of the NiFe LDH based cell, while the mass activities of the two cells present comparable values at room temperature. This result also highlights the significance of characterizing electrocatalysts and OER process at practical operation temperatures, as catalysts may present different properties during the OER under realistic application conditions. The result also suggests that the high proton diffusion coefficients of NFCe0.7 are conducive to facilitating the transfer of released protons and avoiding the accumulation of protons within the LDH interlayers to relieve the local concentrated acidic environment during OER process, thus suppressing the dissolution of metal ions and the subsequent structure collapse. Besides, the abundant interfaces suggests that the deposition of CeO_2 may hinder the continuous growth of the LDH, thereby exposing

more surfaces and edges. This exposure can increase the number of active sites while simultaneously reducing the distance for protons to migrate out of the layers, ultimately enhancing its stability. Consequently, NFCe0.7 achieves significantly enhanced stability in comparison to NiFe LDH due to the higher proton diffusion, faster proton transfer, and reduced distance of proton migration.

3.3 Conclusion

In summary, a series of CeO_2/NiFe-based LDH composites were successfully synthesized by one-step electrodeposition method and utilized as anodic catalysts in water/seawater electrolysis. Among the developed catalysts, NFCe0.7 sample exhibits the best electrocatalytic OER activity, selectivity, and stability, stemming from its abundant oxygen vacancies, outstanding oxygen ion conductivity, and enhanced proton conductivity, especially at a high temperature of 60 °C. Our results show that, aiming at practical applications, the electrochemical characterizations of electrocatalysts and cells at room temperature are not enough, and high temperature characterizations under service conditions are needed.

3.4 References

1. R. R. Beswick, A. M. Oliveira and Y. Yan, *ACS Energy Letters*, 2021, **6**, 3167-3169.
2. M. Khan, T. Al-Attas, S. Roy, M. M. Rahman, N. Ghaffour, V. Thangadurai, S. Larter, J. Hu, P. M. Ajayan and M. G. Kibria, *Energy & Environmental Science*, 2021, **14**, 4831-4839.
3. M. Tahir, L. Pan, F. Idrees, X. Zhang, L. Wang, J.-J. Zou and Z. L. Wang, *Nano Energy*, 2017, **37**, 136-157.
4. L. Gao, X. Cui, C. D. Sewell, J. Li and Z. Lin, *Chemical Society Reviews*, 2021, **50**, 8428-8469.

5. Y. Xu, C. Wang, Y. Huang and J. Fu, *Nano Energy*, 2021, **80**, 105545.

6. L. Li, X. Cao, J. Huo, J. Qu, W. Chen, C. Liu, Y. Zhao, H. Liu and G. Wang, *Journal of Energy Chemistry*, 2023, **76**, 195-213.

7. L. Mu, S. Qiu, G. Zhao, W. Liao, N. Zhao and X. Xu, *Journal of Materials Chemistry A*, 2024, **12**, 1714-1724.

8. L. Yu, J. Xiao, C. Huang, J. Zhou, M. Qiu, Y. Yu, Z. Ren, C.-W. Chu and J. C. Yu, *Proceedings of the National Academy of Sciences*, 2022, **119**, e2202382119.

9. W. Tong, M. Forster, F. Dionigi, S. Dresp, R. Sadeghi Erami, P. Strasser, A. J. Cowan and P. Farràs, *Nature Energy*, 2020, **5**, 367-377.

10. F. Sun, J. Qin, Z. Wang, M. Yu, X. Wu, X. Sun and J. Qiu, *Nature communications*, 2021, **12**, 4182.

11. X. Liu, J. Chi, H. Mao and L. Wang, *Advanced Energy Materials*, 2023, **13**, 2301438.

12. L. Wu, L. Yu, F. Zhang, B. McElhenny, D. Luo, A. Karim, S. Chen and Z. Ren, *Advanced Functional Materials*, 2021, **31**, 2006484.

13. H. Yang, M. Driess and P. W. Menezes, *Advanced energy materials*, 2021, **11**, 2102074.

14. H. Jin, J. Xu, H. Liu, H. Shen, H. Yu, M. Jaroniec, Y. Zheng and S.-Z. Qiao, *Science Advances*, 2023, **9**, eadi7755.

15. Y. Wu, M. Chen, H. Sun, T. Zhou, X. Chen, G. Na, G. Qiu, D. Li, N. Yang, H. Zheng, Y. Chen, B. Wang, J. Zhao, Y. Zhang, J. Zhang, F. Liu, H. Cui, T. He and Q. Liu, *Applied Catalysis B: Environment and Energy*, 2025, **360**, 124548.

16. D. Zhou, P. Li, X. Lin, A. McKinley, Y. Kuang, W. Liu, W.-F. Lin, X. Sun and X. Duan, *Chemical Society Reviews*, 2021, **50**, 8790-8817.

17. L. Liu, Y. Chen, Q. Zhang, Z. Liu, K. Yue, Y. Cheng, D. Li, Z. Zhu, J. Li and Y. Wang, *Applied Catalysis B: Environment and Energy*, 2024, **354**, 124140.

18. H. Chen, P. Liu, W. Li, W. Xu, Y. Wen, S. Zhang, L. Yi, Y. Dai, X. Chen, S. Dai, Z. Tian, L. Chen and Z. Lu, *Advanced Materials*, 2024, **36**, 2411302.

19. B. Zhang, S. Liu, S. Zhang, Y. Cao, H. Wang, C. Han and J. Sun, *Small*, 2022, **18**, 2203852.

20. H. Chen, R.-T. Gao, H. Chen, Y. Yang, L. Wu and L. Wang, *Advanced Functional Materials*, 2024, **34**, 2315674.

21. Z. Wang, L. Wang, L. Chu, M. Yang and G. Wang, *ACS Sustainable Chemistry & Engineering*, 2024, **12**, 11628-11637.

22. H. Sun, X. Xu, H. Kim, W. Jung, W. Zhou and Z. Shao, *Energy & Environmental Materials*, 2023, **6**, e12441.

23. W. Zhang, M. Liu, X. Gu, Y. Shi, Z. Deng and N. Cai, *Chemical Reviews*, 2023, **123**, 7119-7192.

24. A. Tschöpe, E. Sommer and R. Birringer, *Solid State Ionics*, 2001, **139**, 255-265.

25. X. Wang, Y. Yang, L. Diao, Y. Tang, F. He, E. Liu, C. He, C. Shi, J. Li and J. Sha, *ACS applied materials & interfaces*, 2018, **10**, 35145-35153.

26. P. Simons, S. A. Schenk, M. A. Gysel, L. F. Olbrich and J. L. M. Rupp, *Advanced Materials*, 2022, **34**, 2109075.

27. B. Zhang, N. Zhang, G. Zhao, L. Mu, W. Liao, S. Qiu and X. Xu, *Journal of Colloid and Interface Science*, 2024, **665**, 1054-1064.

28. M. Liu, K.-A. Min, B. Han and L. Y. S. Lee, *Advanced Energy Materials*, 2021, **11**, 2101281.

29. H. Xu, B. Wang, C. Shan, P. Xi, W. Liu and Y. Tang, *ACS Applied Materials & Interfaces*, 2018, **10**, 6336-6345.

30. B. Zhang, X. Zheng, O. Voznyy, R. Comin, M. Bajdich, M. García-Melchor, L. Han, J. Xu, M. Liu and L. Zheng, *Science*, 2016, **352**, 333-337.

31. X. Fan, S. Tan, J. Yang, Y. Liu, W. Bian, F. Liao, H. Lin and Y. Li, *ACS Energy Letters*, 2021, **7**, 343-348.

32. F. Wang, X. Xu, Y. Li, L. Gu, L. Li, H. Liu and H. Cong, *Applied Catalysis B: Environment and Energy*, 2025, **363**, 124838.

33. Y. Li, Z. Zhang, C. Li, Y. Zhou, X.-B. Chen, H. Lu, Z. Shi and S. Feng, *Applied Catalysis B: Environment and Energy*, 2024, **355**, 124116.

34. Y. Zhu, Q. Lin, Z. Hu, Y. Chen, Y. Yin, H. A. Tahini, H.-J. Lin, C.-T. Chen, X. Zhang, Z. Shao and H. Wang, *Small*, 2020, **16**, 2001204.

35. J. Tang, X. Xu, T. Tang, Y. Zhong and Z. Shao, *Small Methods*, 2022, **6**, 2201099.

36. J. Fan, X. Zhang, M. Han, X. Xiang, C. Guo, Y. Lin, N. Shi, D. Xu, Y. Lai and J. Bao, *Small*, 2024, **20**, 2303927.

37. F. Bartoli, L. Capozzoli, T. Peruzzolo, M. Marelli, C. Evangelisti, K. Bouzek, J. Hnát, G. Serrano, L. Poggini, K. Stojanovski, V. Briega-Martos, S. Cherevko, H. A. Miller and F. Vizza, *Journal of Materials Chemistry A*, 2023, **11**, 5789-5800.

38. L. Cai, H. Bai, C. W. Kao, K. Jiang, H. Pan, Y. R. Lu and Y. Tan, *Small*, 2024, **20**, e2311178.

39. B. Chen, A. L. G. Biancolli, C. L. Radford and S. Holdcroft, *ACS Energy Letters*, 2023, **8**, 2661-2667.

40. D. Chen, Y. S. Park, F. Liu, L. Fang and C. Duan, *Chemical Engineering Journal*, 2023, **452**.

41. K. C. Devarayapalli, J. Lee, S. Kang, S. Moon, S. V. P. Vattikuti, J. Lee and K. Lee, *Journal of Power Sources*, 2022, **527**.

42. L. Guo, X. Liu, Z. He, Z. Chen, Z. Zhang, L. Pan, Z.-F. Huang, X. Zhang, Y. Fang and J.-J. Zou, *ACS Sustainable Chemistry & Engineering*, 2022, **10**, 9956-9968.

43. W. Hooch Antink, S. Lee, H. S. Lee, H. Shin, T. Y. Yoo, W. Ko, J. Shim, G. Na, Y. E. Sung and T. Hyeon, *Advanced Functional Materials*, 2023, **34**.

44. B. J. Kim, X. Cheng, D. F. Abbott, E. Fabbri, F. Bozza, T. Graule, I. E. Castelli, L. Wiles, N. Danilovic, K. E. Ayers, N. Marzari and T. J. Schmidt, *Advanced Functional Materials*, 2018, **28**.

45. L. Li, Z. Zheng, J. Li, Y. Mu, Y. Wang, Z. Huang, Y. Xiao, H. Huang, S. Wang, G. Chen and L. Zeng, *Small*, 2023, **19**, e2301261.

46. X. Lin, X. Li, L. Shi, F. Ye, F. Liu and D. Liu, *Small*, 2024, **20**, e2308517.

47. H.-J. Liu, S. Zhang, R.-Y. Fan, B. Liu, R.-Q. Lv, Y.-M. Chai and B. Dong, *Applied Catalysis B: Environmental*, 2024, **343**.

48. H. J. Liu, S. Zhang, W. Y. Yang, N. Yu, C. Y. Liu, Y. M. Chai and B. Dong, *Advanced Functional Materials*, 2023, **33**.

49. M. Mekete Meshesha, D. Chanda, S. Gwon Jang and B. Lyong Yang, *Chemical Engineering Journal*, 2023, **474**.

50. T. H. Nguyen, P. K. L. Tran, D. T. Tran, V. A. Dinh, N. H. Kim and J. H. Lee, *Applied Catalysis B: Environmental*, 2024, **343**.

51. D. H. Park, M. H. Kim, H. J. Lee, W. J. Lee, J. H. Byeon, J. H. Kim, J. S. Jang and K. W. Park, *Advanced Materials Interfaces*, 2022, **9**.

52. J. E. Park, M.-J. Kim, M. S. Lim, S. Y. Kang, J. K. Kim, S.-H. Oh, M. Her, Y.-H. Cho and Y.-E. Sung, *Applied Catalysis B: Environmental*, 2018, **237**, 140-148.

53. Y. S. Park, J. H. Lee, M. J. Jang, J. Jeong, S. M. Park, W.-S. Choi, Y. Kim, J. Yang and S. M. Choi, *International Journal of Hydrogen Energy*, 2020, **45**, 36-45.

54. F. Razmjooei, T. Morawietz, E. Taghizadeh, E. Hadjixenophontos, L. Mues, M. Gerle, B. D. Wood, C. Harms, A. S. Gago, S. A. Ansar and K. A. Friedrich, *Joule*, 2021, **5**, 1776-1799.

55. L. Wan, Z. Xu, P. Wang, P.-F. Liu, Q. Xu and B. Wang, *Chemical Engineering Journal*, 2022, **431**.

56. F.-L. Wang, N. Xu, C.-J. Yu, J.-Y. Xie, B. Dong, X.-Y. Zhang, Y.-W. Dong, Y.-L. Zhou and Y.-M. Chai, *Applied Catalysis B: Environmental*, 2023, **330**.

57. Z. Wei, M. Guo and Q. Zhang, *Applied Catalysis B: Environmental*, 2023, **322**.

58. L. Xia, W. Jiang, H. Hartmann, J. Mayer, W. Lehnert and M. Shviro, *ACS Applied Materials & Interfaces*, 2022, **14**, 19397-19408.

59. H. Zhang, A. Chen, Z. Bi, X. Wang, X. Liu, Q. Kong, W. Zhang, L. Mai and G. Hu, *ACS Nano*, 2023, **17**, 24070-24079.

60. J. Zhao, J. Wang, X. Zheng, H. Wang, J. Zhang, J. Ding, X. Han, Y. Deng and W. Hu, *Small Methods*, 2023, **7**, e2201362.

61. H. Jia, H. Wang, F. Yan, Z. Li, R. Li, S. Li, J. Wang and H. Zhang, *Applied Catalysis B: Environment and Energy*, 2025, **364**, 124861.

62. X. Xiao, Y. Wei, S. Song, B. McElhenny, F. Zhang, X. Jiang, Y. Zhang, S. Chen, M. Wang, Y. Shen and Z. Ren, *Applied Catalysis B: Environment and Energy*, 2024, **349**, 123871.

63. T. T. N. Tran, T. A. Le, N. T. T. Dinh, N. D. Hai, T.-K. Truong, J. Yu, L. Peng, C. C. Nguyen and N. Q. Tran, *ACS Applied Materials & Interfaces*, 2024, **16**, 53675-53687.

64. S. Gupta, M. Forster, A. Yadav, A. J. Cowan, N. Patel and M. Patel, *ACS Applied Energy Materials*, 2020, **3**, 7619-7628.

65. P. Guo, D. Liu and R. Wu, *Small Structures*, 2023, **4**, 2300192.

66. R. Chen, S.-F. Hung, D. Zhou, J. Gao, C. Yang, H. Tao, H. B. Yang, L. Zhang, L. Zhang, Q. Xiong, H. M. Chen and B. Liu, *Advanced Materials*, 2019, **31**, 1903909.

67. B. Huang, J. Yan, Z. Li, L. Chen and J. Shi, *Angewandte Chemie International Edition*, 2024, **63**, e202409419.

68. D. Bao, L. Huang, Y. Gao, K. Davey, Y. Zheng and S.-Z. Qiao, *Journal of the American Chemical Society*, 2024, **146**, 34711-34719.

Chapter 4 Enhancing OER Performance through Nickel Substitution in Double Perovskite

4.1 Introduction

Hydrogen offers significant potential for decarbonizing future energy systems, owing to its zero-carbon emissions and high energy density [1, 2]. The electrolysis of water, which can be powered by renewable energies, is one of the most viable and effective methods for hydrogen production [3]. Currently, industrial water electrolysis relies on highly purified fresh water, yet freshwater resources are scarce and insufficient [4]. Replacing freshwater with seawater becomes increasingly appealing owing to its abundant and widespread reserves. Moreover, the electrical energy derived from diverse renewable sources such as solar, wind, and tidal energies can be directly integrated and utilized for seawater electrolysis systems [5]. However, significant progress is still required to launch the large-scale commercialization of seawater electrolysis. One of the formidable challenges for seawater electrolysis is the electrochemical competition between oxygen evolution reaction (OER) and chlorine electro-oxidation reaction (ClOR) on the anode side on account of their close thermodynamic equilibrium potentials [6, 7]. Besides, the products of ClOR, involving either Cl_2 or ClO^- depending on pH values, are highly toxic and corrosive, resulting in low efficiency and poor stability of the electrolysis system [8]. Dionigi *et al.* proposed a Pourbaix diagram in 2016 to illustrate the chloride and oxygen electrochemistry in relation to pH values. It is found that there is a wide potential difference window of ~480 mV for active OER while simultaneously suppressing ClOR at pH values larger than 7.5 [9]. Therefore, it is highly feasible to facilitate OER at a

potential lower than that required to trigger ClOR in alkaline electrolyte, which can be realized by the application of highly efficient electrocatalysts towards OER.

Among various catalysts, traditional inorganic perovskite oxides with tunable A and B sites provide an opportunity for establishing the relationship between the material's composition and electrochemical performance, stemming from the adjustable electronic structure of the B-site metal, lattice oxygen participation, and oxygen vacancies [10, 11]. In particular, defects and well-organized cation ordering of perovskite materials are anticipated to facilitate the rapid release of oxygen vacancies, hence enhancing the mobility of oxygen ions [12]. Double perovskites are a derivative of conventional perovskite oxides that expand the original framework to superlattices, often denoted as $AA'B'BO_{5+\delta}$. The A-site and/or B-site ordering distribution endows double perovskites with an enhanced oxygen-ion diffusion rate and surface exchange coefficient than the simple perovskites, thus the facilitated catalytic reaction [13]. Besides, the A-site and/or B-site cation ordering can induce a unique arrangement/electronic structure to the active TM elements, thereby exerting additional effects on the catalytic activity of the double perovskites [14]. For instance, Shao-Horn *et al.* have verified the efficiency of employing a series of double perovskites $LnBaCo_2O_{5+\delta}$ (Ln = Pr, Nd, Gd, and Gd) as OER electrocatalysts in alkaline condition [15]. These double perovskites exhibit exceptional OER activity and stability ascribed to their O-band centers, which are optimally positioned relative to the ab initio Fermi level, owing to the unique layered structure of these perovskites. Recently, Jun-Young *et al.* employed dual-doping strategy in $LnBaCo_2O_{5+\delta}$ double perovskite, which was substituting Ca in the Ba-site and incorporating Fe in the Co site to form $NdBa_{0.75}Ca_{0.25}Co_{1.5}Fe_{0.5}O_{5+\delta}$, as an efficient bi-functional oxygen electrocatalyst [16]. The B site cations with different oxidation states originated from the partially filled d or f orbitals was found to promote the movement of

electrons and oxygen-ions through oxygen vacancies, thus exhibiting exceptional oxygen electrocatalytic performance.

In this work, $NdBa_{0.75}Ca_{0.25}Co_{1.5}Fe_{0.5}O_{5+\delta}$ (donated as NBCCF) with partial substitution of Ni (denoted as NBCCFN) was synthesized by electrospinning method as highly active and durable oxygen evolution electrocatalyst for both freshwater and seawater electrolysis. The incorporation of Ni into the perovskite facilitates the in-situ formation of the electrocatalytically active oxyhydroxide species through surface re-construction during OER. In addition, the improved concentration of oxygen vacancies and the reduced reaction energy barrier induced by nickel incorporation are conducive to facilitating OER. As a result, the NBCCFN nanofibers could significantly promote OER while suppressing ClOR, achieving high activity, selectivity, and stability for water/seawater electrolysis.

4.2 Results and Discussion

The morphologies of the electrospun double perovskites were characterized by scanning electron microscope (SEM). The SEM images indicate that the electrospun perovskites display nanofibrous morphology with varying diameters interwoven into a scaffold structure (**Figure 4.1b** and **Figure 4.2a**). To investigate the phase structure of the as-spun perovskites, X-ray diffraction (XRD) was characterized. As shown in **Figure 4.1c**, the obtained XRD patterns reveal a singular phase with a characteristic perovskite structure, which can be indexed as a layered double perovskite (ICDD number: 00-053-0128). Rietveld refinements based on the XRD profiles were subsequently implemented to reveal the crystallographic details of the as-synthesized perovskites. The refinement results suggest that both the parental and the Ni-substituted perovskites can be assigned to a pure tetragonal structure with a space group of P4/mmm (**Figure 4.1d** and **Figure 4.2a**).

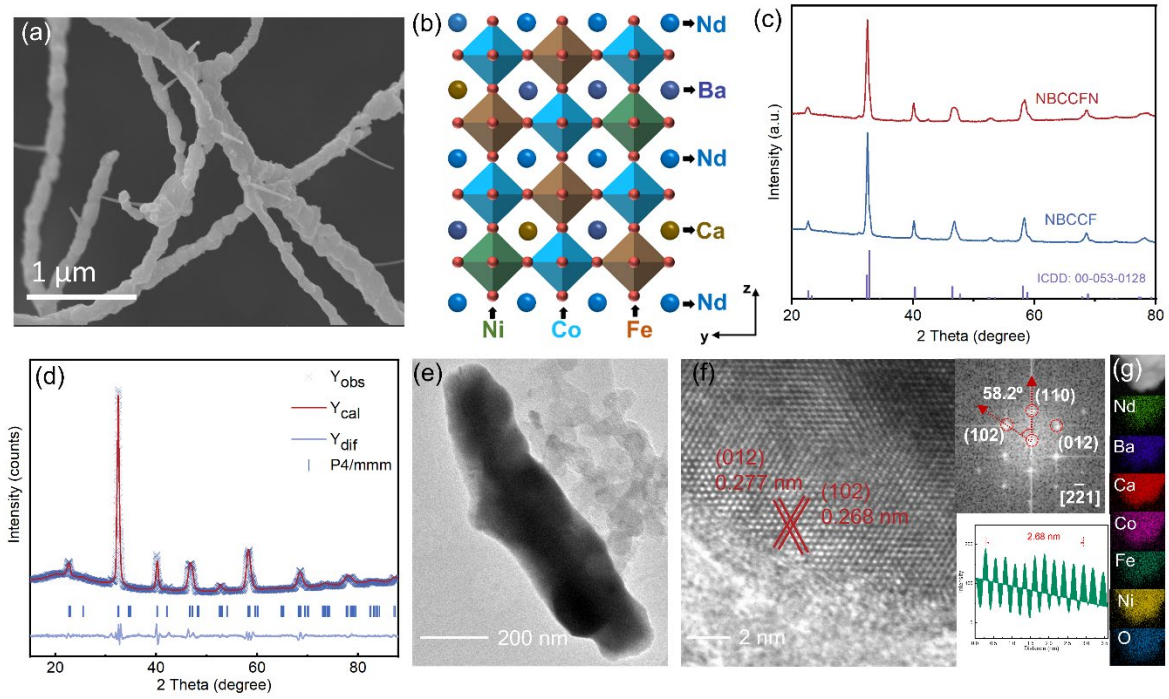

Figure 4.1 (a) SEM image and (b) schematic representation of the crystal structure for NBCCFN nanofibers. (c) XRD patterns of NBCCF and NBCCFN. (d) Refined XRD profiles of NBCCFN sample. (e) TEM, (f) HR-TEM (on the right is the corresponding FFT pattern along [2 -2 1] zone axis and the intensity profile of crystalline fringes), and (g) EDX element mapping images of NBCCFN.

Transmission electron microscope (TEM) images were also collected to unveil the detailed crystal structure of nanofibrous perovskites, which also reveal that the perovskites exhibit a nanosized morphology (**Figure 4.1e** and **Figure 4.2c**). The high-resolution TEM (HR-TEM) images (**Figure 4.1f** and **Figure 4.2d**) enlarged from the TEM images demonstrates clear lattice fringes with the d-spacing value of 0.277 nm and 0.268 nm, which can be assigned to the (012) and (102) planes of the tetragonal phase of NBCCF perovskites, respectively. The corresponding FFT pattern (inset in **Figure 4.1f**) additionally validates the tetragonal symmetry phase of NBCCFN, as evidenced by the intervals between (102), (110), and (012) planes, as well as the inclusive angle of ≈58.2°, consistent well with the lattice viewed along

[2 -2 1] zone axis and the XRD refinement results. **Figure 4.1g** displays the corresponding energy dispersive X-ray (EDX) elemental mappings, which suggests that the uniform distribution of all elements within NBCCFN, without any segregation.

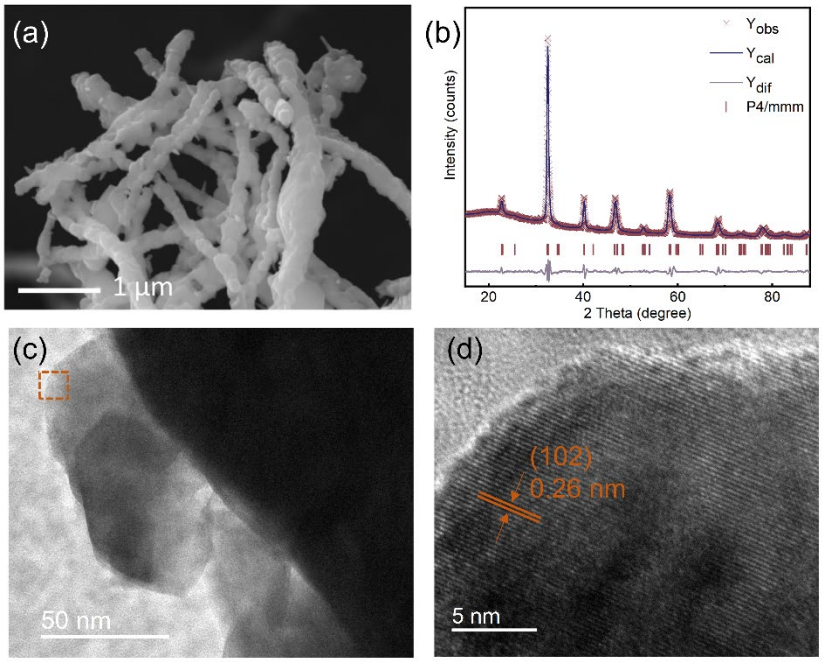

Figure 4.2 (a) SEM image, refined XRD profile, (c) TEM, and (d) HR-TEM images of NBCCF sample.

X-ray photoelectron spectroscopy (XPS) spectra were acquired to probe the surface chemistry of the metal elements within the perovskites. The Co 3p spectra were collected due to the partial overlap between Co 2p and Ba 3d spectra. A single peak, centered at approximately 61 eV, was observed for both samples, suggesting that the Co^{3+} ions are predominantly present in the perovskites (**Figure 4.3a**). The Fe 2p spectra suggests a shift toward a higher binding energy with the introduction of nickel, revealing an increased oxidation state of Fe species in the NBCCFN sample, as depicted in **Figure 4.3b**. XPS spectra of O 1s spectra for both samples can be deconvoluted into four components. The peaks at 528.48, 530, 531.28, and 532 eV can be assigned to the lattice oxygen O_L, highly

oxidative oxygen species O_2^{2-}/O^- (O_V), surface-adsorbed O_2 or hydroxyl groups (O_{ads}), and surface adsorbed water (O_{sur}), respectively (**Figure 4.3c**). The concentration of the O_2^{2-}/O^- species within the NBCCFN sample is notably higher than that of the NBCCF sample, indicating an increase in surface oxygen vacancies with the introduction of Ni doping.

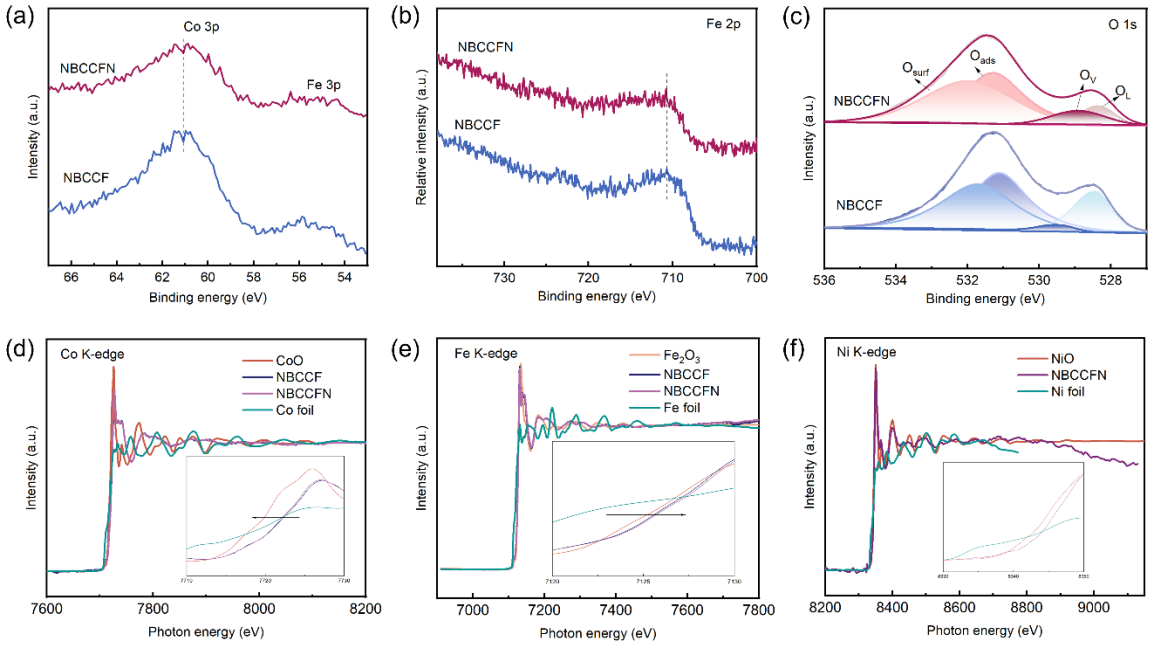

Figure 4.3 The XPS spectra of (a) Co 3p, (b) Fe 2p, and (c) O 1s for the prepared perovskite oxides. The (d) Co, (e) Fe, and (f) Ni K-edge XANES spectra of the perovskite oxides.

The K-edge X-ray absorption near-edge structure (XANES) spectra of Co, Fe, and Ni were measured to investigate the effects of Ni substitution. The Co K-edge XANES spectra exhibit a shift towards lower photon energy with increasing Ni content, indicating a reduction in the Co valence state (**Figure 4.3d**). Conversely, the Fe K-edge XANES spectra show a shift towards higher photon energy, suggesting an increase in the Fe valence state due to Ni doping (**Figure 4.3e**). Furthermore, a comparison of the Ni K-edge XANES spectra reveals that the Ni present in the NBCCFN matrix exists in an oxidation state higher than Ni^{2+} (**Figure 4.3f**). This observation highlights the complex interplay of oxidation states among the transition

metals in the system, providing insights into the electronic structure modifications induced by Ni substitution.

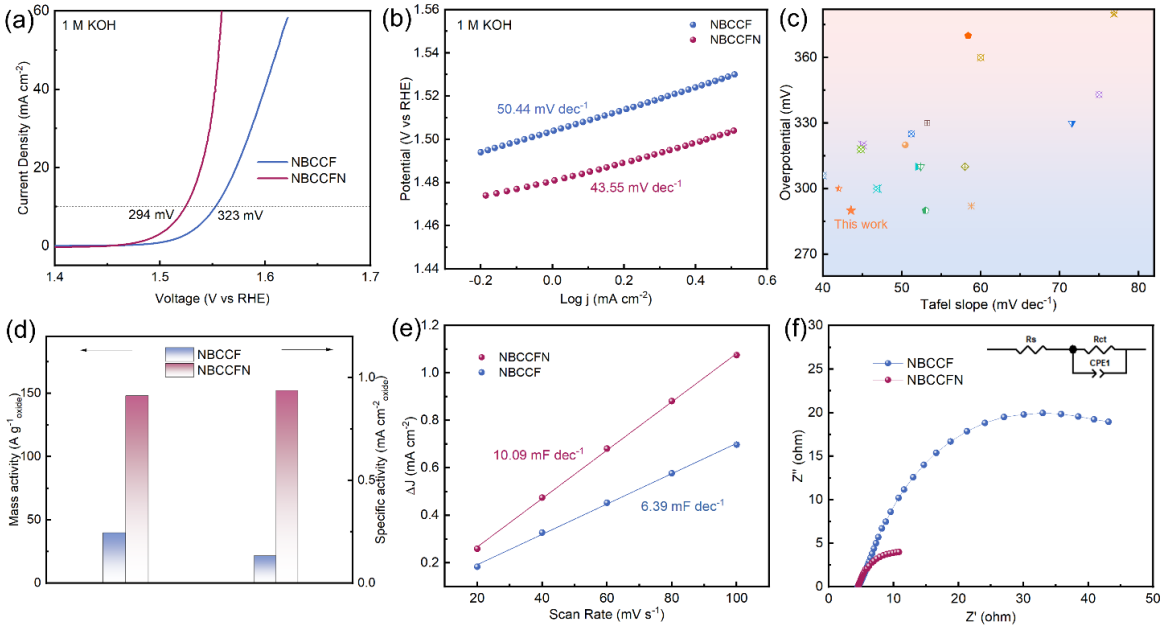

Figure 4.4 (a) LSV curves, (b) Tafel plots of NBCCF and NBCCFN samples. (c) Overpotential comparison of NBCCFN and other catalysts at 10 mA cm^{-2} [17-33]. (d) Mass activity and specific activity, (e) C_{dl} values, and (f) Nyquist plots (the inset is the equivalent circuit diagram) of NBCCF and NBCCFN samples.

The evaluation of electrocatalytic OER performance was first measured in 1 M KOH solution at room temperature using a typical three-electrode system. The linear sweep voltammetry (LSV) polarization curves in **Figure 4.4a** suggest that, to launch a current density of 10 mA cm^{-2}, only an overpotential of 294 mV is needed for NBCCFN, much lower than that of NBCCF (323 mV). It is found that the overpotential of NBCCFN is much lower than those of the perovskites and other advanced electrocatalysts (**Figure 4.4c**). To understand the catalytic kinetics of the as-prepared catalysts, Tafel slopes were extracted and calculated from LSV curves (**Figure 4.4b**). The Tafel slope of 43.55 mV dec^{-1} for NBCCFN is much smaller than

the pristine NBCCF (50.40 mV dec^{-1}), indicating its improved OER kinetics. **Figure 4.4d** highlights the superior mass activity and specific activity (based on the BET surface areas in **Figure 4.5a**, **b**) of NBCCFN compared to NBCCF. The electrochemically active surface area (ECSA) proportional to the number of active sites can identify the intrinsically catalytic activity of the catalysts, which can be reflected by the electrochemistry double-layer capacitance (C_{dl}) values. The C_{dl} values presented in **Figure 4.4e** were derived from the cyclic voltammetry (CV) curves with different scan rates (**Figure 4.5c**, **d**), which suggests that NBCCFN presents a much larger C_{dl} values (10.09 mF cm^{-2}) than the pristine perovskite (6.39 mF cm^{-2}). The radar map in **Figure 4.6** indicates that NBCCFN takes a much larger area in the map than NBCCF, indicating its superior OER performance.

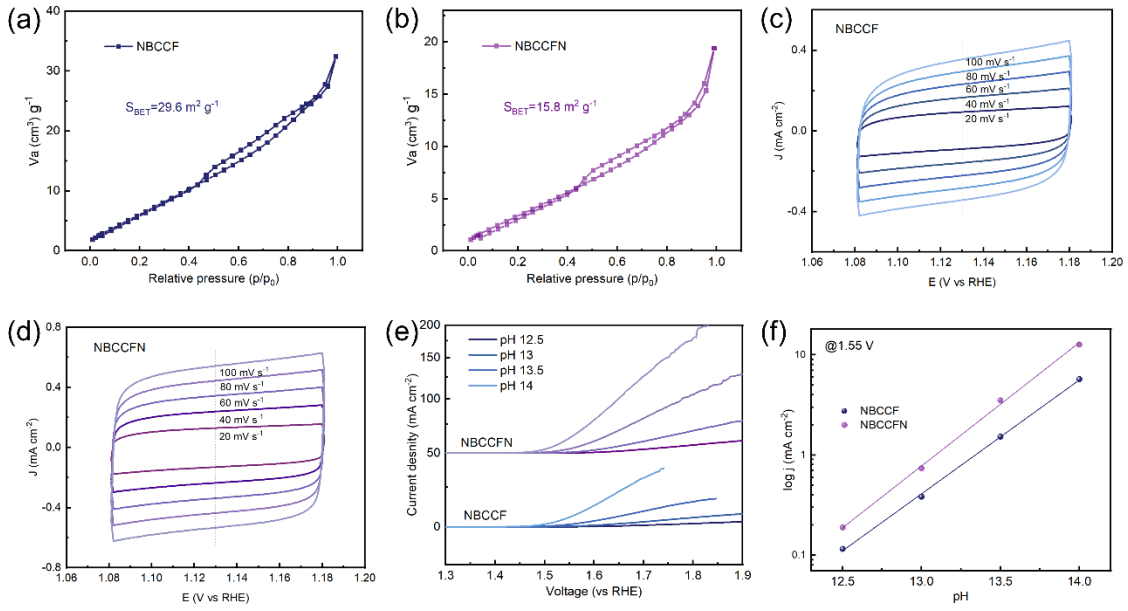

Figure 4.5 Nitrogen adsorption-desorption isotherm profiles of (a) NBCCF and (b) NBCCFN samples. CV curves of (c) NBCCF and (d) NBCCFN samples scanned from 20 to 100 mV s^{-1}. (e) OER activity under different pH values and (f) the corresponding pH-dependent activities.

The electrochemical impedance spectra (electrolyser) were obtained to evaluate the charge transfer resistance and the catalytic kinetics. As shown in **Figure 4.4f**, the charge transfer

resistance (R_{ct}) of the nickel doped perovskite is much smaller than the pristine one, demonstrating the superior charge-transfer kinetics of the doped catalysts. A robust pH-dependent activity is usually indicative of the lattice oxygen mechanism (LOM) during OER, as has been well confirmed by other investigations. The double perovskite's pH-dependent activity has been examined in order to investigate the underlying OER mechanism. Both catalysts exhibit an increase in activity as pH values rise from 12.5 to 14, as shown in **Figure 4.5e** and **f**. This suggests that the that the LOM mechanism may be involved throughout the OER process for both perovskites.

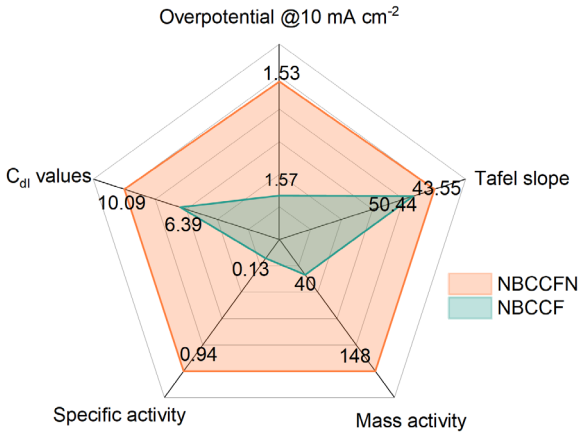

Figure 4.6 Radar map of catalytic activities for the perovskite nanofibers in 1 M KOH at room temperature.

The contact angle measurements of the perovskite catalyst coated on the glassy carbon electrode were conducted to investigate the interface ion/molecule interactions between the perovskite electrocatalysts and the aqueous electrolyte. As suggested in **Figure 4.7**, when the electrolyte was just dropped on the electrode, the contact angle of the NBCCF electrode is slightly smaller than that of the NBCCFN electrode. However, after standing steadily for 30 min, the NBCCFN electrode significantly reduced contact angle than the NBCCF electrode, indicating the improved surface wettability of the NBCCFN electrode, which could help to

assist the surface decoupled hydroxyl/water adsorption/dissociation and thus improve the OER kinetics.

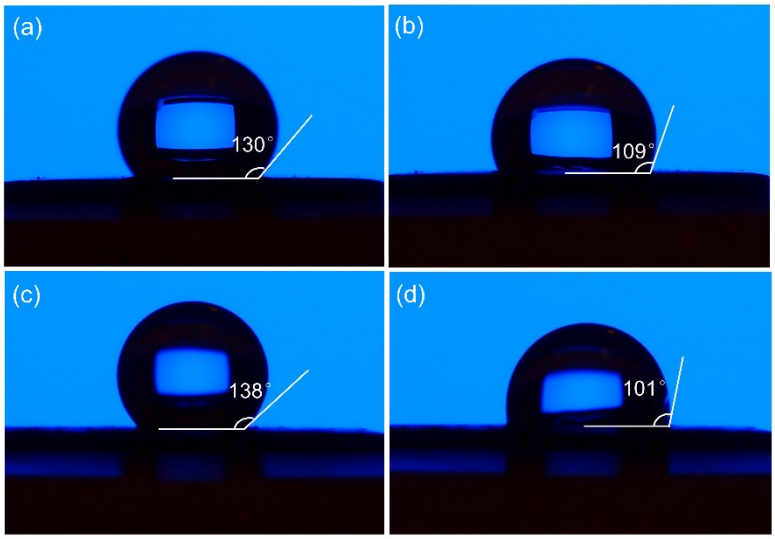

Figure 4.7 Contact angle measurements for water droplets were conducted on (a) NBCCF and (c) NBCCFN, and allowed to stand for 30 minutes for (b) NBCCF and (d) NBCCFN, with the catalysts coated on the glassy carbon electrode.

To evaluate the practical application potential of the prepared perovskite electrocatalysts and investigate their applicability to real-work conditions, anion exchange membrane water electrolyser (AEMWE) single cells were assembled and tested. Illustrated in **Figure 4.8a** is the configuration of the zero-gap AEMWE components. An AEMWE single cell mainly consists of an anode (Ni foam, serving as the catalyst support and gas diffusion layer) and a cathode (carbon paper, acting as catalyst (commercial Pt/C) support and gas diffusion layer) sandwiching an anion exchange membrane, referred to as the membrane electrode assembly (MEA). Bipolar plates are closely attached to the exterior of both electrodes. The assembled single cells were then subject to electrochemical measurement. Notably, the initial polarization curve of the NBCCFN-based cell exhibits a rather unsatisfactory activity, as shown in **Figure 4.8b**. After the activation process at a constant current density of 300 mA

cm^{-2} by the chronopotentiometry test, the activity enhanced tremendously. The activation process may stem from the Ni foam, as verified by the polarization curves of the AEMWE with empty Ni foam as anodic electrode (**Figure 4.9a**).

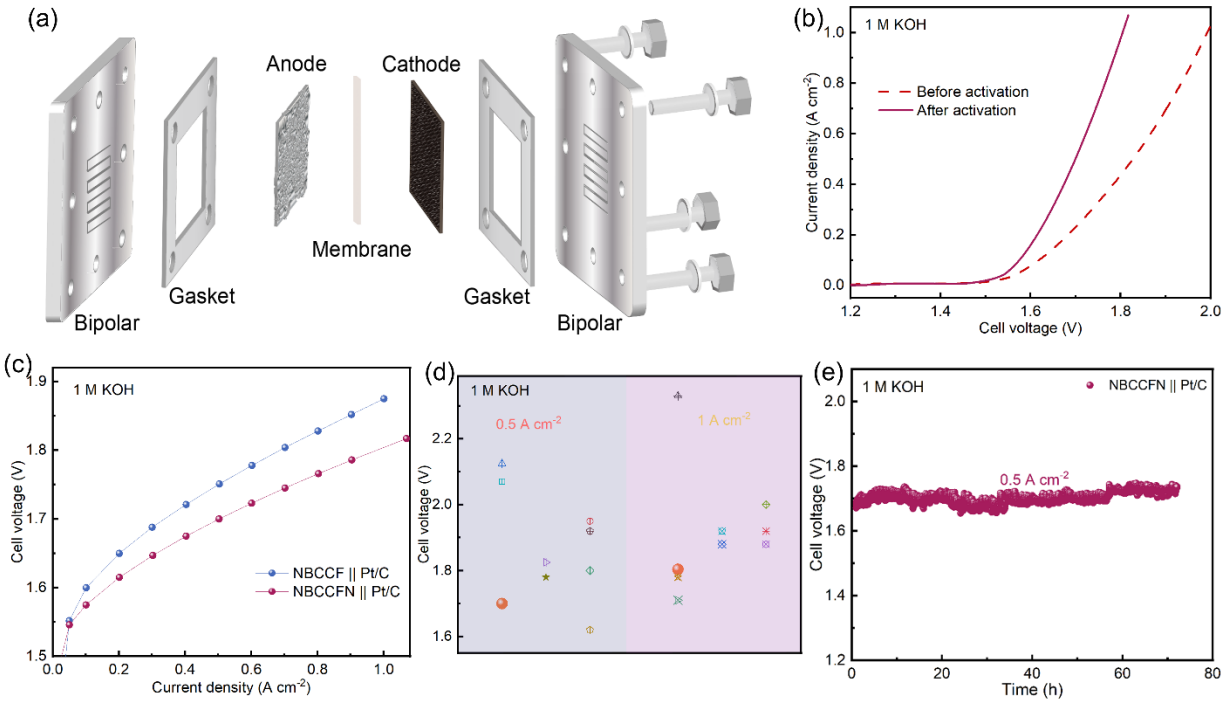

Figure 4.8 (a) Configuration of AEMWE single cell. (b) Polarization curves of the NBCCFN-based AEMWE before and after activation. (c) NBCCF- and NBCCFN-based single cell performances in 1 M KOH. (d) Performance comparison between NBCCFN based cell and other single cells [34-53]. (e) Long-term durability test of NBCCFN-based electrolyser.

Figure 4.8c suggests the polarization curves of the NBCCF- and NBCCFN-based AEMWE single cells after the activation process. The NBCCFN-based cell demonstrates the highest activity, requiring only a cell voltage of 1.70 and 1.805 V to achieve a current density of 0.5 and 1.0 A cm^{-2}, whereas the pristine NBCCF-based cell requires 1.751 and 1.875 V, respectively. Even comparing with other advanced electrolysers, the NBCCFN-based cell still suggests superior activities for both 0.5 and 1.0 A cm^{-2} (**Figure 4.8d**). In addition to its

remarkable activity, the NBCCFN-based AEMWE also demonstrates desirable durability even at a high current density, as evidenced by the nearly constant potential at 0.5 A cm^{-2} for more than 70 h (**Figure 4.8e**). The evaluation of AEMWE indicates that the NBCCFN is a promising electrocatalyst for the practical implementation of the overall water splitting process.

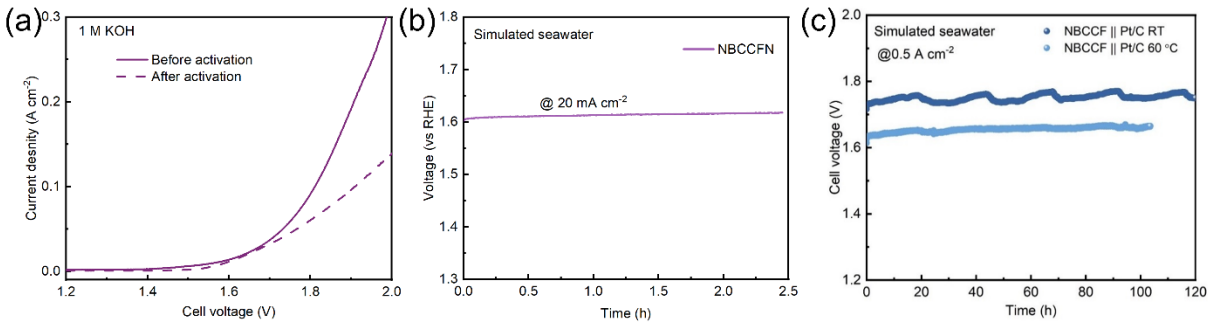

Figure 4.9 (a) Polarization curves of the AEMWE cell with unloaded Ni foam anode before and after activation. (b) Stability evaluation of NBCCFN sample in simulated seawater. (c) Long-term durability tests of the NBCCFN-based electrolyser in simulated seawater.

After confirming the favorable OER activity in alkaline freshwater electrolyte, the electrochemical performance of the as-prepared perovskite nanofibers was evaluated in alkaline simulated seawater (1.0 M KOH + 0.5 M NaCl) and alkaline natural seawater (1.0 M KOH + seawater). As shown in **Figure 4.10a**, the OER polarization curves of the as-prepared catalysts illustrate that NBCCFN shows a decreased overpotential of 348 mV at 10 mA cm^{-2} than pristine NBCCF (371 mV). Compared with in 1.0 M KOH, both samples suggest deteriorative OER performances in alkaline simulated seawater, which may originate from the increased corrosive chlorine ions. **Figure 4.9b** depicts the stability evaluation in alkaline simulated seawater at 20 mA cm^{-2}, with no noticeable potential degradation within 2.5 h. The performances of the AEMWE single cells with NBCCF and NBCCFN as anodic catalysts

were also evaluated in the simulated alkaline seawater. The polarization curves in **Figure 4.10b** indicate that aligning to alkaline freshwater solution, NBCCFN-based single cell outperforms the pristine cell. Under room temperature, the single cell with NBCCFN as anodic catalyst only necessitates a cell voltage of 1.68 and 1.82 V at 0.5 and 1.0 A cm^{-2}, respectively, whereas NBCCF-based cell requires 1.72 and 1.95 V to achieve equivalent current densities.

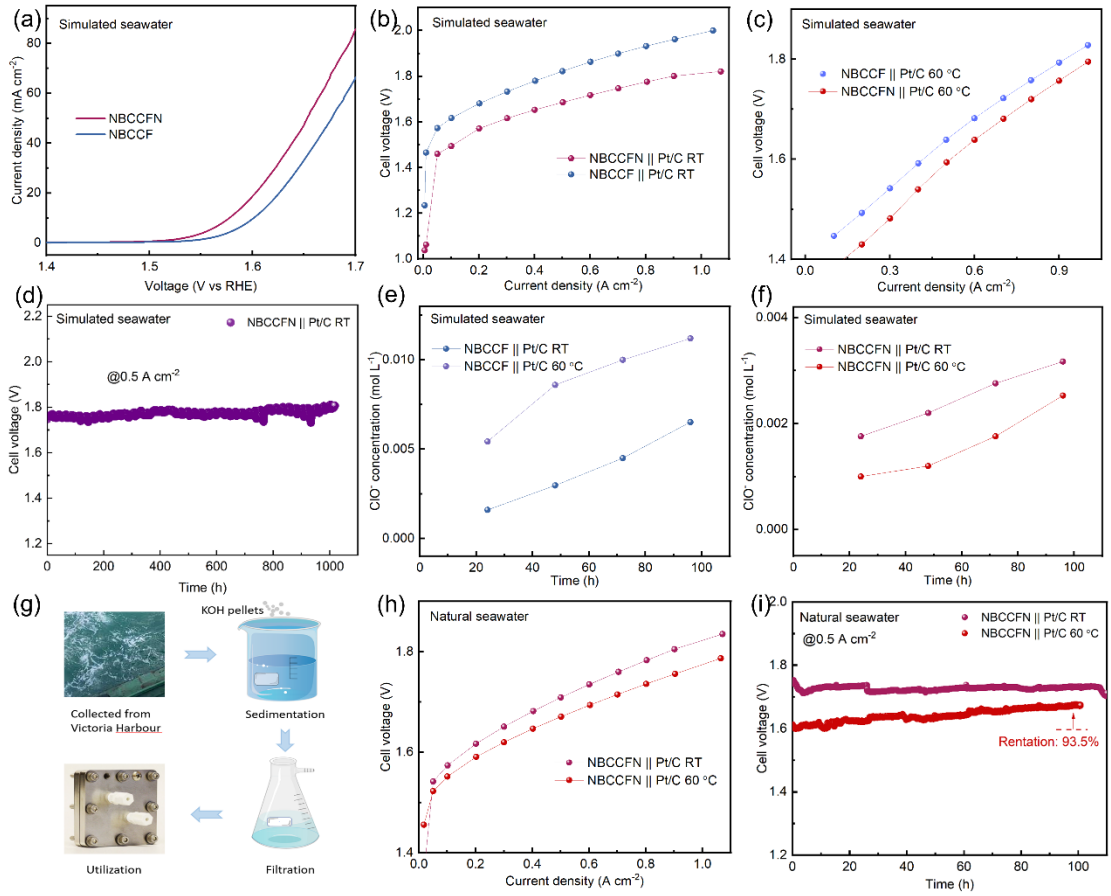

Figure 4.10 (a) Polarization curves in simulated seawater. NBCCF- and NBCCFN-based cell performance at (b) room temperature and (c) 60 °C. (d) Durability test of NBCCFN-based cell in simulated seawater. ClO^- generated in simulated seawater from the (e) NBCCF- and (f) NBCCFN-based electrolysers at 0.5 A cm^{-2}. (g) Natural seawater treatment process. (h) Polarization curves and (i) stability tests of NBCCFN-based electrolyser in natural seawater.

Even when the system temperature reached 60 ℃, the NBCCFN-based single cell continued to outperform the NBCCF-based single cell (**Figure 4.10c**). The stability tests in **Figure 4.10d** and **4.9c** show that both cells can stably operate at industrial current density in simulated seawater. Notably, the NBCCFN-based single cell suggests superior stability for more than 1000 h, without obvious degradation. To assess the capability of the prepared perovskite catalysts on suppressing ClOR, the produced ClO^- in alkaline simulated seawater by the NBCCF- and NBCCFN-based AEMWE electrolysers at the current density of 0.5 A cm^{-2} were measured by UV-vis. According to **Figure 4.10e** and **4.10f**, the ClO^- generated by the NBCCF-based electrolyser is much higher than that of the NBCCFN-based electrolyser, demonstrating its unfavorable effectiveness on suppressing ClOR compared with NBCCFN configuration. Due to the much-complexed components of real seawater, the natural seawater was alkalized and employed for electrocatalytic measurements. The natural seawater was directly acquired from Victoria Harbour, followed by a simple treatment. As shown in **Figure 4.10g**, The treatment process was that the KOH pellets were first added into the natural seawater so that the alkali concentration of seawater is ~1.0 M, which was then filtered to remove the sedimentary hydroxides (i.e., $Ca(OH)_2$, $Mg(OH)_2$, etc.) and other insoluble species within seawater. The filtered seawater was then utilized and fed into the AEMWE single cell. Shown in **Figure 4.10h** is the polarization curves of the NBCCFN-based cell fed with alkaline natural seawater at room temperature and 60 ℃. The single cell performance of NBCCFN-based cell shows comparable value in alkaline natural seawater (1.709 V at 0.5 A cm^{-2}). Improving the system temperature to 60 ℃, the single cell performance can be enhanced, requiring only 1.671 V to achieve 0.5 A cm^{-2}. Furthermore, the NBCCFN-based cell demonstrates remarkable stability in alkaline natural seawater at 0.5 A cm^{-2} for over 100 h at room temperature (**Figure 4.10i**). Even elevating the temperature to 60 ℃, the cell performance still maintains 93.5% in a harsher condition after 100 h operation. The

performance decline could be attributed to the incomplete removal of insoluble substances and metal cations from seawater, necessitating further research endeavor.

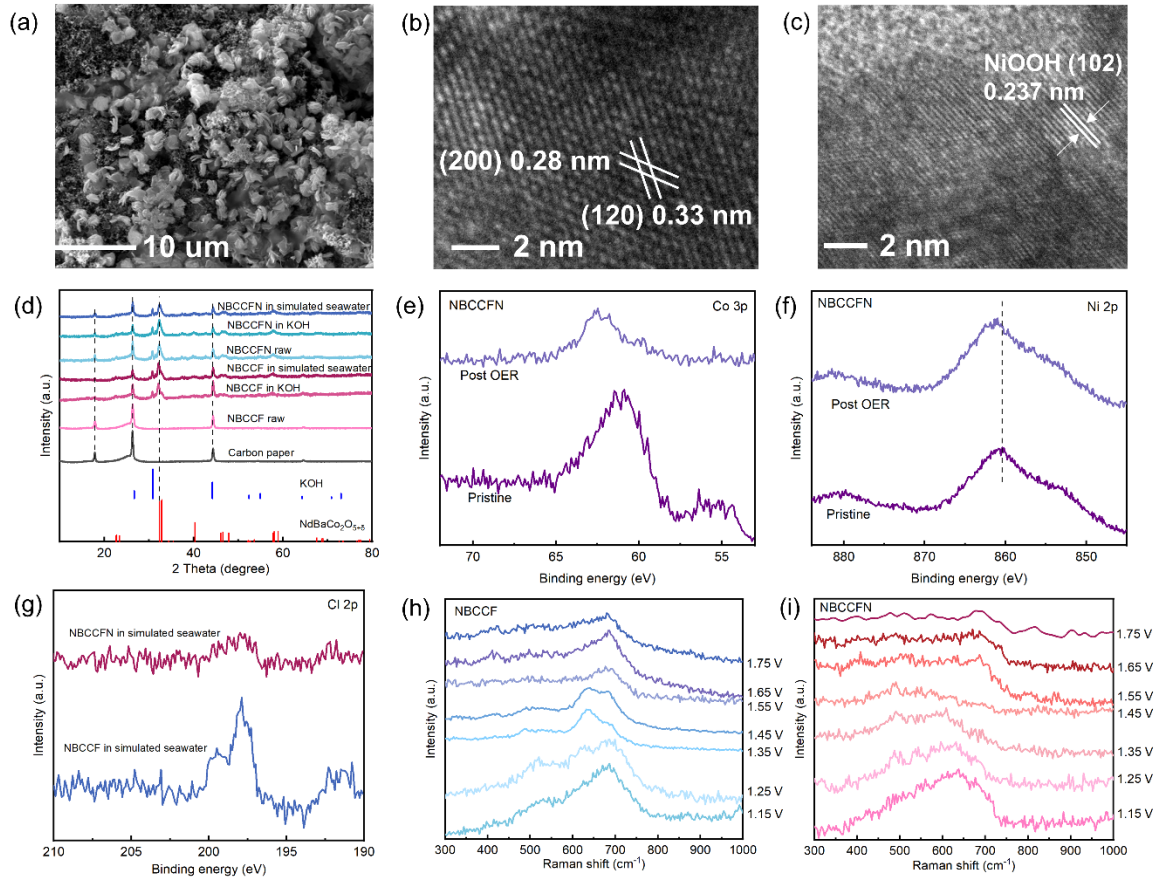

Figure 4.11 (a) SEM image and (b, c) HR-TEM images of the NBCCFN anode after stability test in alkaline electrolyte. (d) XRD patterns for the catalysts before and after test. XPS spectra of (e) Co 3p and (f) Ni 2p of NBCCFN samples after OER tests. (g) XPS spectra of Cl 2p after OER tests. The in-situ Raman spectra of (h) NBCCF and (i) NBCCFN catalysts under different applied voltages.

Given the extensive in situ surface reconstruction observed in OER catalysts, particularly in TM based oxide materials, a series of characterizations were conducted after stability tests to elucidate the structure-activity correlations of the perovskite catalysts. From the SEM image, the NBCCFN electrode after stability test reveals a much rougher surface compared to the

pristine sample (**Figure 4.11a**), featuring the emergence of nanosheets. The HR-TEM images further confirm the maintenance of the perovskite structure in the bulk, as evidenced by the distinct lattice fringes that can be attributed to the layered perovskite. Notably, a limited number of lattice fringes with an interplanar spacing of 0.237 nm attributed to the (102) plane of NiOOH have also been found on the catalyst's surface, indicating the in-situ formation of NiOOH during OER the process (**Figure 4.11b** and **c**). The XRD patterns of the catalyst before and after stability tests suggest no obvious change in perovskite structure (**Figure 4.11d**). XPS spectra of the catalysts coated on the carbon paper before and after OER tests under various conditions were collected. The Co 3p spectra of NBCCFN sample reveal that the catalyst exhibited increased intensity after the electrochemical tests, indicating the increased content of Co on the catalyst surface (**Figure 4.11e**), whereas no significant change was observed for the undoped sample (**Figure 4.12a**). The XPS spectra of Fe 2p peaks for both samples (**Figure 4.12b**, **c**) show no obvious shift. For the Ni 2p spectra of NBCCFN (**Figure 4.11f**), the peaks after electrochemical tests suggest obvious shift to higher binding energies, which is an indicative of the generation of Ni^{3+} in NiOOH, in consistent with previous reports [54]. To further compare the chlorine resistance on the surface of the prepared perovskites, Cl 2p spectra were also detected. As indicated in **Figure 4.11g**, the NBCCF sample exhibits a distinct Cl 2p peak, while the NBCCFN sample presents a discernible signal, indicating the negligible adsorption of chlorine on the surface of the NBCCFN sample after the electrochemical test, thus demonstrating its high selectivity for OER.

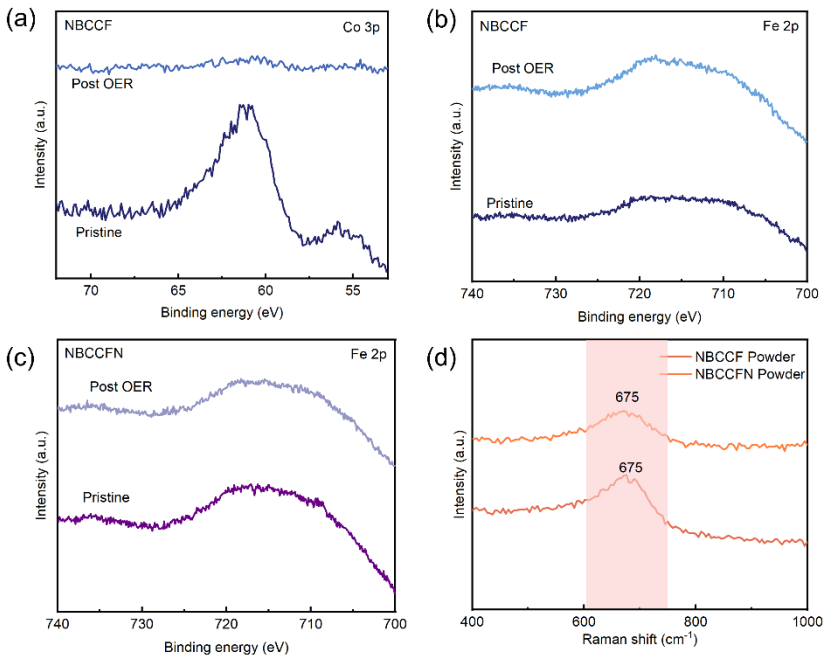

Figure 4.12 Comparison of the XPS spectra before and after stability tests for (a) Co 3p for NBCCF, (b) Fe 2p for NBCCF, and (c) Fe 2p for NBCCFN. (d) Ramna spectra of the NBCCF and NBCCFN perovskite powders.

In-situ Raman characterizations were further conducted to elucidate the real-time evolution of the perovskite catalysts during the OER process. For comparison, the Raman spectra of the powdered catalysts were also obtained and shown in **Figure 4.12d**, which both show a broad peak centering at 675 cm^{-1}. Compared to the powdered spectra, the catalysts coated on glassy carbon electrode and immersed into the electrolyte solution suggest different spectra. This is due to the distinct behavior of water molecules at the interface, which differs significantly from their behavior in the liquid phase. In the context of water electrocatalysis, the specific structure of water at the charged electrode interface, including its orientation and hydrogen-bonding network, will have a substantial impact on the reaction mechanism and activity [55]. For the in-situ Raman of the catalyst at 1.15 V (**Figure 4.11h**), only the intensity of NBCCF changed compared with the original catalyst. The intensity of the peak of NBCCFN changed

and blue-shifted, which was mainly attributed to the surface strain caused by the reorientation of atoms after immersion in KOH solution (**Figure 4.11i**). For the NBCCF sample, at 1.15 V, there are three peaks, namely the highest peak of 424 cm^{-1}, 686 cm^{-1}, and the peaks of 518 cm^{-1} and 628 cm^{-1}. The peak at 686 cm^{-1} belongs to the Co-O bending and stretching vibrations [56]. As the voltage gradually increases, the peak intensity gradually decreases and blue shifts. Interestingly, the peak at 628 cm^{-1} belongs to β-CoOOH stretching [57]. As the voltage increases from 1.15 V to 1.45 V, the peak intensity gradually increases and red shifts. At 1.45 V, the peak intensity even exceeded the main peak at 628 cm^{-1}, and the peak position red-shifted to 633 cm^{-1}. At 1.55 V, this peak suddenly disappeared, and did not reappear at higher potentials, indicating that the catalyst surface was reconstructed. The peak at 518 cm^{-1} belongs to the Co-O bands of α-$Co(OH)_2$, suggesting gradual red shift to 509 cm^{-1} and gradually decreasing in intensity as the potential increased [58]. At 1.45 V, a new peak emerges at 424 cm^{-1}, which can be assigned to the bending modes of M-O bonds in oxides [59, 60]. Nonetheless, no FeOOH signals can be observed within the in-situ Raman spectra of the NBCCF sample. This may be attributed to the relatively lower abundance of FeOOH species on the reconstructed surface compared to other species, as well as the overlapping of the characteristic FeOOH peaks (526 and 700 cm^{-1}) with other Raman peaks [61, 62]. The NBCCFN sample with the introduction of Ni exhibits notably distinct spectra compared to the pristine sample. At 1.15 V (vs. RHE), a series of peaks emerges within the 500-750 cm^{-1} range. The prominent peak at approximately 494 cm^{-1} is indicative of disordered $Ni(OH)_2$, which exhibits an increase in peak intensity and becomes the most prominent peak at 1.95 V, signifying the activation of NiOOH in the reaction [63]. This is consistent with the experimental results. The peak intensity diminishes at 1.55-1.75 V, potentially due to bubble coverage. The band at around 612 cm^{-1}, attributed to CoOOH, gradually diminishes until 1.45 V [64]. The Raman band at 638 cm^{-1} corresponds to the Co-OH vibrational mode in α-

$Co(OH)_2$, which undergoes a red shift to 621 cm^{-1} as the voltages increase [65]. The peak at 676 cm^{-1} corresponds to the stretching vibration mode of Ni-O [66]. The signal at 690 cm^{-1} indicates the presence of the FeOOH band, with the intensity increasing as the applied voltages rise [67]. The in-situ Raman spectra indicate that the reconstructed CoOOH serves as the active sites for the NBCCF sample, while the in-situ generation of the NiOOH species facilitated by the Ni substitution and the enhanced generation of CoOOH together boost the OER for the NBCCFN specimen.

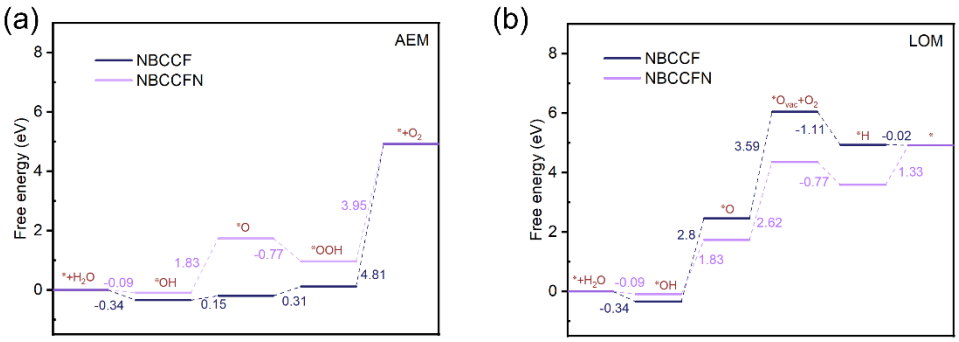

Figure 4.13 Gibbs free energy profiles of (a) AEM mechanism and (b) LOM mechanism for the OER pathway on NBCCF and NBCCFN.

DFT calculation was conducted to determine the OER mechanism of the prepared double perovskite nanofibers, involving adsorbate evolution mechanism (AEM) and lattice oxygen oxidation mechanism (LOM), as shown in **Figure 4.13**. In AEM mechanism, the deprotonation process of *OOH serves as the potential determining step (PDS) for both samples, with the largest free energy barrier (ΔG) of 4.81 eV for NBCCF and 3.95 eV for NBCCFN sample (**Figure 4.13a**). While in the LOM mechanism, the step from *O to $*O_{vac+O2}$ is found to be the PDS, with the largest ΔG value of 3.59 eV for NBCCF and 2.62 eV for NBCCFN sample (**Figure 4.13b**). It can be found that AEM exhibits a higher ΔG

value than LOM in PDS, implying that both perovskites prefer to follow the LOM pathway during OER, which is consistent with their strong pH-dependent activities.

4.3 Conclusion

A nickel substituted double perovskite was synthesized by electrospinning method and employed as OER catalysts for seawater/seawater electrolysis. The in-situ formed metal oxyhydroxides on the perovskite surface have been recognized as truly active sites. The incorporation of Ni facilitates the intrinsic activity for OER by increasing oxygen vacancies, facilitating reaction intermediate formation, and decreasing reaction energy barrier. Notably, the NBCCFN nanofibers achieves stable operation in seawater for over 1000 h at an industrial current density. This work demonstrates the significant potential of the double perovskite nanofibers as active, selective, and durable electrocatalysts for freshwater and seawater electrolysis.

4.4 References

1. L. Schlapbach and A. Züttel, *nature*, 2001, **414**, 353-358.
2. S. Dunn, *International journal of hydrogen energy*, 2002, **27**, 235-264.
3. J. Chi and H. Yu, *Chinese Journal of Catalysis*, 2018, **39**, 390-394.
4. P. Kumar, A. Date, N. Mahmood, R. K. Das and B. Shabani, *International Journal of Hydrogen Energy*, 2024, **78**, 202-217.
5. S. Loomba, M. W. Khan and N. Mahmood, *ChemElectroChem*, 2023, **10**, e202300471.
6. L. Chen, C. Yu, J. Dong, Y. Han, H. Huang, W. Li, Y. Zhang, X. Tan and J. Qiu, *Chemical Society Reviews*, 2024.
7. Z. Yu and L. Liu, *Advanced Materials*, 2024, **36**, 2308647.

8. W. He, X. Li, C. Tang, S. Zhou, X. Lu, W. Li, X. Li, X. Zeng, P. Dong and Y. Zhang, *Acs Nano*, 2023, **17**, 22227-22239.

9. F. Dionigi, T. Reier, Z. Pawolek, M. Gliech and P. Strasser, *ChemSusChem*, 2016, **9**, 962-972.

10. Q. Ji, L. Bi, J. Zhang, H. Cao and X. S. Zhao, *Energy & Environmental Science*, 2020, **13**, 1408-1428.

11. Y. Liu, H. Huang, L. Xue, J. Sun, X. Wang, P. Xiong and J. Zhu, *Nanoscale*, 2021, **13**, 19840-19856.

12. S. Royer, D. Duprez, F. Can, X. Courtois, C. Batiot-Dupeyrat, S. Laassiri and H. Alamdari, *Chemical reviews*, 2014, **114**, 10292-10368.

13. W. Zhou, J. Sunarso, Z.-G. Chen, L. Ge, J. Motuzas, J. Zou, G. Wang, A. Julbe and Z. Zhu, *Energy & Environmental Science*, 2011, **4**, 872-875.

14. H. Sun, X. Xu, Z. Hu, L. H. Tjeng, J. Zhao, Q. Zhang, H.-J. Lin, C.-T. Chen, T.-S. Chan and W. Zhou, *Journal of Materials Chemistry A*, 2019, **7**, 9924-9932.

15. A. Grimaud, K. J. May, C. E. Carlton, Y.-L. Lee, M. Risch, W. T. Hong, J. Zhou and Y. Shao-Horn, *Nature communications*, 2013, **4**, 2439.

16. N.-I. Kim, S.-H. Cho, S. H. Park, Y. J. Lee, R. A. Afzal, J. Yoo, Y.-S. Seo, Y. J. Lee and J.-Y. Park, *Journal of Materials Chemistry A*, 2018, **6**, 17807-17818.

17. H. Arandiyan, S. S. Mofarah, Y. Wang, C. Cazorla, D. Jampaiah, M. Garbrecht, K. Wilson, A. F. Lee, C. Zhao and T. Maschmeyer, *Chemistry*, 2021, **27**, 14418-14426.

18. H. Chen, L. Shi, K. Sun, K. Zhang, Q. Liu, J. Ge, X. Liang, B. Tian, Y. Huang, Z. Shi, Z. Wang, W. Zhang, M. Liu and X. Zou, *ACS Catalysis*, 2022, **12**, 8658-8666.

19. X. Du, H. Ai, M. Chen, D. Liu, S. Chen, X. Wang, K. H. Lo and H. Pan, *Applied Catalysis B: Environmental*, 2020, **272**.

20. Y. Fang, Y. Fang, R. Zong, Z. Yu, Y. Tao and J. Shao, *Journal of Materials Chemistry A*, 2022, **10**, 1369-1379.

21. S. Guddehalli Chandrappa, P. Moni, D. Chen, G. Karkera, K. R. Prakasha, R. A. Caruso and A. S. Prakash, *ACS Applied Energy Materials*, 2021, **4**, 13425-13430.

22. Y. Liu, C. Ye, S.-N. Zhao, Y. Wu, C. Liu, J. Huang, L. Xue, J. Sun, W. Zhang, X. Wang, P. Xiong and J. Zhu, *Nano Energy*, 2022, **99**.

23. T. X. Nguyen, Y. C. Liao, C. C. Lin, Y. H. Su and J. M. Ting, *Advanced Functional Materials*, 2021, **31**.

24. S. Rao Ede, C. N. Collins, C. D. Posada, G. George, H. Wu, W. D. Ratcliff, Y. Lin, J. Wen, S. Han and Z. Luo, *ACS Catal*, 2021, **11**.

25. Y. Sun, Z. Zhao, S. Wu, W. Li, B. Wu, G. Liu, G. Chen, B. Xu, B. Kang, Y. Li and C. Li, *ChemSusChem*, 2020, **13**, 2671-2676.

26. L. Tang, Z. Chen, F. Zuo, B. Hua, H. Zhou, M. Li, J. Li and Y. Sun, *Chemical Engineering Journal*, 2020, **401**.

27. L. Tang, T. Fan, Z. Chen, J. Tian, H. Guo, M. Peng, F. Zuo, X. Fu, M. Li, Y. Bu, Y. Luo, J. Li and Y. Sun, *Chemical Engineering Journal*, 2021, **417**.

28. L. Tang, Y. Yang, H. Guo, Y. Wang, M. Wang, Z. Liu, G. Yang, X. Fu, Y. Luo, C. Jiang, Y. Zhao, Z. Shao and Y. Sun, *Advanced Functional Materials*, 2022, **32**.

29. X. Wang, J. Dai, C. Zhou, D. Guan, X. Wu, W. Zhou and Z. Shao, *ACS Materials Letters*, 2021, **3**, 1258-1265.

30. J. Yu, X. Wu, D. Guan, Z. Hu, S.-C. Weng, H. Sun, Y. Song, R. Ran, W. Zhou, M. Ni and Z. Shao, *Chemistry of Materials*, 2020, **32**, 4509-4517.

31. N. Yu, Y. Ma, J.-K. Ren, Z.-J. Zhang, H.-J. Liu, J. Nan, Y.-C. Li, Y.-M. Chai and B. Dong, *Chemical Engineering Journal*, 2023, **478**.

32. J. Zhang, Y. Ye, B. Wei, F. Hu, L. Sui, H. Xiao, L. Gui, J. Sun, B. He and L. Zhao, *Applied Catalysis B: Environmental*, 2023, **330**.

33. J.-W. Zhao, H. Zhang, C.-F. Li, X. Zhou, J.-Q. Wu, F. Zeng, J. Zhang and G.-R. Li, *Energy & Environmental Science*, 2022, **15**, 3912-3922.

34. D. S. Baek, K. A. Lee, J. Park, J. H. Kim, J. Lee, J. S. Lim, S. Y. Lee, T. J. Shin, H. Y. Jeong, J. S. Son, S. J. Kang, J. Y. Kim and S. H. Joo, *Angew Chem Int Ed Engl*, 2021, **60**, 1441-1449.

35. J. Chang, Q. Lv, G. Li, J. Ge, C. Liu and W. Xing, *Applied Catalysis B: Environmental*, 2017, **204**, 486-496.

36. L. Guo, X. Liu, Z. He, Z. Chen, Z. Zhang, L. Pan, Z.-F. Huang, X. Zhang, Y. Fang and J.-J. Zou, *ACS Sustainable Chemistry & Engineering*, 2022, **10**, 9956-9968.

37. W. Hooch Antink, S. Lee, H. S. Lee, H. Shin, T. Y. Yoo, W. Ko, J. Shim, G. Na, Y. E. Sung and T. Hyeon, *Advanced Functional Materials*, 2023, **34**.

38. M. J. Jang, J. Yang, J. Lee, Y. S. Park, J. Jeong, S. M. Park, J.-Y. Jeong, Y. Yin, M.-H. Seo, S. M. Choi and K. H. Lee, *Journal of Materials Chemistry A*, 2020, **8**, 4290-4299.

39. B. J. Kim, X. Cheng, D. F. Abbott, E. Fabbri, F. Bozza, T. Graule, I. E. Castelli, L. Wiles, N. Danilovic, K. E. Ayers, N. Marzari and T. J. Schmidt, *Advanced Functional Materials*, 2018, **28**.

40. L. Li, G. Zhang, B. Wang and S. Yang, *Applied Catalysis B: Environmental*, 2022, **302**.

41. L. Li, Z. Zheng, J. Li, Y. Mu, Y. Wang, Z. Huang, Y. Xiao, H. Huang, S. Wang, G. Chen and L. Zeng, *Small*, 2023, **19**, e2301261.

42. H. Liao, G. Ni, P. Tan, Y. Liu, K. Chen, G. Wang, M. Liu and J. Pan, *Applied Catalysis B: Environmental*, 2022, **317**.

43. H.-J. Liu, R.-N. Luan, L.-Y. Li, R.-Q. Lv, Y.-M. Chai and B. Dong, *Chemical Engineering Journal*, 2023, **461**.

44. H. J. Liu, S. Zhang, W. Y. Yang, N. Yu, C. Y. Liu, Y. M. Chai and B. Dong, *Advanced Functional Materials*, 2023, **33**.

45. H. J. Liu, S. Zhang, Y. N. Zhou, W. L. Yu, Y. Ma, S. T. Wang, Y. M. Chai and B. Dong, *Small*, 2023, **19**, e2301255.

46. Q. P. Ngo, T. T. Nguyen, Q. T. T. Le, J. H. Lee and N. H. Kim, *Advanced Energy Materials*, 2023, **13**.

47. W. Ning, R. Wang, X. Li, M. H. Wang, H. G. Xu, H. Y. Lin, X. P. Fu, M. Wang, P. F. Liu and H. G. Yang, *Chem Commun (Camb)*, 2023, **59**, 11803-11806.

48. F. Razmjooei, A. Farooqui, R. Reissner, A. S. Gago, S. A. Ansar and K. A. Friedrich, *ChemElectroChem*, 2020, **7**, 3951-3960.

49. P. Thangavel, H. Lee, T. H. Kong, S. Kwon, A. Tayyebi, J. h. Lee, S. M. Choi and Y. Kwon, *Advanced Energy Materials*, 2022, **13**.

50. F.-L. Wang, Y.-W. Dong, C.-J. Yu, B. Dong, X.-Y. Zhang, R.-Y. Fan, J.-Y. Xie, Y.-N. Zhou and Y.-M. Chai, *Applied Catalysis B: Environmental*, 2023, **331**.

51. F.-L. Wang, N. Xu, C.-J. Yu, J.-Y. Xie, B. Dong, X.-Y. Zhang, Y.-W. Dong, Y.-L. Zhou and Y.-M. Chai, *Applied Catalysis B: Environmental*, 2023, **330**.

52. Z. Xu, L. Wan, Y. Liao, P. Wang, K. Liu and B. Wang, *Journal of Materials Chemistry A*, 2021, **9**, 23485-23496.

53. T. Zhao, S. Wang, C. Jia, C. Rong, Z. Su, K. Dastafkan, Q. Zhang and C. Zhao, *Small*, 2023, **19**, e2208076.

54. H. Zhang, S. Geng, M. Ouyang, H. Yadegari, F. Xie and D. J. Riley, *Advanced Science*, 2022, **9**, 2200146.

55. Y. Xie, Y. Sun, H. Tao, X. Wang, J. Wu, K. Ma, L. Wang, Z. Kang and Y. Zhang, *Advanced Functional Materials*, 2022, **32**, 2111777.

56. L. Ge, W. Lai, Y. Deng, J. Bao, B. Ouyang and H. Li, *Inorganic Chemistry*, 2022, **61**, 2619-2627.

57. X. Cai, F. Peng, X. Luo, X. Ye, J. Zhou, X. Lang and M. Shi, *ChemSusChem*, 2021, **14**, 3163-3173.

58. C. Jing, T. Yuan, L. Li, J. Li, Z. Qian, J. Zhou, Y. Wang, S. Xi, N. Zhang and H.-J. Lin, *ACS Catalysis*, 2022, **12**, 10276-10284.

59. H. Cheraparambil, M. Vega-Paredes, C. Scheu and C. Weidenthaler, *ACS Applied Materials & Interfaces*, 2024, **16**, 21997-22006.

60. G. M. Kumar, P. Ilanchezhiyan, C. Siva, A. Madhankumar, T. Kang and D. Kim, *International Journal of Hydrogen Energy*, 2020, **45**, 391-400.

61. L. V. Lima, M. Rodriguez, V. A. Freitas, T. E. Souza, A. E. Machado, A. O. Patrocínio, J. D. Fabris, L. C. Oliveira and M. C. Pereira, *Applied Catalysis B: Environmental*, 2015, **165**, 579-588.

62. Y. Wu, Z. Xie, Y. Li, Z. Lv, L. Xu and B. Wei, *International Journal of Hydrogen Energy*, 2021, **46**, 25070-25080.

63. K. S. Joya and X. Sala, *Physical Chemistry Chemical Physics*, 2015, **17**, 21094-21103.

64. J. Liu, Q. Hu, Y. Wang, Z. Yang, X. Fan, L.-M. Liu and L. Guo, *Proceedings of the National Academy of Sciences*, 2020, **117**, 21906-21913.

65. K. Wang, Y. Li, J. Hu, Z. Lu, J. Xie, A. Hao and Y. Cao, *Chemical Engineering Journal*, 2022, **447**, 137540.

66. S. Zhou, S. Lv, J. Shi, L. Zhang, J. Li and W. Cai, *Chemical Engineering Journal*, 2024, **484**, 149706.

67. Z. Qiu, Y. Ma and T. Edvinsson, *Nano Energy*, 2019, **66**, 104118.

Chapter 5 Complete Reconstruction of Cobalt Metaphosphate for Highly Efficient and Selective OER

5.1 Introduction

The pursuit of sustainable and renewable energy sources has emerged as a critical global imperative, driven by the urgent need to mitigate climate change and reduce dependence on fossil fuels [1]. Hydrogen produced through water electrolysis offers zero carbon emissions and generates no undesirable byproducts, making it a reliable energy solution, especially when powered by renewable energy sources such as wind, solar, and wave energy [2]. Generally, water electrolysis involves a cathodic reaction for hydrogen generation and an anodic reaction for oxygen production. The anodic oxygen evolution reaction (OER), which is a complex four-electron transfer process, has been regarded as the bottleneck for water electrolysis [3]. Therefore, the development of highly efficient catalysts is of paramount importance for accelerating OER kinetics and improving the efficiency of water electrolysis. Recently, using seawater for electrolysis has gained significant attention due to the abundant reserves of seawater and depleting freshwater resources [4]. However, the high concentration of chloride ions in seawater can induce the electrochemical chlorine oxidation reaction (ClOR), which competes with the anodic OER and generates harmful products [5]. While according to previous studies, there exists a substantial thermodynamic standard potential difference of ~480 mV between OER and ClOR under alkaline conditions, which implies that regulating the overpotential of OER within this range could effectively hinder the onset of ClOR, further highlighting the importance for developing highly active electrocatalysts [6].

Typically, most transition metal-based OER electrocatalysts would experience a dynamic and irreversible self-reconstruction process on their surfaces under the alkaline anodic conditions, generating the corresponding (oxy)hydroxides species, which have been extensively regarded as the actual active substances for alkaline OER [7]. The in-situ generated transitional metal (oxy)hydroxides could reveal improved electrocatalytic activity compared to the directly synthesized counterparts, which is mainly attributed to the increase in surface area, abundant edge active sites, and the formation of oxygen vacancies. [7]. Consequently, considerable efforts have been devoted to optimizing the degree of reconstruction to achieve complete reconstruction, thereby achieving maximum catalytic activity. Transition metal-based phosphates are highly promising OER electrocatalysts due to their structural diversity, robust structural stability, ability to accept protons to promote the oxidation of metal species, and capacity to induce distorted local metal geometries that facilitate the adsorption and oxidation of water molecules [8, 9]. In addition, metaphosphates with higher phosphorus content have been reported to exhibit enhanced OER activity [10]. Previous studies have extensively observed the reconstruction process of the transition metal based (meta)phosphates [11-14]. The reconstruction process of phosphates typically accompanies the leaching of alkali metal and phosphorous, with the in-situ formed (oxy)hydroxide active species. Notably, most of the reported (meta)phosphates experienced limited and uncompleted reconstruction process, resulting in limited active species generated on the catalyst surface and thus the limited OER activity. Thus, it is of great significance to achieve fast and deep reconstruction of metaphosphates catalysts to produce maximally active sites with high intrinsic activity, thereby improving electrocatalytic activity.

In this work, a cobalt metaphosphate ($K_2Co(PO_3)_4$) was synthesized and employed in water/seawater electrolysis. The as-prepared electrocatalyst has undergo fast, deep self-

reconstruction process, resulting in the in-situ formation of CoOOH, which stands as the actual active sites for OER. This process is also accompanied by the leaching of potassium and metaphosphate ions into the electrolyte. The as-prepared catalyst suggests favorable activity, selectivity, and stability towards OER.

5.2 Results and Discussion

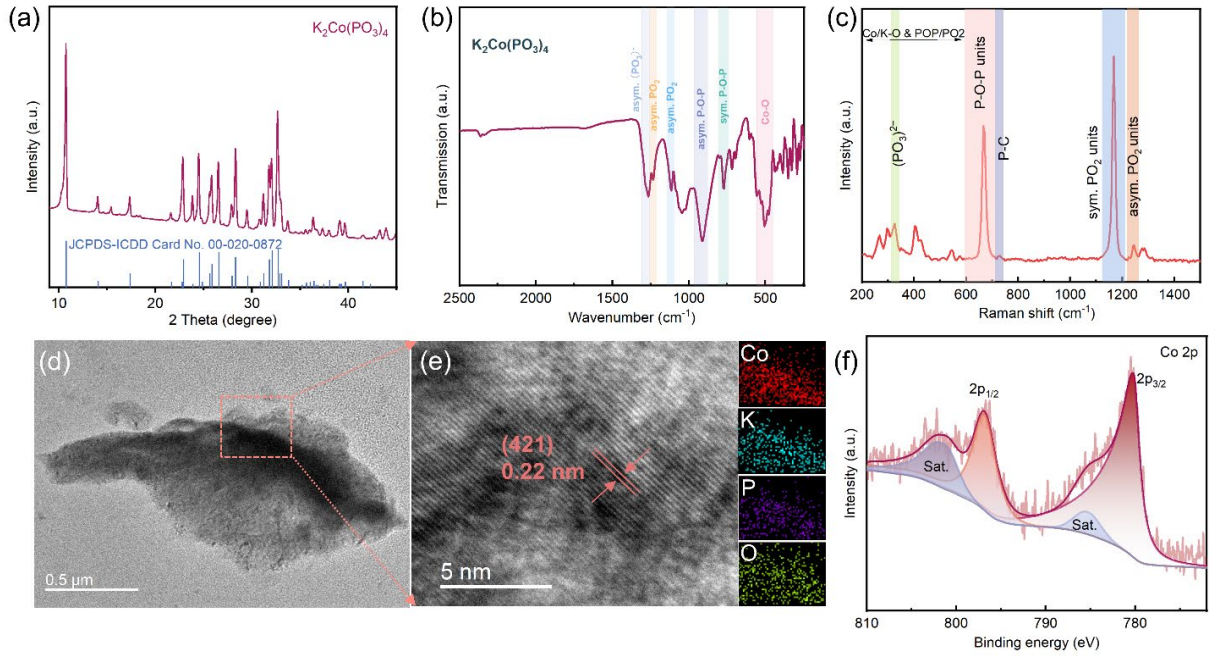

Figure 5.1 (a) XRD pattern, (b) FT-IR spectrum, (c) Raman spectrum, (d) TEM image, (e) HR-TEM image of $K_2Co(PO_3)_4$, and the XPS spectrum of (f) Co 2p for the as-prepared $K_2Co(PO_3)_4$ sample.

The catalyst was synthesized by a solution combustion method. The XRD pattern of the synthesized sample, as illustrated in **Figure 5.1a**, reveals distinct diffraction peaks that can be accurately indexed to the monoclinic $K_2Co(PO_3)_4$ (JCPDS-ICDD Card No. 00-020-0872). To elucidate the local structural environment, the FT-IR spectrum of the sample was recorded and is presented in **Figure 5.1b**. The peaks observed in the low-wavenumber region, below

600 cm^{-1}, can be attributed to the Co–O or K–O groups. The broad peaks centered at 1230 cm^{-1} and 1118 cm^{-1} correspond to the asymmetric and symmetric PO_2 units, respectively [15]. The characteristic bands for PO_3^-, which are the symmetric and asymmetric stretching vibrations of (P-O-P) units, are located at the 755-806 cm^{-1} and 910-950 cm^{-1}, respectively. The sharp peak at 1268 cm^{-1} is the asymmetric stretching vibration of $(PO_3)^-$ [16]. The Raman spectrum also reveals the terminal PO_2 and bridging P–O–P bands. As illustrated in **Figure 5.1c**, the sharp peak at approximately 671 cm^{-1} corresponds to the symmetric stretching vibration of the P–O–P bond [17]. The bands at 1167 cm^{-1} and 1246 cm^{-1} are attributed to the symmetric and asymmetric stretching modes of PO_2 unit [18], respectively. Additionally, the peak at 321 cm^{-1} corresponds to the stretching vibration of the $(PO_3)^{2-}$ group.

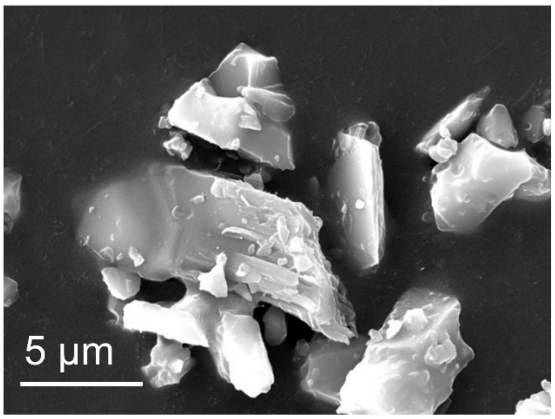

Figure 5.2 SEM image of the as-prepared $K_2Co(PO_3)_4$ sample.

The SEM image in **Figure 5.2** illustrates the blocky morphology of the synthesized sample, featuring varying sizes, which can be further confirmed by the TEM image (**Figure 5.1d**). The HR-TEM image in **Figure 5.1e**, magnified from the selected area of the TEM image, reveals a distinct lattice fringe with a spacing distance of 0.22 nm, corresponding to the (421) plane of monoclinic cobalt metaphosphate. Additionally, the EDX mapping images demonstrate the uniform distribution of K, Co, P, and O elements within the particles,

without any segregation. The XPS spectra were then obtained to probe the surface chemistry of the prepared sample. The Co 2p spectrum indicates a convoluted $2p_{1/2}$ and $2p_{3/2}$ spin-orbit doublet peak, along with the two distinctive satellite peaks, indicate an oxidized Co^{2+} species (**Figure 5.1f**). The Co $2p_{3/2}$ peak is observed at 781.5 eV, accompanied by a satellite splitting peak at 785.5 eV, while the Co $2p_{1/2}$ peak is located at 796.9 eV, with a satellite splitting peak at 801.8 eV. The P 2p spectrum in **Figure 5.3a** can be resolved into two sub-peaks situated at 133.2 and 132.6 eV, which correspond to the characteristic P $2p_{1/2}$ and $2p_{3/2}$ peaks for the PO_3^{2-} ion. The O 1s spectrum can be deconvoluted into three peaks at 531.2, 532.3, and 533.4 eV, attributed to $(H_2PO_4)^-$, $(PO_3)^-$, and P–OH, respectively (**Figure 5.3b**).

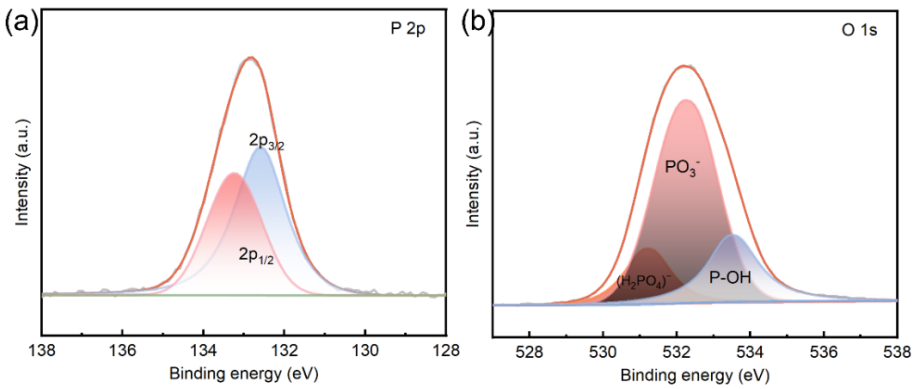

Figure 5.3 The XPS spectra of (a) P 2p and (b) O 1s for the as-prepared $K_2Co(PO_3)_4$ sample.

The OER performance was systematically evaluated using a conventional three-electrode-cell in 1 M KOH solution and simulated seawater. The glassy carbon electrode was employed as the working electrode, while a Hg/HgO (1 M KOH) electrode served as the reference electrode, and a platinum mesh was utilized as the counter electrode. It has been extensively reported that the transition metal-based electrocatalysts undergo a dynamic reconstruction process, transforming into real reactive species, typically in the form of (oxy)hydroxides. To investigate the structural evolution of the as-prepared sample, the corresponding CV curves and the chronopotentiometry curve have been presented. The CV curves depicted in **Figure**

5.4a indicate a significant increase in the intensity of the oxidation peaks after 2000 cycles of activation, thereby confirming the occurrence of the reconstruction process. The chronopotentiometry curve further confirms the reconstruction process, as evidenced by the increasing current density over time under constant voltage, as shown in **Figure 5.4b**, indicating the generation of additional electrochemically active sites.

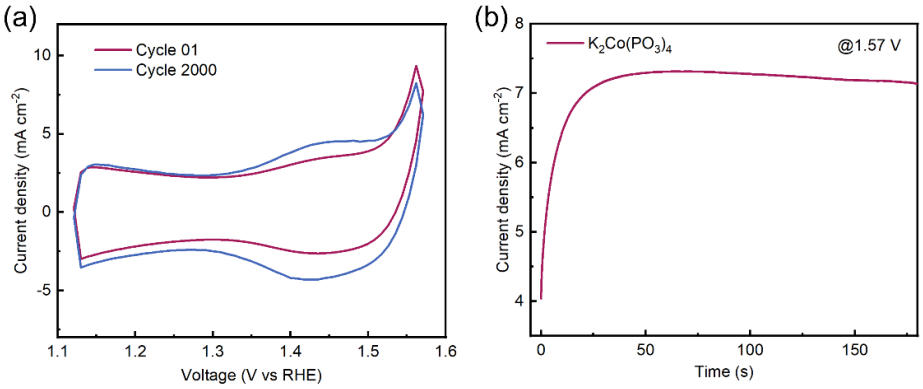

Figure 5.4 The electrochemical reconstruction process illustrated by (a) CV curves and (b) chronopotentiometry curve in 1 M KOH solution.

After the activation process, the polarization curves measured in alkaline electrolyte and simulated seawater (1 M KOH + 0.5 M NaCl) suggest comparable activity, necessitating an overpotential of 327 and 335 mV at the current density of 10 mA cm^{-2}, respectively, both lower than benchmark RuO_2, as shown in **Figure 5.5a**. The Tafel slopes extracted from the LSV curves also indicate that the catalyst demonstrates similar kinetics for both electrolytes (**Figure 5.5b**). The electrochemical active surface area (ECSA) has been demonstrated to exhibit a positive correlation with the double-layer capacitance (C_{dl}) values. The calculated C_{dl} values of $K_2Co(PO_3)_4$ and RuO_2, derived from the CV measurements at various scan rates (**Figure 5.6a** and **b**), are depicted in **Figure 5.5c**. The prepared catalyst demonstrate a much higher C_{dl} value (9.2 mF dec^{-1}) than RuO_2 (1.1 mF dec^{-1}), indicating the favorable ECSA of the $K_2Co(PO_3)_4$ material and further validating its efficiency. Additionally, the mass activity

(MA) and specific activity (SA, derived from Brunauer–Emmett–Teller (BET) specific surface area in **Figure 5.6c**) of the catalyst are determined to be 130.2 A g^{-1}_{oxide} and 1.3 mA cm^{-2}_{oxide}, respectively, both higher than that of RuO_2 (**Figure 5.5d**). The stability test of the catalyst in alkaline medium was conducted through CV testing for 1000 cycles, which suggests the robust nature of the cobalt metaphosphate due to the almost coincidence of the curves (**Figure 5.5e**). In simulated sweater, the synthesized catalyst also demonstrate significant stability. As depicted in **Figure 5.5f**, after the chronopotentiometry test at a constant current density of 10 mA cm^{-2} for over 50 h, the catalyst exhibits no discernible potential loss.

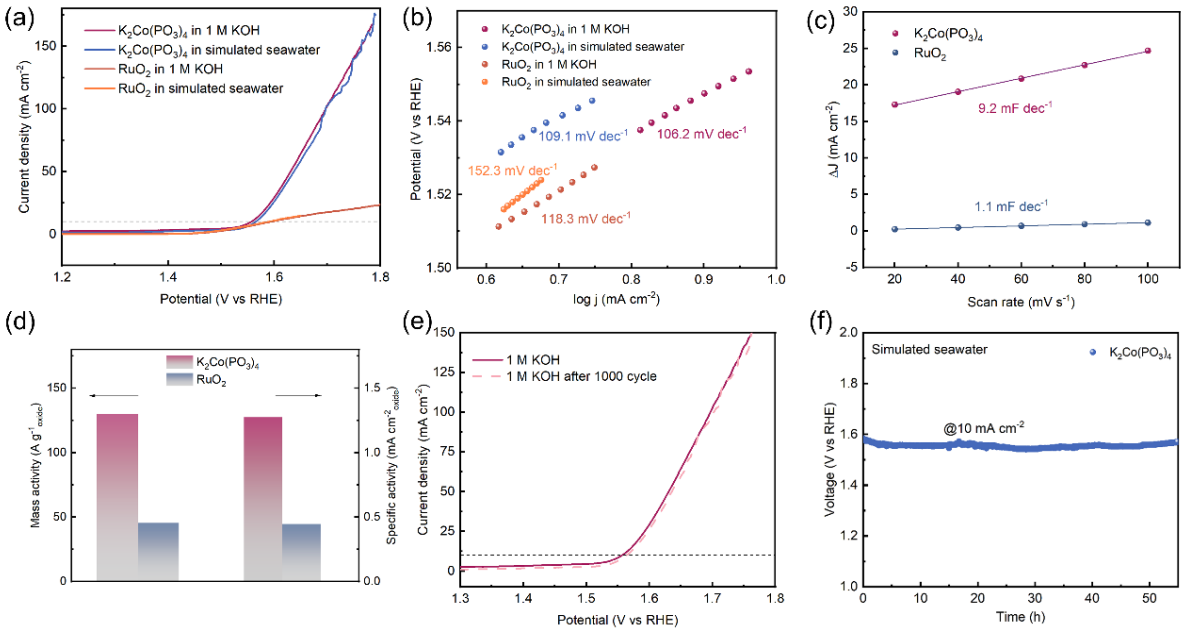

Figure 5.5 (a) Polarization curves and (b) Tafel plot of the prepared catalyst and benchmark RuO_2 in 1 M KOH and simulated seawater. (c) The double later capacitance and (d) MA and SA measurements of the catalyst and RuO_2 in 1 M KOH. Stability tests in (e) 1 M KOH by CV test and (f) simulated seawater by chronopotentiometry test.

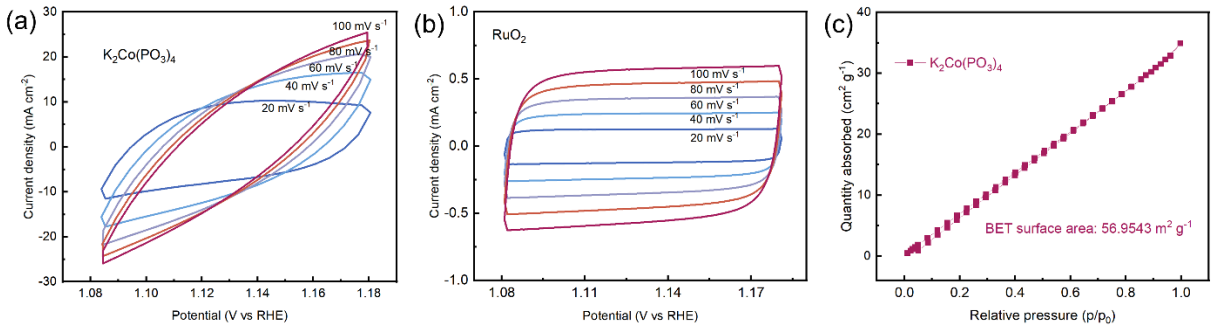

Figure 5.6 CV curves of (a) the prepared catalyst and (b) RuO_2 under different scan rates. (c) Nitrogen adsorption-desorption isotherm profiles of the prepared catalyst.

Chemically selective anode electrocatalysts are critical to the durability of seawater electrolysers by mitigating component corrosion and degradation associated with chlorine electrochemistry. To evaluate the OER selectivity of the $K_2Co(PO_3)_4$ electrocatalyst, rotating ring disk electrodes (RRDE) voltammograms were examined and analyzed. As shown in **Figure 5.7a**, OER predominantly evolved from the electrocatalyst in the simulated seawater, with no detectable signal of ClO^- reduction, indicating the high OER selectivity of the prepared electrocatalyst. After the stability test in alkaline and seawater electrolytes, both XPS spectra of Cl 2p of the catalyst exhibit negligible chlorine signals, further confirming the superior resistance to chlorine and the selective adsorption of OH^- (**Figure 5.7b**).

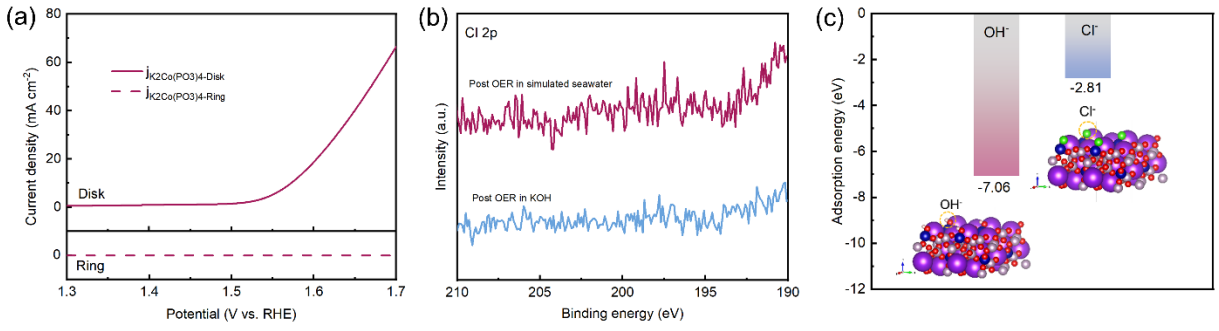

Figure 5.7 (a) RRDE voltammograms of the $K_2Co(PO_3)_4$ disk and Pt ring in simulated seawater. (b) XPS spectra of Cl 2p after OER stability test in simulated seawater. (c) Surface

adsorption energies of OH^- and Cl^- on selected facet.

To attain a more thorough understanding of the underlying mechanisms contributing to the high OER selectivity of the catalyst, DFT calculations were performed and analyzed. In this study, the (-221) facet of $K_2Co(PO_3)_4$ was chosen for DFT computations due to the high stability and efficient active atom exposure of this surface. **Figure 5.8** shows the 3D projection, side view, and top view of the $K_2Co(PO_3)_4$ structure. The adsorption energies of OH^- and Cl^- on the selected plane were calculated. The total adsorption energies were calculated based on the equation of $\Delta E = E_{OH^*} - E_* - OH^-/Cl^-$, with the obtained results shown in **Table 5.1**. **Figure 5.7c** compares the total adsorption energies of OH^- and Cl^-. It shows that hydroxyl group shows much more negative adsorption energy towards the surface than chloride does, suggesting that hydroxyl has a higher adsorption tendency towards the surface and could dominantly absorb on the surface. This can be conducive to reduce the adsorption of chloride and the occurrence of subsequent chloride-related side reactions, further confirming the chlorine resistance of the prepared catalyst.

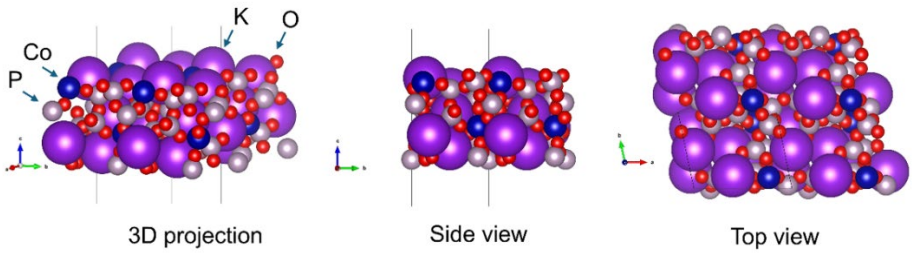

Figure 5.8 The optimized structure of (-221) facet of $K_2Co(PO_3)_4$.

Table 5.1 The Adsorption energy of OH^- and Cl^- from the DFT calculations.

Ions	Site	Total energy (eV)	Adsorption energy (eV)

		E_{OH*}	E_{*}	OH^-	Cl^-	ΔE
OH^-	10	-370.47	-361.51	-3.53	/	
	17	-372.077	-361.51	-3.53	/	
	18	-372.09	-361.51	-3.53	/	
	3	-372.10	-361.51	-3.53	/	-7.06
	7	-372.10	-361.51	-3.53	/	
Cl^-	15	-364.59	-361.51	/	-0.28	
	18	-364.55	-361.51	/	-0.28	
	19	-364.59	-361.51	/	-0.28	
	23	-364.59	-361.51	/	-0.28	-2.81
	3	-364.59	-361.51	/	-0.28	

Post-OER characterizations were conducted to investigate the chemical changes of the electrocatalyst after the electrochemical OER process. The post-OER SEM images depicted in **Figure 5.9a** and **b** reveal that the catalyst is securely affixed to the 3D hierarchical networks of Ni foam, exhibiting a reduced particle size that is different from the previously observed large blocky structure.

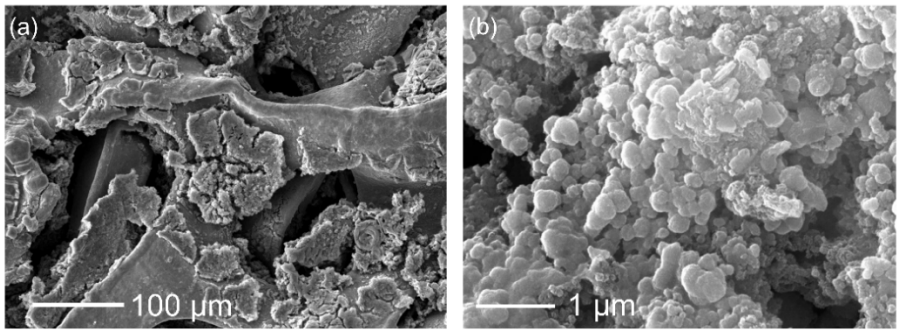

Figure 5.9 (a, b) SEM images of the catalyst after the OER test.

The XRD patterns of the catalyst after testing in alkaline solution and simulated seawater were recorded and suggested in **Figure 5.10a**. Obviously, the catalyst has undergone a complete structural transformation, and the transformed structure can be indexed as CoOOH phase. This is consistent with numerous previous studies indicating that the transition metal catalysts would experience a self-reconstruction process under OER conditions and form the corresponding transition metal oxyhydroxide.

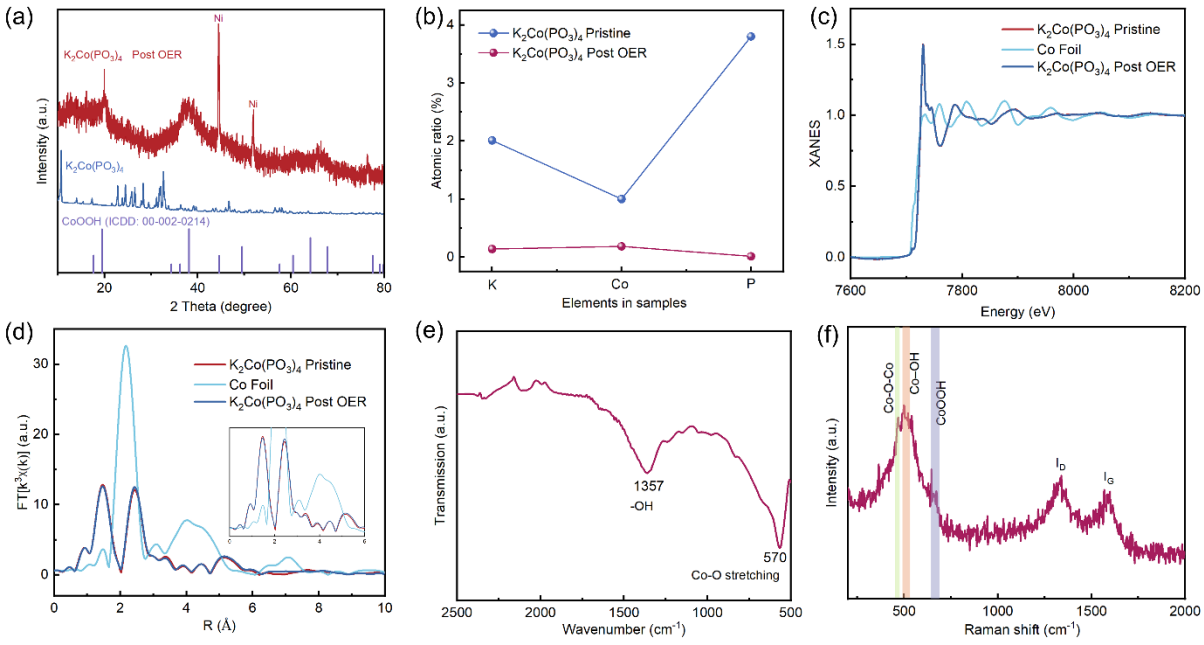

Figure 5.10 (a) XRD patterns, (b) ICP-OES results, normalized Co K-edge (c) XANES spectra and (d) FT-EXAFS spectra, (e) FT-IR spectrum, and (f) Raman spectrum of the

catalyst after overall water electrolysis test.

Figure 5.11a presents the TEM image of the electrocatalysts after stability test. The HR-TEM images selected from the TEM images presented in **Figure 5.11b** and **c** reveal distinct lattice fringes within the phase, which can be indexed to the (015) and (101) plane of the CoOOH phase, further confirming the structural change of the metaphosphate catalyst after OER. The EDX mapping images in **Figure 5.11d** exhibit notable differences compared to those of the pristine samples, revealing significantly weaker signals for the elements of K and P, while maintaining robust signals for the elements of Co and O, suggesting a potential loss of the K and P content.

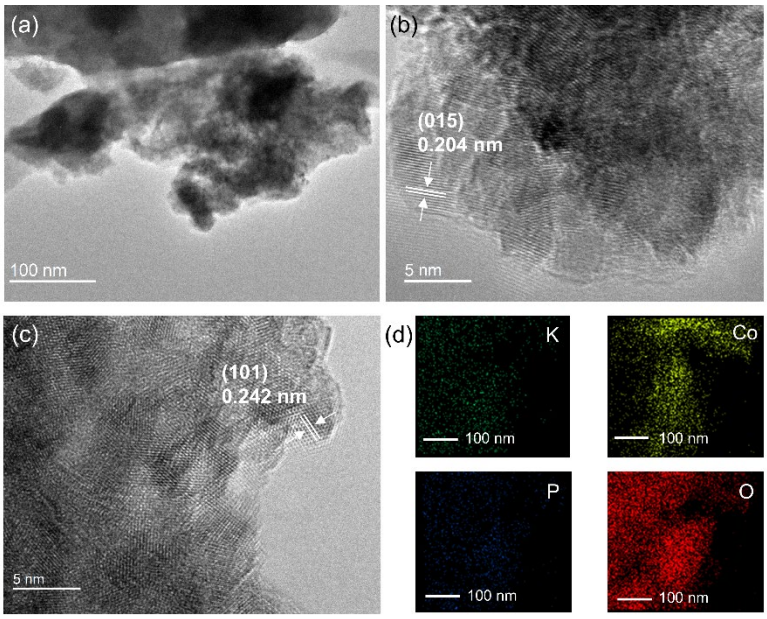

Figure 5.11 (a) TEM, (b, c) HR-TEM images, and (d) the corresponding EDX mapping images of the catalyst after the overall water electrolysis test.

The elemental analysis results detected by inductively coupled plasma mass spectrometry-optical emission spectrometry (ICP-OES) can provide more accurate elemental content information of catalyst, as suggested in **Figure 5.10b** and **Table 5.2**. The synthesized catalyst

demonstrates the targeted proportion, with the molar ratio of K/Co/P is about 2/1/3.84. However, after the OER stability test, it was found that the molar ratio of the elements was significantly different from that of the pristine catalyst. The P element with a large content in the pristine catalyst was significantly reduced, and the content of K was also greatly reduced, but not as much as P, while Co became the element with the highest content. The reservation of K may originate from those intercalated into layers of CoOOH and the residual of KOH in electrolyte. Previous results has proved that the large potassium cations could increase the interlayer spacing of CoOOH, expanding the Co−O bonds and optimizing the adsorption strength of oxygen intermediates, thereby improving the OER activity [19, 20].

Table 5.2 The ICP-OES data of the catalyst before and after the long-term stability test.

Sample	Element	Content (mg kg^{-1})	Atomic ratio
Pristine $K_2Co(PO_3)_4$	K	156765.53	2
	Co	117544.17	1
	P	237488.35	3.84
Post OER $K_2Co(PO_3)_4$	K	10826.48	0.14
	Co	21832.83	0.186
	P	782.13	0.013

The electronic structure analysis and local atomic geometry of the catalysts before and after the OER tests, were further analyzed using X-ray absorption near-edge structure (XANES) and extended X-ray absorption fine structure (EXAFS), elucidating the local configurations around cobalt. **Figure 5.10c** and **Figure 5.10d** show the Co K-edge XANES and EXAFS curves of the $K_2Co(PO_3)_4$ catalysts before and after the stability test. The near-edge absorption energy position of the Co K-edge for both samples are much higher than those of Co foil, suggesting a positive charge within the catalyst. Additionally, the Co K-edge XANES curve of the post-OER sample shifts to lower energy in comparison to the pristine sample. The k^2-weighted Fourier transform EXAFS (FT-EXAFS) curves for both samples in **Figure 5.10d** suggest characteristic peaks at 1.47 and 2.45 Å, corresponding to the Co−O and Co_{Oh}−Co_{Oh} (Oh means octahedral) bond, with no observable metallic Co−Co bond peak at 2.17 Å, as seen in Co foil.

The FT-IR spectrum of the catalyst after stability test also exhibits notable differences compared to the pristine spectrum, providing additional evidence of the structural changes. As illustrated in **Figure 5.10e**, the FT-IR signals are reduced to two main peaks, which can be attributed to the O-H vibration (~1357 cm^{-1}) and the Co-O stretching vibration (~570 cm^{-1}) for CoOOH, respectively. Furthermore, the Raman spectrum of the catalyst after the stability test mainly displays peaks corresponding to cobalt oxyhydroxide, including the Co-O-Co vibration at 468 cm^{-1}, Co-OH at 501 cm^{-1}, and CoOOH at 664 cm^{-1}, further validating the structural reconstruction to CoOOH (**Figure 5.10f**). The Raman characteristic peaks at 1330 cm^{-1} and 1582 cm^{-1} correspond to the D band and G band of carbon, respectively, which was added as conductive carbon additive when preparing catalyst ink.

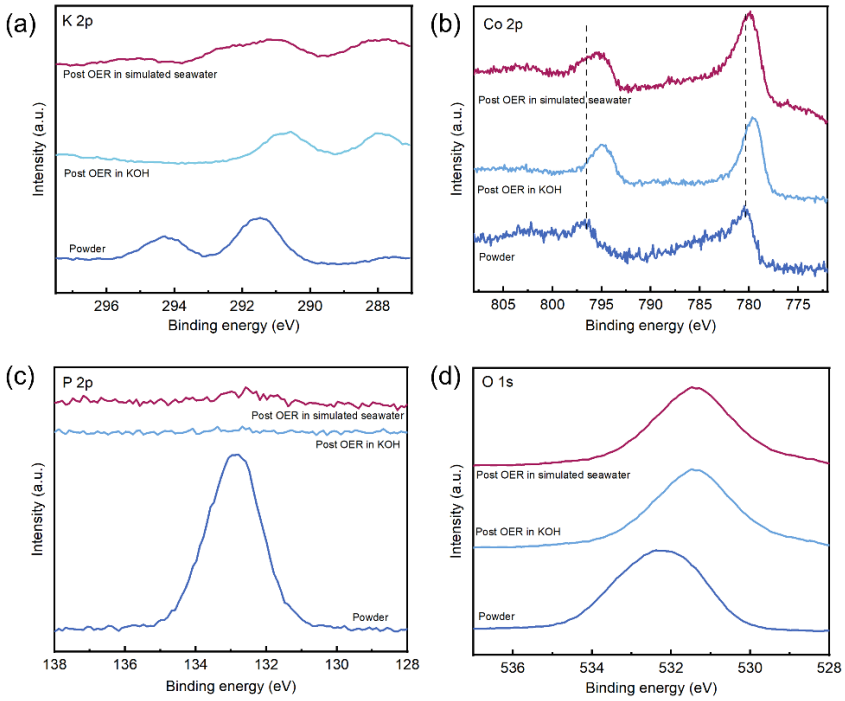

Figure 5.12 XPS spectra of (a) K 2p, (b) Co 2p, (c) P 2p, and (d) O 1s of the catalyst after overall water electrolysis test in 1 M KOH and simulated seawater.

To probe the surface chemistry of the catalyst after OER, XPS spectra were obtained and analyzed. The peaks were attributed to K 2p (**Figure 5.12a**) and P 2p (**Figure 5.12c**) after the long-term stability test exhibit diminished signals in comparison to the original sample, indicating structural reconstruction with the dissolution of P and K, in accordance with the above results. The Co 2p spectra in **Figure 5.12b** suggests that both Co $2p_{1/2}$ and Co $2p_{3/2}$ shifted to a lower binding energy after OER test in alkaline condition and simulated seawater, indicating that the valence states of Co has been increased from Co^{2+} (in metaphosphate) to Co^{3+} (in CoOOH), consistent with above results and prior reports [21, 22]. The O 1s signals after stability test shifted to lower binding energies (**Figure 5.12d**), which can be attributed to the extensive charge transfer to lattice metal–O [23]. Considering the above results, it can be concluded that the metaphosphate phase has been changed to the CoOOH species after OER process, as illustrated in **Figure 5.13**.

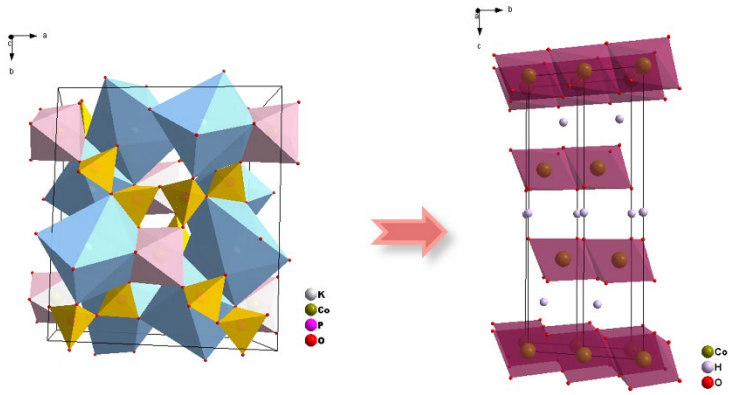

Figure 5.13 Structural transformation of the catalyst after long-term stability.

To gain insight into the structural evolution during OER process, in-situ Raman spectra were obtained under different electrolytes. For in situ Raman spectra immersing in both electrolytes, the three characteristic peaks at 321, 671, and 1167 cm^{-1} corresponding to $(PO_3)^{2-}$ stretching vibration, stretching vibration of P-O-P, and symmetric stretching mode of PO_2 unit, respectively, are well maintained and show no obvious changes (**Figure 5.14a** and **b**), indicating that the change of the catalyst phase during OER requires certain conditions, such as the prolonged time or high voltage/current.

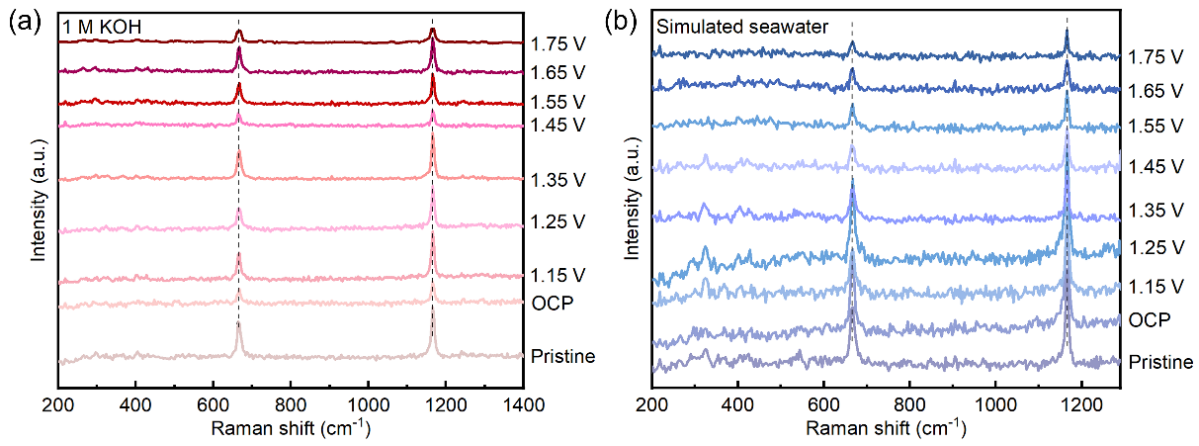

Figure 5.14 In-situ Raman spectra of the catalyst under (a) 1 M KOH and (b) simulated seawater with varying applied voltages.

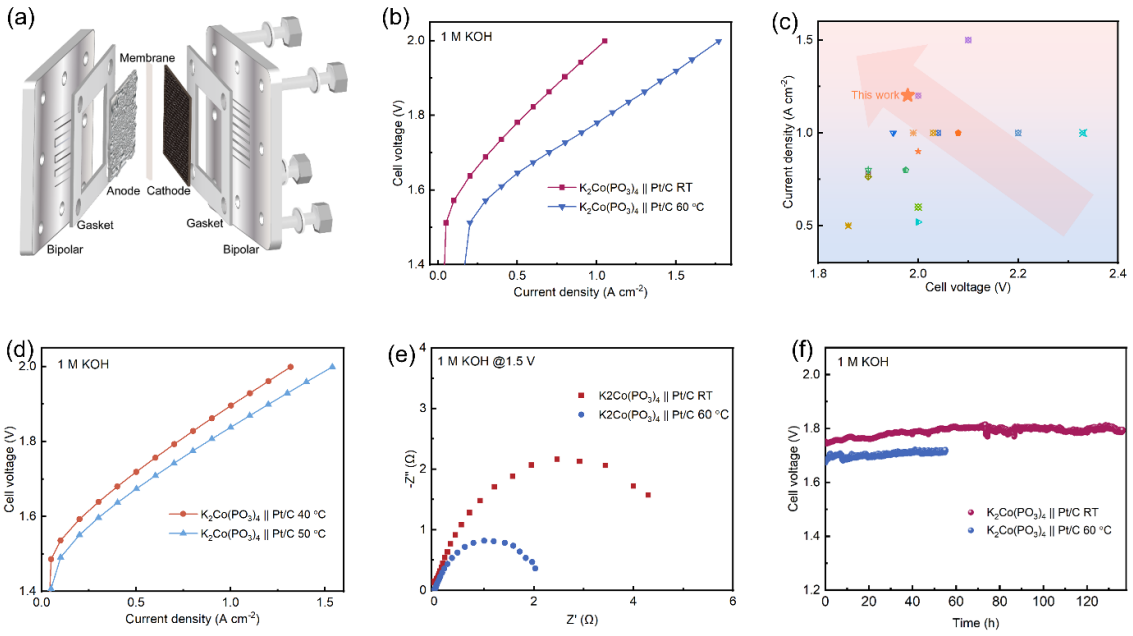

Figure 5.15 (a) AEMWE electrolyser configuration. (b) Polarization curves of $K_2Co(PO_3)_4$-based cell in 1 M KOH. (c) Performance comparison between $K_2Co(PO_3)_4$-based cell and other cells [24-40]. (d) Electrolyser polarization curves at 40 and 50 °C. (e) EIS Nyquist plots of the electrolyser at 1.5 V. (f) Stability tests of the electrolyser in 1 M KOH.

Inspired by the desirable OER performance, an anion-exchange-membrane water electrolyser (AEMWE) with the synthesized material as anodic catalyst and the commercial Pt/C as the cathode catalyst (denoted as $K_2Co(PO_3)_4$ || Pt/C cell) was further assembled to evaluate the practical application potential for water and seawater electrolysis. The schematic diagram of the assembled AEMWE was shown in **Figure 5.15a**. The electrolyser primarily consists of a bipolar plate, carbon paper (serving as the catalyst carrier and gas diffusion layer of the anode), Ni foam (serving as the catalyst carrier and gas diffusion layer of the cathode), and an anion exchange membrane. The polarization curves of the assembled $K_2Co(PO_3)_4$ || Pt/C electrolyser in a 1 M KOH electrolyte, measured at temperatures ranging from room temperature to 60 °C, are illustrated in **Figure 5.15b** and **Figure 5.15d**. To achieve a current density of 0.5 A cm^{-2}, the $K_2Co(PO_3)_4$ || Pt/C electrolyser requires cell voltages of 1.75 and

1.68 V at room temperature and 60 ℃, respectively. Additionally, cell voltages of 1.92 V and 1.84 V are necessary at room temperature and 60 ℃ to achieve a current density of 1.0 A cm^{-2}. In comparison to other advanced AEMWE systems, the assembled $K_2Co(PO_3)_4$ || Pt/C electrolyser still demonstrates considerable superiority in activity, as illustrated in **Figure 5.15c**.

To understand the reason behind the outstanding performance of the assembled AEMWE electrolyser, the Nyquist plot of the electrolyser obtained through EIS was analyzed. It is evident that increasing the temperature significantly reduces the polarization resistance of the electrolyser, as demonstrated by the considerably smaller semicircle observed at elevated temperature (**Figure 5.15e**). In addition to its notable water splitting activity, the AEMWE with a $K_2Co(PO_3)_4$ anode also exhibits favorable durability, at an industrial-required current density (0.5 A cm^{-2}), as evidenced by the nearly constant potential for over 120 h at room temperature and over 60 h at 60 ℃ (**Figure 5.15f**). The evaluation of the AEMWE underscores the potential of $K_2Co(PO_3)_4$ as a promising electrocatalyst for the practical application of the overall water splitting process.

Simulated seawater was subsequently fed to the assembled $K_2Co(PO_3)_4$ || Pt/C electrolyser. It is suggested that cell voltages of 1.781 and 1.715 V are needed for delivering a current density of 0.5 A cm^{-2} for room temperature and 60 ℃, respectively (**Figure 5.16e**), which are slightly larger than the cell feeding pure alkaline electrolyte. Additionally, the electrolyser requires 1.998 and 1.936 V at 1.0 A cm^{-2} for room temperature and 60 ℃, respectively. Similar to the electrolyser in an alkaline electrolyte, the Nyquist plot obtained through EIS demonstrates that the polarization resistance of the electrolyser at elevated temperatures is significantly lower than that at room temperature (**Figure 5.16b**), indicating the source of enhanced activity with increasing temperature. The current-voltage curves at 40 and 50 ℃ in

Figure 5.17c further demonstrate that a gradual increase in temperature can enhance the performance of the electrolyser. The gases generated by the cathode and anode of the electrolyser in simulated seawater as a function of time reveal that only hydrogen and oxygen, with a molar ratio of 2:1, are detected (**Figure 5.16d**). Furthermore, the experimentally measured gas quantities align with theoretically calculated results, demonstrating nearly 100% Faradaic efficiency and high selectivity of the electrolyser for green hydrogen production. Except for the high activity and selectivity, the $K_2Co(PO_3)_4$ based electrolyser exhibits prominent durability, sustaining operation for 300 h at room temperature and 100 h at 60 °C, as illustrated in **Figure 5.16e**.

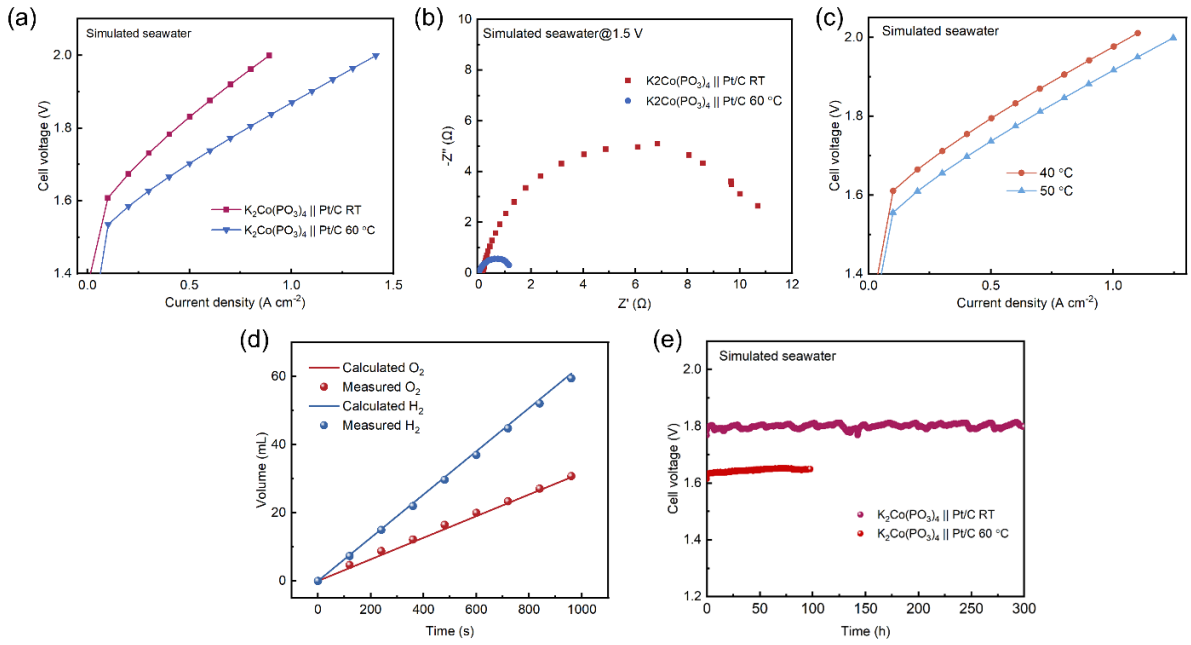

Figure 5.16 (a) Polarization curves and (b) EIS Nyquist plots of the $K_2Co(PO_3)_4$-based electrolyser in simulated seawater. (c) Polarization curves at 40 and 50 °C. (d) Theoretical calculation and experimental measurement of the amount of O_2 and H_2 in simulated seawater. (e) Stability performance at 0.5 A cm^{-2} in simulated seawater.

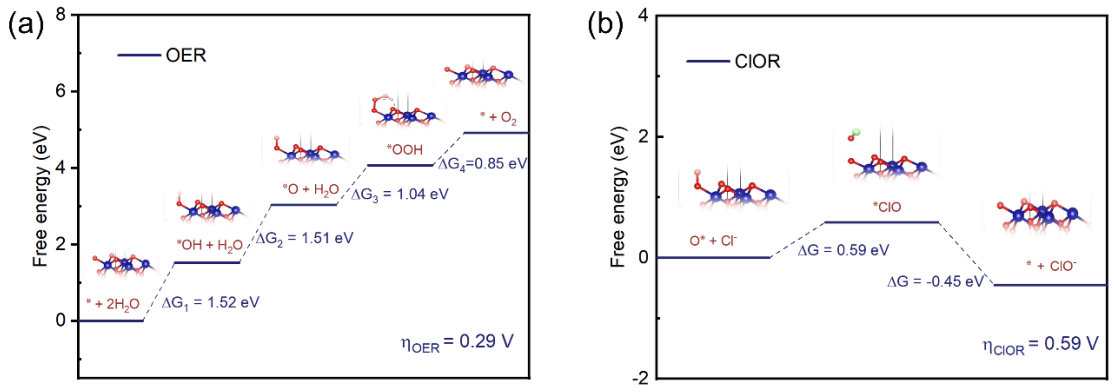

Figure 5.17 Gibbs free energy diagrams for (a) OER and (b) ClOR over CoOOH. Blue, red, white, and green spheres represent Co, O, H, and Cl atoms, respectively.

DFT theoretical calculations were conducted to gain mechanistic insights into the OER activity and selectivity on reconstructed CoOOH (001) surface. Typically, the CoOOH surface is assumed to follow the Adsorbate Evolution Mechanism (AEM) pathway during OER. According to the DFT calculations, the adsorption of hydroxyl on the (001) surface of CoOOH requires the largest free energy barrier, standing as the potential determining step (PDS) for OER pathway (**Figure 5.17a**). A low theoretical overpotential of 0.29 V for OER can be obtained on the CoOOH surface. In comparison, the formation of oxychloride intermediate via the adsorption of chloride anion on the CoOOH surface is the PDS step for ClOR, requiring a potential barrier of 0.59 eV, which implies that the surface adsorption of chloride anion is unfavorable (**Figure 5.17b**). Correspondingly, the calculated overpotential for ClOR is 0.59 V, which is much larger than that for OER, suggesting the high selectivity of OER on the fully reconstructed cobalt oxyhydroxide surface.

5.3 Conclusion

Cobalt metaphosphate has been successfully synthesized and employed as an anodic OER catalyst for seawater electrolysis. It has been found that during the OER process, the

synthesized catalyst undergoes a distinct structural reconstruction, leading to a phase transition from cobalt metaphosphate to the corresponding oxyhydroxide CoOOH, which serves as the actual active site for anodic OER. In addition, both experimentation and DFT calculation indicate the advantageous adsorption of OH^- over Cl^- on the catalyst surface, thereby achieving highly selective and stable seawater electrolysis. Moreover, the prepared electrode suggests robust durability in both alkaline electrolyte and simulated seawater. This work highlights the high potential of transition metal metaphosphate as the self-sacrificing pre-catalyst for the generation of truly active oxyhydroxide, thus achieving highly active, selective, and durable anodic OER for water and seawater electrolysis.

5.4 References

1. M. J. Burke and J. C. Stephens, *Energy Research & Social Science*, 2018, **35**, 78-93.
2. S. E. Hosseini and M. A. Wahid, *Renewable and Sustainable Energy Reviews*, 2016, **57**, 850-866.
3. N.-T. Suen, S.-F. Hung, Q. Quan, N. Zhang, Y.-J. Xu and H. M. Chen, *Chemical Society Reviews*, 2017, **46**, 337-365.
4. M. A. Khan, T. Al-Attas, S. Roy, M. M. Rahman, N. Ghaffour, V. Thangadurai, S. Larter, J. Hu, P. M. Ajayan and M. G. Kibria, *Energy & Environmental Science*, 2021, **14**, 4831-4839.
5. R. K. B. Karlsson and A. Cornell, *Chemical Reviews*, 2016, **116**, 2982-3028.
6. F. Dionigi, T. Reier, Z. Pawolek, M. Gliech and P. Strasser, *ChemSusChem*, 2016, **9**, 962-972.
7. H. Zhong, Q. Zhang, J. Yu, X. Zhang, C. Wu, Y. Ma, H. An, H. Wang, J. Zhang, X. Wang and J. Xue, *Advanced Energy Materials*, 2023, **13**, 2301391.

8. X.-W. Chang, S. Li, L. Wang, L. Dai, Y.-P. Wu, X.-Q. Wu, Y. Tian, S. Zhang and D.-S. Li, *Advanced Functional Materials*, 2024, **34**, 2313974.

9. Y. Li, Z. Wang, J. Hu, S. Li, Y. Du, X. Han and P. Xu, *Advanced Functional Materials*, 2020, **30**, 1910498.

10. R. Gond, D. K. Singh, M. Eswaramoorthy and P. Barpanda, *Angewandte Chemie*, 2019, **131**, 8418-8423.

11. H. Cao, P. Qiao, Q. Zhong, R. Qi, Y. Dang, L. Wang, Z. Xu and W. Zhang, *Small*, 2023, **19**, 2204864.

12. H. Zhao and Z.-Y. Yuan, *ChemCatChem*, 2020, **12**, 3797-3810.

13. I. V. Odynets, N. Y. Strutynska, J. Li, W. Han, I. V. Zatovsky and N. I. Klyui, *Dalton Transactions*, 2018, **47**, 15703-15713.

14. X. Zhang, Q. Hou, S. Cao, X. Lin, X. Chen, Z. Wang, S. Wei, S. Liu, F. Dai and X. Lu, *Green Chemistry*, 2023, **25**, 7883-7903.

15. S. Chaudhary and R. Murugavel, *Chemistry of Materials*, 2024, **36**, 6475-6488.

16. N. Yao, Y. Zhang, D. Kong, J. Zhu, Y. Tao and T. Qiu, *IOP Conference Series: Materials Science and Engineering*, 2011, **18**, 062022.

17. C. Murugesan, S. P. Panjalingam, S. Lochab, R. K. Rai, X. Zhao, D. Singh, R. Ahuja and P. Barpanda, *Nano Energy*, 2021, **89**, 106485.

18. Z. Černošek, J. Holubová and P. Hejda, *Journal of Non-Crystalline Solids*, 2019, **522**, 119556.

19. H. Jia, N. Yao, C. Yu, H. Cong and W. Luo, *Angew Chem Int Ed Engl*, 2023, **62**, e202313886.

20. F. Dionigi, Z. Zeng, I. Sinev, T. Merzdorf, S. Deshpande, M. B. Lopez, S. Kunze, I. Zegkinoglou, H. Sarodnik, D. Fan, A. Bergmann, J. Drnec, J. F. d. Araujo, M. Gliech,

D. Teschner, J. Zhu, W.-X. Li, J. Greeley, B. R. Cuenya and P. Strasser, *Nature Communications*, 2020, **11**, 2522.

21. X. Li, L. Xiao, L. Zhou, Q. Xu, J. Weng, J. Xu and B. Liu, *Angewandte Chemie*, 2020, **132**, 21292-21299.
22. L. He, N. Wang, B. Sun, L. Zhong, Y. Wang, S. Komarneni and W. Hu, *Journal of Colloid and Interface Science*, 2023, **650**, 1274-1284.
23. D. Liu, H. Ai, J. Li, M. Fang, M. Chen, D. Liu, X. Du, P. Zhou, F. Li, K. H. Lo, Y. Tang, S. Chen, L. Wang, G. Xing and H. Pan, *Advanced Energy Materials*, 2020, **10**, 2002464.
24. Y. Bao, X. Liang, H. Zhang, X. Bu, Z. Cai, Y. Yang, D. Yin, Y. Zhang, L. Chen, C. Yang, X. Hu, X. C. Zeng, J. C. Ho and X. Wang, *Advanced Energy Materials*, 2024, DOI: 10.1002/aenm.202401909.
25. H. Chai, X. Ma, Y. Dang, Y. Zhang, F. Yue, X. Pang, G. Wang and C. Yang, *J Colloid Interface Sci*, 2024, **654**, 66-75.
26. K. Ham, S. Hong, S. Kang, K. Cho and J. Lee, *ACS Energy Letters*, 2021, **6**, 364-370.
27. J.-Y. Jeong, Y. S. Park, J. Jeong, K.-B. Lee, D. Kim, K.-Y. Yoon, H.-S. Park and J. Yang, *Journal of Materials Chemistry A*, 2022, **10**, 25070-25077.
28. X. Jiang, V. Kyriakou, B. Wang, S. Deng, S. Costil, C. Chen, T. Liu, C. Deng, H. Liao and T. Jiang, *Chemical Engineering Journal*, 2024, **486**.
29. D. Kong, C. Meng, Y. Wang, X. Chen, J. Zhang, L. Zhao, J. Ji, L. Zhang and Y. Zhou, *Applied Catalysis B: Environmental*, 2024, **343**.
30. L. Li, Z. Zheng, J. Li, Y. Mu, Y. Wang, Z. Huang, Y. Xiao, H. Huang, S. Wang, G. Chen and L. Zeng, *Small*, 2023, **19**, e2301261.
31. S. Li, T. Liu, W. Zhang, M. Wang, H. Zhang, C. Qin, L. Zhang, Y. Chen, S. Jiang, D. Liu, X. Liu, H. Wang, Q. Luo, T. Ding and T. Yao, *Nat Commun*, 2024, **15**, 3416.

32. W.-G. Lim, H. N. Truong, J.-Y. Jeong, D. Kim, L. S. Oh, C. Jo, C. Kim, H. J. Kim, S. M. Choi, H. Shin, S. Lee and E. Lim, *Applied Catalysis B: Environmental*, 2024, **343**.

33. X. Lin, X. Li, L. Shi, F. Ye, F. Liu and D. Liu, *Small*, 2024, **20**, e2308517.

34. Y. Ma, J.-J. Wang, X.-H. Liu, N. Xu, X. Li, Y.-H. Wang, L.-M. Zhao, Y.-M. Chai and B. Dong, *Chemical Engineering Journal*, 2024, **490**.

35. W. Ning, R. Wang, X. Li, M. H. Wang, H. G. Xu, H. Y. Lin, X. P. Fu, M. Wang, P. F. Liu and H. G. Yang, *Chem Commun (Camb)*, 2023, **59**, 11803-11806.

36. S. Park, J. H. Jun, M. Park, J. Jeong, J.-H. Jo, S. Jeon, J. Yang, S. M. Choi, W. Jo and J.-H. Lee, *Energy & Fuels*, 2024, **38**, 4451-4463.

37. Y. S. Park, J. H. Lee, M. J. Jang, J. Jeong, S. M. Park, W.-S. Choi, Y. Kim, J. Yang and S. M. Choi, *International Journal of Hydrogen Energy*, 2020, **45**, 36-45.

38. F. Razmjooei, T. Morawietz, E. Taghizadeh, E. Hadjixenophontos, L. Mues, M. Gerle, B. D. Wood, C. Harms, A. S. Gago, S. A. Ansar and K. A. Friedrich, *Joule*, 2021, **5**, 1776-1799.

39. X. She, C. Feng, D. Liu, Z. Fan, M. Yang and Y. Li, *International Journal of Hydrogen Energy*, 2024, **59**, 1297-1304.

40. F.-L. Wang, Y.-W. Dong, C.-J. Yu, B. Dong, X.-Y. Zhang, R.-Y. Fan, J.-Y. Xie, Y.-N. Zhou and Y.-M. Chai, *Applied Catalysis B: Environmental*, 2023, **331**.

Chapter 6 Conclusions and Outlook

6.1 Conclusions

This dissertation presents significant advancements in the development and optimization of transition-metal-based electrocatalysts for efficient and stable alkaline and seawater electrolysis, specifically addressing the challenges associated with the OER in the presence of chloride ions. Through extensive characterization techniques and theoretical calculations, this work systematically investigated the critical factors influencing catalytic activities of the electrocatalysts and elucidates the underlying mechanisms of the reaction. The primary conclusions drawn from this thesis are as follows.

Chapter 3 focuses on CeO_2/NiFe-based LDH, which exhibits high oxygen ion diffusion rates and a substantial concentration of oxygen vacancies, especially under elevated temperature, thereby optimizing its OER activity. The partial coverage of CeO_2 on LDH surfaces inhibits direct Cl^- adsorption, while the high proton conductivity mitigates proton accumulation within LDH interlayers, thus preventing structural collapse and enhancing stability. The study underscores the importance of characterizing electrocatalyst at elevated temperatures, as the enhanced mixed ionic conductivities at these conditions significantly improve OER performance.

Chapter 4 introduces a nickel-doped double perovskite, $NdBa_{0.75}Ca_{0.25}Co_{1.5}Fe_{0.4}Ni_{0.1}O_{5+\delta}$ (NBCCFN), synthesized via the electrospinning method. The substitution of Ni in double perovskite increases the concentration of oxygen vacancies, facilitates the formation of reaction intermediates, and decreases reaction energy barrier. It has been found that the in situ formed transition metal-based oxyhydroxide through surface reconstruction serves as the

actual active sites for OER. Consequently, the nanofibrous NBCCFN demonstrates remarkable activity, selectivity, and durability towards water and seawater electrolysis. The ability of the NBCCFN-based electrolyser to maintain stable operation even with natural seawater highlights its significant potential for practical applications in electrolysis technologies.

Chapter 5 investigates cobalt metaphosphate ($K_2Co(PO_3)_4$), a relatively underexplored material in the field of electrocatalysis. Experimental results indicate that the cobalt metaphosphate would experience a complete and irreversible self-reconstruction process during OER. This reconstruction leads to a transformation of the phase structure from metaphosphate to the corresponding oxyhydroxide, i.e., CoOOH, which has been identified as the real active site for OER, achieving maximum utilization of active sites. Furthermore, the integration of experimental findings with theoretical calculations provides compelling evidence for the preferential adsorption of OH^- over Cl^- on the prepared catalyst surface, thereby inhibiting the occurrence of ClOR. As a result, high activity, selectivity, and stability have been achieved, even under practical seawater electrolysis conditions.

6.2 Outlook

In this thesis, the developed and optimized transition metal based electrocatalysts demonstrate significant potential as highly active, selective, and durable anodic OER electrocatalysts for both freshwater and seawater electrolysis under practical operating conditions. Here are some perspectives on future directions:

(1) The studies highlight the importance of understanding the mechanisms of OER. The role of oxygen vacancies, proton conductivity, and structural reconstruction in enhancing OER performance is crucial. Future research should focus on elucidating these mechanisms in

greater detail, possibly through advanced characterization techniques (such as FT-IR, XAS) and computational modeling.

(2) The research also underscores the importance of characterizing electrocatalysts and cells under realistic conditions, such as elevated temperatures, natural seawater, and larger current densities. Future studies should focus on long-term stability tests and real-world applications to validate the effectiveness of these materials.

(3) The insights gained from the mechanistic understanding presented in this thesis can significantly guide the design and optimization of electrocatalysts with enhanced activity, selectivity, and stability for both freshwater and seawater electrolysis.

(4) The ability of the NBCCFN-based electrolyser to operate stably with natural seawater is a significant step towards practical applications. Further optimization of this material to enhance its catalytic activity could position it as a viable alternative to precious metal-based benchmarks.